UNIVERSIDADE DE SÃO PAULO
INSTITUTO DE FÍSICA DE SÃO CARLOS

Luciana Andrade Dourado

Signatures of ultra-high energy cosmic ray sources in large-scale anisotropy measurements

São Carlos

2023

Luciana Andrade Dourado

Signatures of ultra-high energy cosmic ray sources in large-scale anisotropy measurements

Dissertation presented to the Graduate Program in Physics at the Instituto de Física de São Carlos da Universidade de São Paulo, to obtain the degree of Master in Science.

Concentration area: Theoretical and Experimental Physics

Advisor: Prof. Dr. Luiz Vitor de Souza Filho

Corrected version

(Original version available on the Program Unit)

São Carlos

2023

Dourado, Luciana Andrade
Signatures of ultra-high energy cosmic ray sources in large-scale anisotropy measurements / Luciana Andrade Dourado; advisor Luiz Vitor de Souza Filho - corrected version -- São Carlos 2023.
93 p.

Dissertation (Master's degree - Graduate Program in Theoretical and Experimental Physics) -- Instituto de Física de São Carlos, Universidade de São Paulo - Brasil , 2023.

1. Ultra-high energy cosmic rays. 2. Local sources. 3. Pierre Auger Observatory. I. Souza Filho, Luiz Vitor de, advisor. II. Title.

To my parents.

ACKNOWLEDGEMENTS

To my advisor, Prof. Vitor de Souza, for accepting me as a student and providing guidance over the last two years. Your help during some critical moments was fundamental to the development and conclusion of this work.

To Rodrigo Guedes Lang, for your guidance and patience in discussing my numerous doubts. This work would definitely not exist without your assistance.

To Cainã de Oliveira, who kindly made his scripts from local sources available for my studies and also promptly answered my questions.

To Luan Bonneau Arbeletche for assisting me in using the supercomputer Santos Dumont.

To Prof. Carola Dobrigkeit and Prof. Vitor de Souza for the opportunity to work at the Pierre Auger Observatory.

To my colleagues and friends that I have made in São Carlos for all our academic and non-academic conversations, even though I sometimes believe that I only know how to talk about academic matters.

To my friends from the Institute of Astronomy, Geophysics, and Atmospheric Sciences and the Institute of Physics of the University of São Paulo for their support, even from a distance.

To my family for their support and affection at all times, especially to my mother, father, sister, and godmother.

To all my professors who were part of my academic formation.

To all the employees of the São Carlos Institute of Physics for their maintenance and care of the institute. To Ricardo from the postgraduate program for assisting me with administrative issues. To Natalina and Neusa from the library for promptly correcting the formatting issues in my dissertation.

To the National Laboratory for Scientific Computing (LNCC) for providing HPC resources on the SDumont supercomputer. To LNCC support for their quick and effective resolution of issues faced by Santos Dumont users.

To CAPES and São Paulo Research Foundation (FAPESP) (grants 2021/10383-0 and 2021/01089-1) for their financial support.

"Que ninguém se engane, só se consegue a simplicidade através de muito trabalho."
Clarice Lispector

ABSTRACT

DOURADO, L. A. **Signatures of ultra-high energy cosmic ray sources in large-scale anisotropy measurements**. 2023. 93p. Dissertation (Master in Science) - Instituto de Física de São Carlos, Universidade de São Paulo, São Carlos, 2023.

The most energetic particles that have ever been detected in the Universe are the ultra-high energy cosmic rays. These fascinating particles originating from outer space are composed of protons and heavier nuclei with energies exceeding 1 EeV (10^{18} eV). The identification of astrophysical sources that accelerate these nuclei up to the highest energies is hindered by cosmic magnetic fields responsible for the deflection of charged particles. Although the trajectories of ultra-high energy cosmic rays do not point straight towards the acceleration sites, their distribution of arrival directions can provide essential information to understand their origin. In particular, the Pierre Auger Observatory has recently measured a dipolar modulation in the large-scale anisotropies pointing almost to the opposite direction of the Galactic Center, which is an important piece of evidence of an extragalactic origin. In this work, we further develop the understanding about the impact of astrophysical hypotheses in modeling the amplitude of the dipole measured by the Pierre Auger Observatory. We simulated the propagation of five representative stable primaries from nearby galaxies (three active galactic nuclei and 19 starburst galaxies) and from an random distribution of background sources taking into account extragalactic magnetic fields and relevant energy loss processes. The simulations were performed using the state-of-the-art propagation code CRPropa 3. We obtained how the amplitude of the dipole behaves as a function of the energy for three sets of nearby galaxies and three luminosities of the sources so that we could encompass reasonable hypotheses of ultra-high energy cosmic ray sources. We also changed the density of the random distribution of background sources. For each density, a chi-square statistical test was used to compare the amplitude of the dipole obtained from the simulations with the measurements of the Pierre Auger Observatory. The density of background sources was considerably constrained regardless of the source model used.

Keywords: Ultra-high energy cosmic rays. Local sources. Pierre Auger Observatory.

RESUMO

DOURADO, L. A. **Assinaturas de fontes de raios cósmicos ultra-energéticos em medidas de anisotropia de grande escala.**. 2023. 93p. Dissertação (Mestrado em Ciências) - Instituto de Física de São Carlos, Universidade de São Paulo, São Carlos, 2023.

As partículas mais energéticas já detectadas no Universo são os raios cósmicos ultra-energéticos. Essas partículas fascinantes vindas do espaço são compostas por prótons e núcleos mais pesados com energias superiores a 1 EeV (10^18 eV). A identificação das fontes astrofísicas que aceleram esses núcleos até as mais altas energias é dificultada pelos campos magnéticos cósmicos responsáveis pela deflexão de partículas carregadas. Embora as trajetórias dos raios cósmicos ultra-energéticos não apontem diretamente para os locais de aceleração, a distribuição de suas direções de chegada pode fornecer informações essenciais para entender sua origem. Em particular, o Observatório Pierre Auger mediu recentemente uma modulação dipolar nas anisotropias de grande escala, apontando quase na direção oposta ao Centro Galáctico, o que é uma evidência importante de origem extragaláctica das partículas. Neste trabalho, aprofundamos a compreensão sobre o impacto das hipóteses astrofísicas na modelagem da amplitude do dipolo medida pelo Observatório Pierre Auger. Simulamos a propagação de cinco primários estáveis representativos de galáxias próximas (três núcleos ativos de galáxias e 19 galáxias de *starburst*) e de uma distribuição aleatória de fontes de fundo, levando em consideração os campos magnéticos extragalácticos e processos relevantes de perda de energia. As simulações foram realizadas usando o código de propagação CRPropa 3. Obtivemos como a amplitude do dipolo se comporta em função da energia para três conjuntos de galáxias próximas e três luminosidades das fontes, de modo que pudéssemos abranger hipóteses razoáveis de fontes de raios cósmicos ultra-energéticos. Também modificamos a densidade da distribuição aleatória de fontes de fundo. Para cada densidade, um teste estatístico qui-quadrado foi usado para comparar a amplitude do dipolo obtida nas simulações com as medidas do Observatório Pierre Auger. A densidade de fontes de fundo foi consideravelmente restrita, independentemente do modelo de fonte utilizado.

Palavras-chave: Raios cósmicos ultra-energéticos. Fontes locais. Observatório Pierre Auger.

LIST OF FIGURES

Figure 1 – Schematic representation of the Pierre Auger Observatory. The black circles represent the surface detectors, while the colored circles represent a different fluorescence detector station. The size scale of the observatory is presented on the left. 25
Figure 2 – Schematic representation of the Telescope Array. 27
Figure 3 – Energy spectra of ultra-high energy cosmic rays measured by the Pierre Auger Observatory scaled by the energy squared in the top panel and by the energy cubed in the bottom panel. The red line in the bottom panel represents the fit of Equation 2.1 to the data. The spectral index of each region of the spectrum is also shown in the bottom panel. . . . 28
Figure 4 – Energy spectra measured by the Pierre Auger Observatory (blue squares) and by the Telescope Array (black circles) scaled by energy cubed. The complete view of the sky was considered for each observatory. 29
Figure 5 – Measurements of $\langle X_{\max} \rangle$ (left panel) and $\sigma(X_{\max})$ (right panel) from the Pierre Auger Observatory compared to predictions for proton and iron nuclei of the hadronic interaction models EPOS-LHC, Sibyll 2.3c and QGSJet-II.04. 30
Figure 6 – Measurements of $\langle X_{\max} \rangle$ (left panel) and $\sigma(X_{\max})$ (right panel) from the Telescope Array compared to predictions of the hadronic interaction model Sibyll 2.3d. 31
Figure 7 – Comparison between measurements of $\langle X_{\max} \rangle$ (left panel) and $\sigma(X_{\max})$ (right panel) from the Telescope Array and the data of the Pierre Auger Observatory transfered into the Telecospe Array detector (AugerMix). . 31
Figure 8 – Map in galactic coordinates of flux of ultra-high energy cosmic rays with energies above 8 EeV measured by the Pierre Auger Observatory. . 32
Figure 9 – Amplitude of the dipole as a function of the energy of particles measured by the Pierre Auger Observatory and other observatories. 33
Figure 10 – Phase of the dipole as a function of the energy of particles measured by the Pierre Auger Observatory and other observatories. 34
Figure 11 – Hillas diagram. 37
Figure 12 – The evolution of the restrained distance to nearest source, $D^{3\sigma}_{\min}$, with relation to the field strength, B. 39
Figure 13 – Plots showing the disappearance of the 99% GOF contours as the distance to the first source is increased up to 81 Mpc. 40
Figure 14 – Plots showing the disappearance of the 99% GOF contours as the distance to the first source is increased up to 81 Mpc. 41

Figure 15 – Evolution of the amplitude of the dipole with energy for proton as primary. 42
Figure 16 – Evolution of the amplitude of the dipole with energy for iron as primary. 43
Figure 17 – The percentage contribution to the observed flux of ultra-high energy cosmic rays originating from several distance bins as a function of energy. 44
Figure 18 – Sky projection in Galactic coordinates of the position of the three active galactic nuclei (pink star symbols) and the 19 starburst galaxies (blue star symbols) considered as local sources in this work. 46
Figure 19 – Galactic coordinates from events originating from different seeds of magnetic fields, with each one represented by a distinct color. 49
Figure 20 – Radial distributions of particles for distinct propagation times. 55
Figure 21 – Integration of the radial distributions. 56
Figure 22 – Parameter space of the 72 phenomenological models of sources considered in this work. 62
Figure 23 – Amplitude of the dipole as a function of the energy for an equal emission of primaries regardless of the astrophysical source. The distinct classes of nearby galaxies and densities of background sources are shown in the plots. The black points with uncertainties are measurements from the Pierre Auger Observatory. (1) 65
Figure 24 – Amplitude of the dipole as a function of the energy for an equal emission of primaries regardless of the astrophysical source. The distinct classes of nearby galaxies and densities of background sources are shown in the plots. The black points with uncertainties are measurements from the Pierre Auger Observatory. (1) 66
Figure 25 – Amplitude of the dipole as a function of the energy for an emission proportional to the radio luminosity of each galaxy. The distinct classes of nearby galaxies and densities of background sources are shown in the plots. The black points with uncertainties are measurements from the Pierre Auger Observatory. (1) 67
Figure 26 – Amplitude of the dipole as a function of the energy for an emission proportional to the radio luminosity of each galaxy. The distinct classes of nearby galaxies and densities of background sources are shown in the plots. The black points with uncertainties are measurements from the Pierre Auger Observatory. (1) 68
Figure 27 – Amplitude of the dipole as a function of the energy for an emission proportional to the gamma ray luminosity of each galaxy. The distinct classes of nearby galaxies and densities of background sources are shown in the plots. The black points with uncertainties are measurements from the Pierre Auger Observatory. (1) 69

Figure 28 – Amplitude of the dipole as a function of the energy for an emission proportional to the gamma ray luminosity of each galaxy. The distinct classes of nearby galaxies and densities of background sources are shown in the plots. The black points with uncertainties are measurements from the Pierre Auger Observatory. (1) 70

Figure 29 – Difference between chi-squared and minimum chi-squared values as a function of the density of background sources for an equal emission of primaries regardless of the astrophysical source and the three distinct sets of local sources. In the upper part of the plots, each combination of set of local sources and luminosity of sources is indicated. The black lines only connect the black points obtained by the statistical analysis. 71

Figure 30 – Difference between chi-squared and minimum chi-squared values as a function of the density of background sources for an emission proportional to the radio luminosity and the three distinct sets of local sources. In the upper part of the plots, each combination of set of local sources and luminosity of sources is indicated. The black lines only connect the black points obtained by the statistical analysis. 72

Figure 31 – Difference between chi-squared and minimum chi-squared values as a function of the density of background sources for an emission proportional to the gamma ray luminosity and the three distinct sets of local sources. In the upper part of the plots, each combination of set of local sources and luminosity of sources is indicated. The black lines only connect the black points obtained by the statistical analysis. 73

Figure 32 – Amplitude of the dipole as a function of energy for the second term of the Equation (4.26) equal to zero. The case is illustrated for an equal particle emission regardless of the astrophysical source, with active galactic nuclei as local sources. The colored curved represent four values of the density of background sources, and the black points with uncertainties correspond to measurements from the Pierre Auger Observatory. (1) 85

Figure 33 – Amplitude of the dipole as a function of energy for the second term of the Equation (4.26) equal to zero. The case is illustrated for an equal particle emission regardless of the astrophysical source, with active galactic nuclei and starburst galaxies as local sources. The colored curved represent four values of the density of background sources, and the black points with uncertainties correspond to measurements from the Pierre Auger Observatory. (1) 86

Figure 34 – Amplitude of the dipole as a function of energy for the second term of the Equation (4.26) equal to zero. The case is illustrated for an equal particle emission regardless of the astrophysical source, with starburst galaxies as local sources. The colored curved represent four values of the density of background sources, and the black points with uncertainties correspond to measurements from the Pierre Auger Observatory. (1) . . 87

Figure 35 – Amplitude of the dipole as a function of energy for the second term of the Equation (4.26) equal to zero. The case is illustrated for a particle emission proportional to the radio luminosity, with active galactic nuclei as local sources. The colored curved represent four values of the density of background sources, and the black points with uncertainties correspond to measurements from the Pierre Auger Observatory. (1) . . 88

Figure 36 – Amplitude of the dipole as a function of energy for the second term of the Equation (4.26) equal to zero. The case is illustrated for a particle emission proportional to the radio luminosity, with active galactic nuclei and starburst galaxies as local sources. The colored curved represent distinct values of the density of background sources, and the black points with uncertainties correspond to measurements from the Pierre Auger Observatory. (1) 89

Figure 37 – Amplitude of the dipole as a function of energy for the second term of the Equation (4.26) equal to zero. The case is illustrated for a particle emission proportional to the radio luminosity, with starburst galaxies as local sources. The colored curved represent four values of the density of background sources, and the black points with uncertainties correspond to measurements from the Pierre Auger Observatory. (1) 90

Figure 38 – Amplitude of the dipole as a function of energy for the second term of the Equation (4.26) equal to zero. The case is illustrated for a particle emission proportional to the gamma ray luminosity, with active galactic nuclei as local sources. The colored curved represent four values of the density of background sources, and the black points with uncertainties correspond to measurements from the Pierre Auger Observatory. (1) . . 91

Figure 39 – Amplitude of the dipole as a function of energy for the second term of the Equation (4.26) equal to zero. The case is illustrated for a particle emission proportional to the gamma ray luminosity, with active galactic nuclei and starburst galaxies as local sources. The colored curved represent four values of the density of background sources, and the black points with uncertainties correspond to measurements from the Pierre Auger Observatory. (1) 92

Figure 40 – Amplitude of the dipole as a function of energy for the second term of the Equation (4.26) equal to zero. The case is illustrated for a particle emission proportional to the gamma ray luminosity, with starburst galaxies as local sources. The colored curved represent four values of the density of background sources, and the black points with uncertainties correspond to measurements from the Pierre Auger Observatory. (1) . . 93

LIST OF TABLES

Table 1 – Information about the nearby active galactic nuclei and starburst galaxies within a distance of 27 Mpc considered as candidate sites in the simulations. 47
Table 2 – Number of detected events in the simulations for each primary and local source. 50
Table 3 – Information about the nearby active galactic nuclei and starburst galaxies within a distance of 27 Mpc considered as candidate sites in the simulations. 51
Table 4 – Spectral parameters of the combined fit from the Pierre Auger Collaboration used in this work. 52
Table 5 – Values of the size of spherical layers of sources and the corresponding density of background sources. 58
Table 6 – Minimum chi-squared value for each phenomenological model of set of local sources and luminosity. 64
Table 7 – Value of the density of background sources that better describe measurements of the Pierre Auger Observatory, $\rho_{\rm best}$, and the lower and upper limits of the density of background sources within a 3σ of confidence level, $\rho^{3\sigma}_{\rm min}$ and $\rho^{3\sigma}_{\rm max}$, for each phenomenological model of set of local sources and luminosity. 64

CONTENTS

1 INTRODUCTION 23

2 MEASUREMENTS OF ULTRA-HIGH ENERGY COSMIC RAYS . . 25
2.1 Pierre Auger Observatory 25
2.2 Telescope Array 26
2.3 Energy spectrum 27
2.4 Mass composition 29
2.5 Distribution of arrival directions 30

3 THE ORIGIN AND PROPAGATION OF ULTRA-HIGH ENERGY COSMIC RAYS 35
3.1 Top-down models 35
3.2 The Hillas criterion 35
3.3 Acceleration of non-thermal particles 37
3.3.1 Second order Fermi acceleration 37
3.3.2 First order Fermi acceleration 38
3.4 Need for local sources 38

4 METHODOLOGY 45
4.1 Simulations of particles from local sources 46
4.2 Simulations of particles from background sources 53
4.3 Combining results from local and background sources 58
4.4 Statistical analysis 60

5 THE AMPLITUDE OF THE DIPOLE 61
5.1 The amplitude of the dipole for distinct sets of local sources and luminosities 61
5.2 The amplitude of the dipole and the density of background sources 63

6 CONCLUSIONS AND PERSPECTIVES 75

REFERENCES 77

APPENDIX 83

APPENDIX A – RESULTS OF THE AMPLITUDE OF THE DIPOLE 85

1 INTRODUCTION

The most energetic particles ever detected in the Universe are ultra-high energy cosmic rays. These fascinating particles of extraterrestrial origin are protons and heavier nuclei with energies exceeding 1 EeV (10^{18} eV). There are several open questions surrounding these highly energetic particles. (2) For instance, a mystery that remains in Astroparticle Physics is the origin of ultra-high energy cosmic rays. Their detection does not provide direct information about the astrophysical sources that accelerate these nuclei to the highest energies.

The arrival directions of ultra-high energy cosmic rays do not point towards astrophysical sources, since charged particles are deflected by cosmic magnetic fields. Our limited knowledge of extragalactic magnetic fields is an obstacle to reconstruct the path taken by these particles up to the acceleration sites. The detected energy spectrum and mass composition on Earth are also not the same as those emanating from astrophysical sources. Energy losses and changes in chemical composition during propagation occur due to interactions between ultra-high energy cosmic rays and photons from background radiation fields, which play an important role in the propagation of these particles.

The flux of cosmic rays drops orders of magnitude with increasing energy. This results in low statistics for the range in which ultra-high energy cosmic rays belong to. For reference, while the typical order of magnitude for the flux of cosmic rays at the energy of 10^{12} eV is one particle per square meter per second, at the energy of 10^{19} eV the flux drops to a few particles per square kilometer per year. (3) Although the aforementioned features make the study of ultra-high energy cosmic rays quite challenging, there is plenty of space for important discoveries to come out.

Observatories around the world take advantage of Earth's atmosphere to increase the effective detection area of particles. Instead of detecting primary particles that reach the Earth's atmosphere (which have a low flux), ground detectors are constructed to detect the secondary particles generated from interactions between primary cosmic particles and molecules of the atmosphere. This only became possible thanks to the discovery of the so-called extensive air showers, made by Pierre Victor Auger and collaborators in 1939. (4) They noticed a coincident signal in detectors several meters apart, which revealed the complex cascade of particles initiated by a single primary cosmic particle entering Earth's atmosphere.

Named after the French physicist, the Pierre Auger Observatory is the largest cosmic ray observatory in the world. The three fundamental pieces of information that are obtained from the observatory are the energy spectrum, the distribution of arrival

directions and the mass composition of primary particles. Regarding the energy spectrum, Kenneth Greisen (5) and Georgiy Zatsepin alongside Vadim Kuzmin (6) independently predicted in 1966 a cutoff for the energy spectrum of proton around 5×10^{19} eV due to the interaction between these particles and the cosmic microwave background, which was discovered one year before in 1965 by Arno Allan Penzias and Robert Woodrow Wilson. (7) The presence of this radiation background makes the Universe opaque for high energetic particles.

The distribution of arrival directions of cosmic rays is isotropic until the energy of 4×10^{18} eV. (8) The Pierre Auger Collaboration identified a large-scale anisotropy of cosmic rays above the energy of 8×10^{18} eV. (8) The distribution of arrival direction is described by a monopole term plus a dipole term that points approximately in the opposite direction of the Galactic Center. This is an important evidence of an extragalactic origin of these particles. If ultra-high energy cosmic rays had a Galactic origin, one would expect at first a higher flux coming from the Galactic Center due to our particular position in the Galaxy. The Pierre Auger Collaboration also calculated the amplitude and the phase of the dipole as a function of the particle energy in reference (1). They found that the amplitude of the dipole increases with energy, which also corroborates the extragalactic origin of these particles.

This work aims to study the amplitude of the dipole to obtain important information about the astrophysical sources of ultra-high energy cosmic rays. We simulated the propagation of particles coming from active galactic nuclei and starburst galaxies within a distance of 27 Mpc and from a randomly distribution of background sources. The innovation implemented in this work was the combined use of two simulations techniques to take into account nearby and distant sources. The method we introduced guarantees a precise description of the nearby sources and a viable simulation time by using an analytical approach for distant sources.

We calculated the resulting dipole and compared with the measurements of the Pierre Auger Observatory. In particular, we obtained a range on the density of background sources without making too strong astrophysical hypotheses. Having such information about the sources is extremely important, since it can help us to eliminate proposed models of particle acceleration in astrophysical sources.

2 MEASUREMENTS OF ULTRA-HIGH ENERGY COSMIC RAYS

2.1 Pierre Auger Observatory

The Pierre Auger Observatory (Auger) (9) is the largest observatory dedicated to the detection of ultra-high energy cosmic rays. It has an area of 3,000 square kilometers with 27 fluorescence detectors (FD) and 1,660 surface detectors (SD) at a distance of 1,500 meters apart of each other. The detectors are located in a vast plain known as Pampa Amarilla in the city of Malargüe in Argentina. In particular, Figure 1 shows a schematic representation of the observatory.

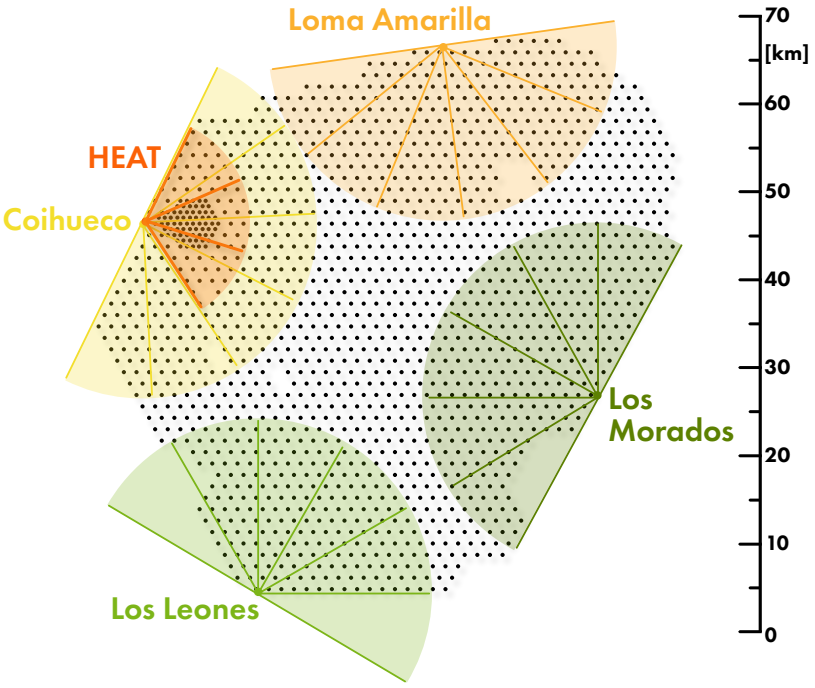

Figure 1 – Schematic representation of the Pierre Auger Observatory. The black circles represent the surface detectors, while the colored circles represent a different fluorescence detector station. The size scale of the observatory is presented on the left.

Source: By the author.

In essence, the surface detectors are large tanks filled with highly purified water that detect secondary particles through their interactions with the water. Charged particles that travel through a dielectric medium at a speed greater than the phase velocity of light in that medium emit an electromagnetic radiation named Cherenkov radiation. This radiation is detected by three photomultipliers tubes inside each detector, which convert light into electrical signals.

Four stations of fluorescence detectors – Los Morados, Los Leones, Loma Amarilla and Coihueco – are located around the surface detectors. They detect the fluorescence radiation in the ultraviolet range from interactions mainly between atmospheric nitrogen and these highly energetic particles. After the detection, data from each surface and fluorescence detectors is combined to reconstruct the event and obtain important details about the primary particle, such as their energy, arrival direction, and composition.

The construction of the Pierre Auger Observatory began shortly after its foundation in 1999 and finished in 2008. However, it has been constantly updated over the years. For instance, the AugerPrime is a current upgrade of the Pierre Auger Observatory. The main purpose of the ongoing upgrade is to improve the mass composition sensitivity of the surface detectors through precise measurements of the muonic and electromagnetic components of extensive air showers. Additional scintillator and radio detectors are being installed on top of surface detector stations, besides updated surface detector electronics and underground muon detectors.

2.2 Telescope Array

The Telescope Array (TA) (10) is another important ultra-high energy cosmic ray observatory and is located in the high desert in Millard County in United States. The surface array samples events across 780 square kilometers of desert. It consists of more than 500 scintillator detectors arranged in a square grid pattern with a spacing of 1.2 kilometers between each detector. The scintillators detectors are made by a material that absorb part of the energy of secondary particles of extensive air showers and emit light in the ultraviolet frequency. This light is also detected by photomultiplier tubes. Furthermore, there are three telescope stations – Black Rock Mesa, Long Ridge and Middle Drum – on a 30 km triangle that have from 12 to 14 telescopes each. The Telescope Array has been collecting data since 2007. Figure 2 shows a schematic representation of the observatory.

Understanding data from the Telescope Array and the Pierre Auger Observatory together would represent a significant advancement in the research of ultra-high energy cosmic rays. This is important not only because each observatory is exposed to complementary regions of the sky, but also because they employ complementary techniques. However, distinctions between the Telescope Array and the Pierre Auger Observatory make their measurements not directly comparable. For this reason, joint working groups of the two observatories were formed to compare results of the energy spectrum, distribution of arrival directions and mass composition by considering the details of each data analysis.

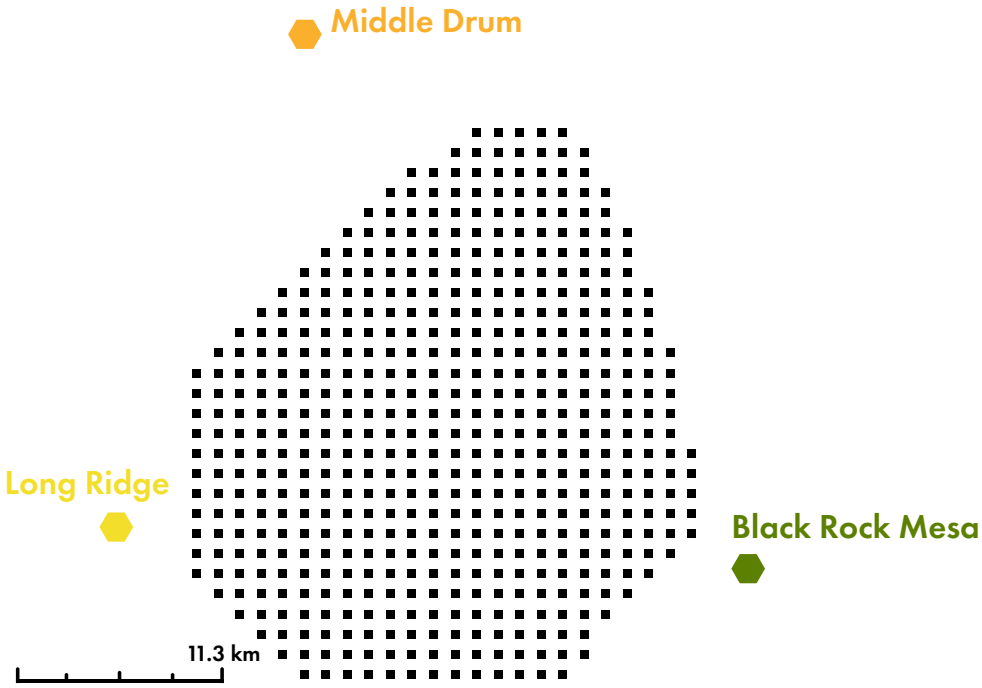

Figure 2 – Schematic representation of the Telescope Array.

Source: By the author.

2.3 Energy spectrum

The energy spectrum is an important information about ultra-high energy cosmic rays. Figure 3 shows the flux of these particles measured by Pierre Auger Observatory scaled by E^2 (top panel) and by E^3 (bottom panel). There are some spectral features that can be noticed in the energy spectrum. In general, the spectrum of cosmic rays can be described as a power law in energy. However, (11) fitted the measurements from Pierre Auger Observatory using a more complex function that is a sequence of four power laws with smooth transitions,

$$J(E) = J_0 \left(\frac{E}{10^{18.5}\,\mathrm{eV}}\right)^{-\gamma_1} \prod_{i=1}^{3} \left[1 + \left(\frac{E}{E_{ij}}\right)^{1/\omega_{ij}}\right]^{(\gamma_i - \gamma_j)\omega_{ij}} . \tag{2.1}$$

The ankle in $(5.0 \pm 0.1 \pm 0.8) \times 10^{18}$ eV (systematic and statistical uncertainties) is a spectral feature consisting of the hardening of the spectrum. The exact cause of the ankle feature is an open question. It is probably related to a transition between cosmic rays of galactic and extragalactic origins. Moreover, there is a suppression in two steps in the spectrum. The spectrum softens from $\gamma_2 = 2.51 \pm 0.03 \pm 0.05$ to $\gamma_3 = 3.05 \pm 0.05 \pm 0.10$ at $E_{23} = (13 \pm 1 \pm 2) \times 10^{18}$ eV and then there is an another suppression at energy of $E_{34} = (46 \pm 3 \pm 6) \times 10^{18}$ eV with $\gamma_4 = 5.1 \pm 0.3 \pm 0.1$. The spectral index of each range

of the spectrum can be seen in Figure 3.

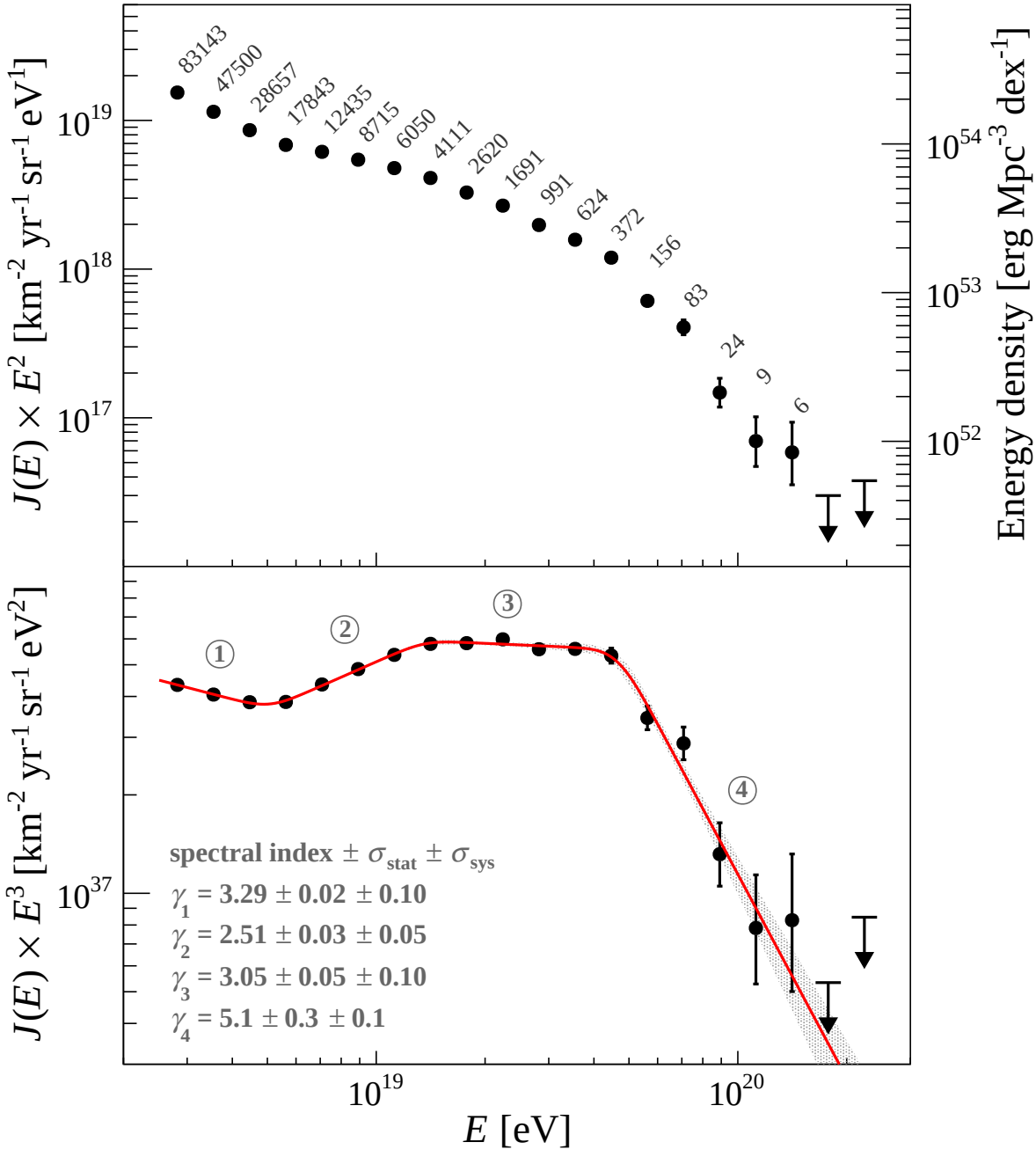

Figure 3 – Energy spectra of ultra-high energy cosmic rays measured by the Pierre Auger Observatory scaled by the energy squared in the top panel and by the energy cubed in the bottom panel. The red line in the bottom panel represents the fit of Equation 2.1 to the data. The spectral index of each region of the spectrum is also shown in the bottom panel.

Source: AAB *et al.* (11)

The Telescope Array also obtained the energy spectrum of the ultra-high energy

cosmic rays. Figure 4 illustrates the spectra of the Telescope Array and the Pierre Auger Observatory overlapped. (12) The energy spectrum measurements from both observatories are compatible with each other up to 10 EeV. However, there are some significant discrepancies at higher energies that cannot be explained by systematic and statistical uncertainties, which is probably related to the fact that the Pierre Auger Observatory and the Telescope Array do not observe the same part of the sky.

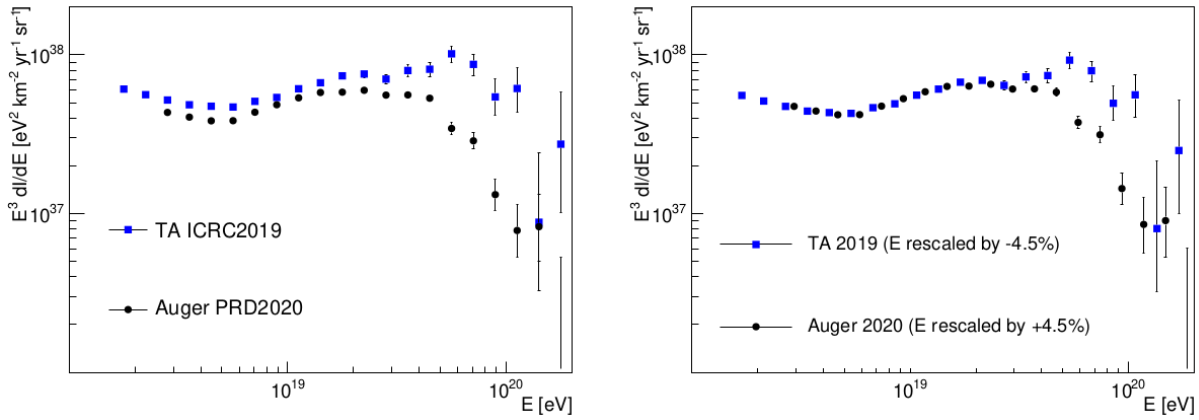

Figure 4 – Energy spectra measured by the Pierre Auger Observatory (blue squares) and by the Telescope Array (black circles) scaled by energy cubed. The complete view of the sky was considered for each observatory.

Source: AAB *et al.* (12)

2.4 Mass composition

Figure 5 presents indirect measurements of the mass composition of ultra-high energy cosmic rays from the Pierre Auger Observatory. These results are obtained from inferences from the depth of shower maximum, $X_{\max}$, which refers to the depth at which the energy deposit profile reaches its maximum. In particular, the $X_{\max}$ can be related to the composition of the primary particle that gave rise to the shower. The problem is that we need measurements of hadronic processes in the energy range of EeV to make the exact correlation between the $X_{\max}$ and the mass composition. Therefore, several extrapolations of measurements of the Large Hadron Collider (LHC) for these higher energies are done. (13–15)

Although we do not manage to determine exactly the mass composition of the primary particle, we can noticed a certain trend in the Pierre Auger Observatory measurements, as can be seen Figure 5. From the 10^{17} to $10^{18.2}$ eV, the composition becomes lighter and above this energy it gets heavier, becoming mixed at the highest energies. This can be seen both in the mean $X_{\max}$ and the standard deviation. The same quantities were also measured by the Telescope Array, which is shown in Figure 6.

Comparisons of the first two moments of $X_{\max}$ distributions obtained by the Pierre Auger Observatory and the Telescope Array for energies above $10^{18.2}$ eV were done. In particular, the data of the Pierre Auger Observatory was converted into the Telescope Array detector due to distinct methods of event selection and analysis of both observatories. Figure 7 shows that there are no significant differences between the two observatories, despite differences in energy spectra.

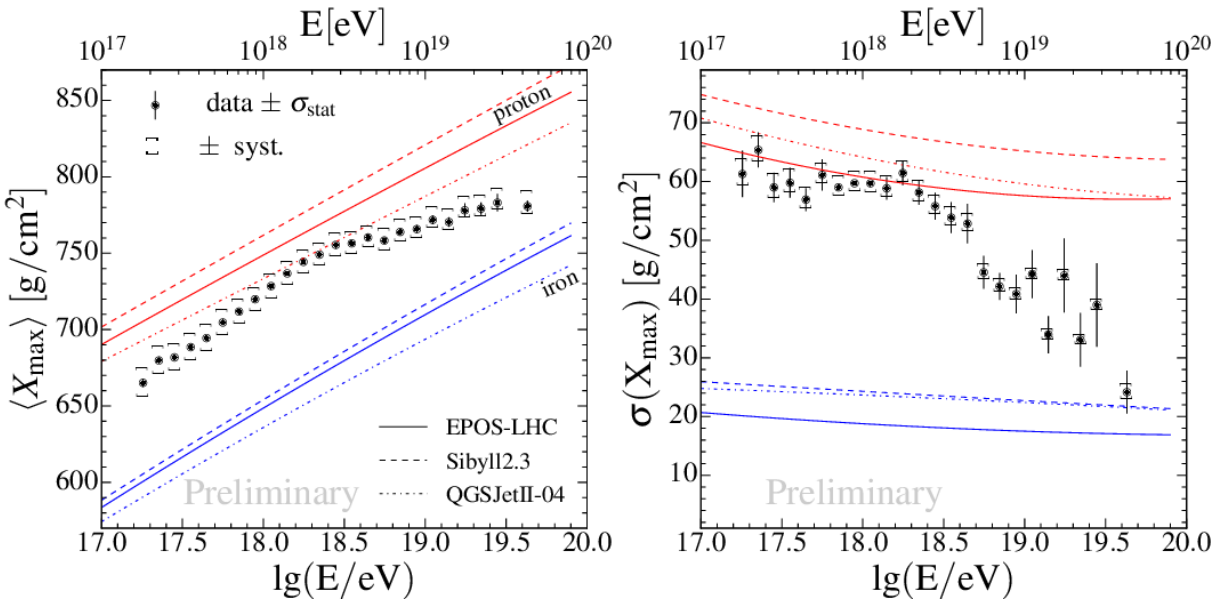

Figure 5 – Measurements of $\langle X_{\max} \rangle$ (left panel) and $\sigma(X_{\max})$ (right panel) from the Pierre Auger Observatory compared to predictions for proton and iron nuclei of the hadronic interaction models EPOS-LHC, Sibyll 2.3c and QGSJet-II.04.

Source: HALIM *et al.* (16)

2.5 Distribution of arrival directions

Above the energy of 4 EeV, the distribution of arrival directions of particles shows a small degree of anisotropy. In essence, there are two ways to search for anisotropies depending on the angular scale of interest. The small-scale anisotropies, also called hotspots, are regions in the sky with a relative excess of events. While the Pierre Auger Observatory measured two hotspots for events with energy above 60 EeV centered approximately at (305°, 25°) and (290°, −70°) in galactic coordinates, (17) the Telescope Array measured one hotspot for events with energy above 57 EeV centered at (146.7°, 43.2°) in equatorial coordinates. (18)

The large-scale anisotropies refer to patterns in the distribution of cosmic ray particles across the entire sky. This can be done by decomposing the distribution of arrival directions into spherical harmonics. In 2017, the Pierre Auger Observatory measured for

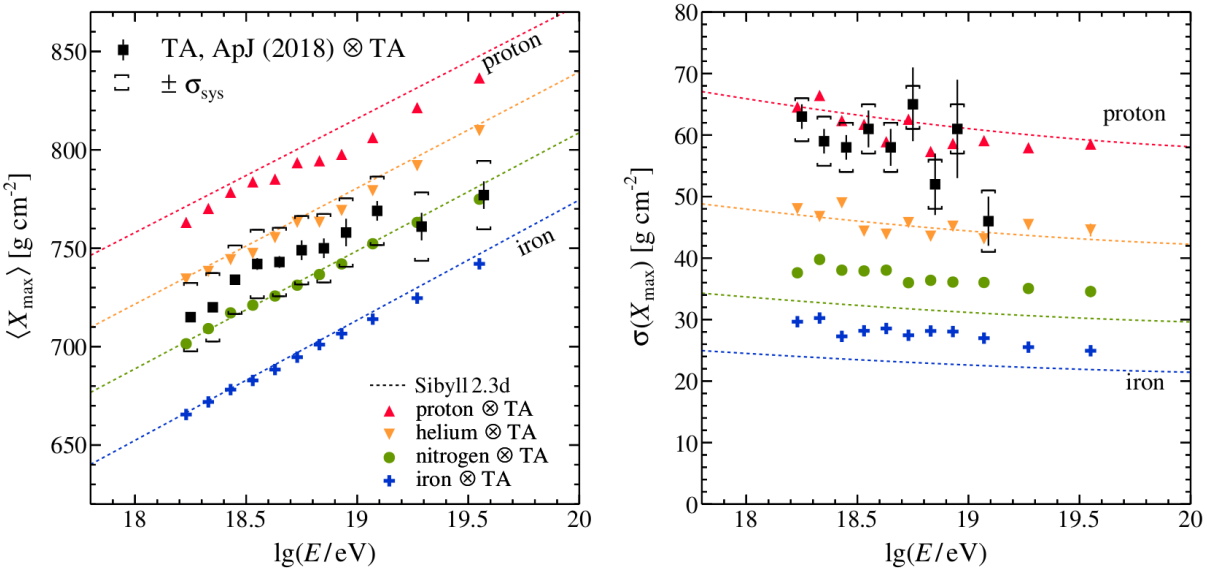

Figure 6 – Measurements of $\langle X_{\max} \rangle$ (left panel) and $\sigma(X_{\max})$ (right panel) from the Telescope Array compared to predictions of the hadronic interaction model Sibyll 2.3d.

Source: HALIM *et al.* (16)

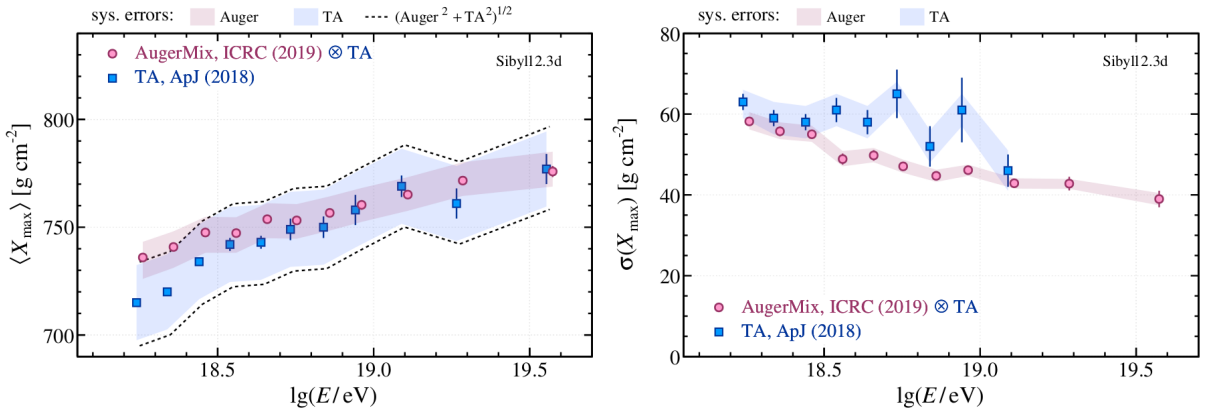

Figure 7 – Comparison between measurements of $\langle X_{\max} \rangle$ (left panel) and $\sigma(X_{\max})$ (right panel) from the Telescope Array and the data of the Pierre Auger Observatory transfered into the Telecospe Array detector (AugerMix).

Source: HALIM *et al.* (16)

events with energies above 8 EeV a dipole with a 5.2σ level of significance. The dipole has an amplitude of $6.5^{+1.3}_{-0.9}\%$ and direction $(100^\circ \pm 10^\circ, -24^{\circ}{}^{+12^\circ}_{-13^\circ})$ in equatorial coordinates, which lies approximately at 125° from the Galactic Center. (8) The sky map showing the cosmic ray flux for energies above 8 EeV can be seen in Figure 8. Besides, further analysis of dipole revealed an even higher statistical significance of 6.6σ in 2021. (19) However, the Telescope Array did not measured the dipolar pattern found by the Pierre Auger

Observatory, which can be an effect of being located in the Northern Hemisphere.

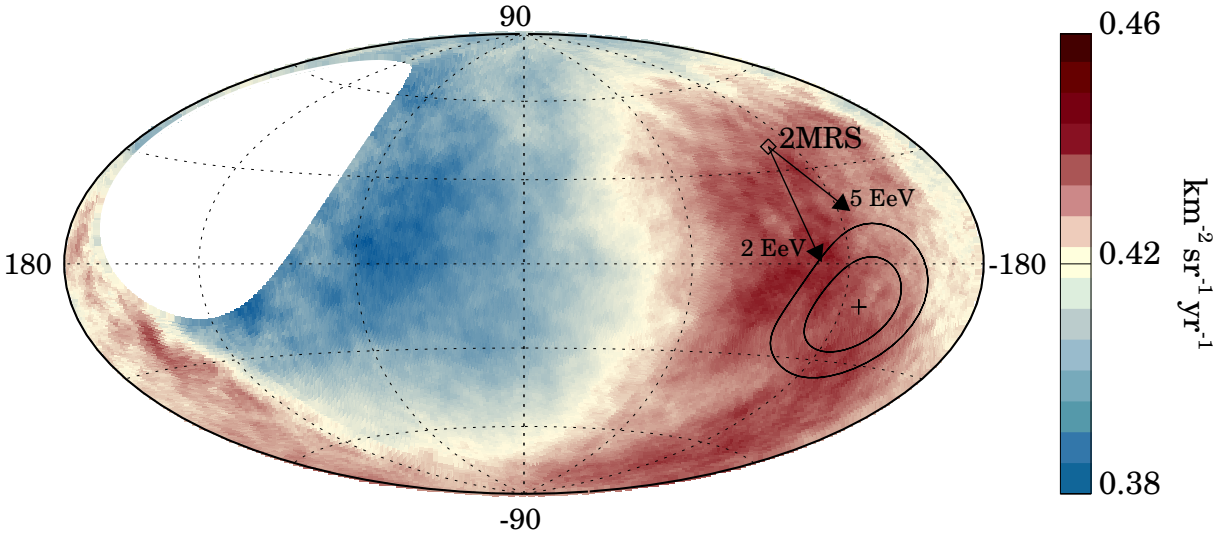

Figure 8 – Map in galactic coordinates of flux of ultra-high energy cosmic rays with energies above 8 EeV measured by the Pierre Auger Observatory.

Source: AAB *et al.* (8)

The amplitude and phase of the dipole as a function of the energy were also obtained by the Pierre Auger Observatory, as can be seen in Figures 9 e 10. (1) For energies below 1 EeV, not only the dipole amplitudes are not significant, but also the phases determined are not far from the Galactic Center. However, evidence of extragalactic origin appears for events above 4 EeV due to the significant amplitude of the dipole and the direction pointing approximately in the opposite direction of the Galactic Center.

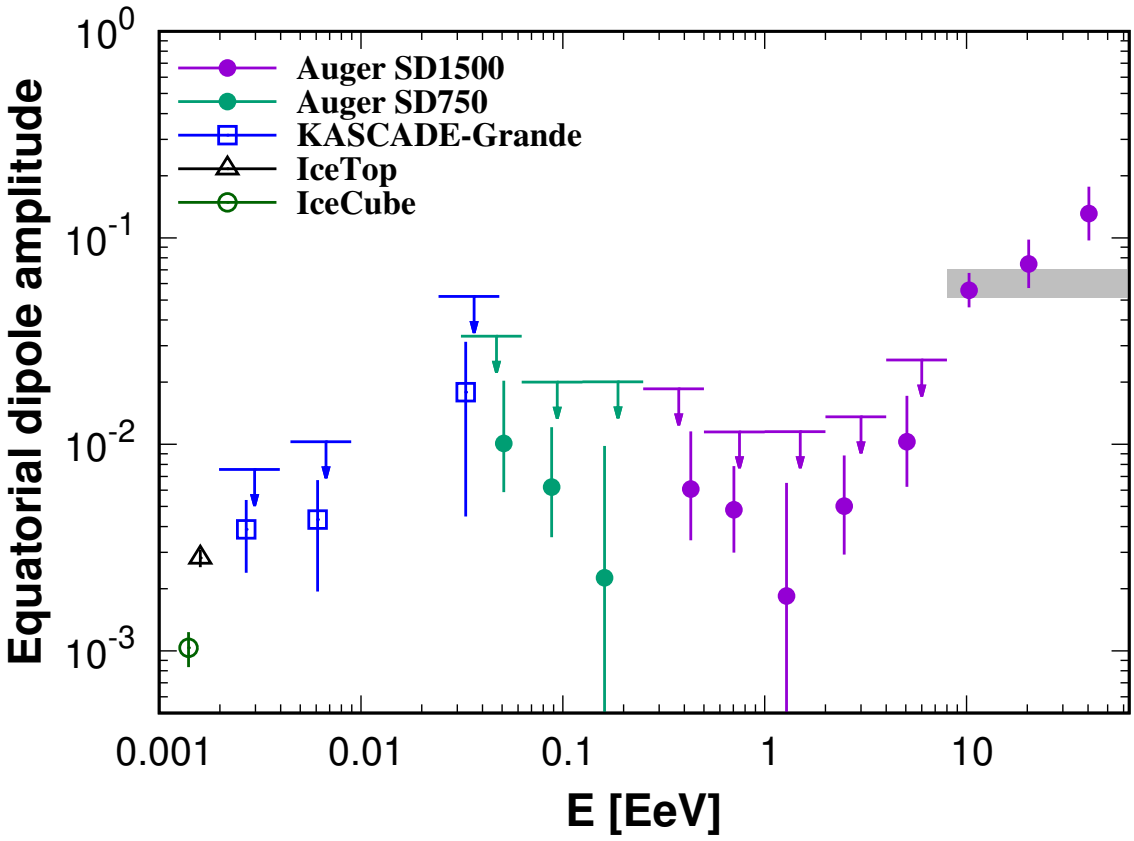

Figure 9 – Amplitude of the dipole as a function of the energy of particles measured by the Pierre Auger Observatory and other observatories.

Source: AAB *et al.* (1)

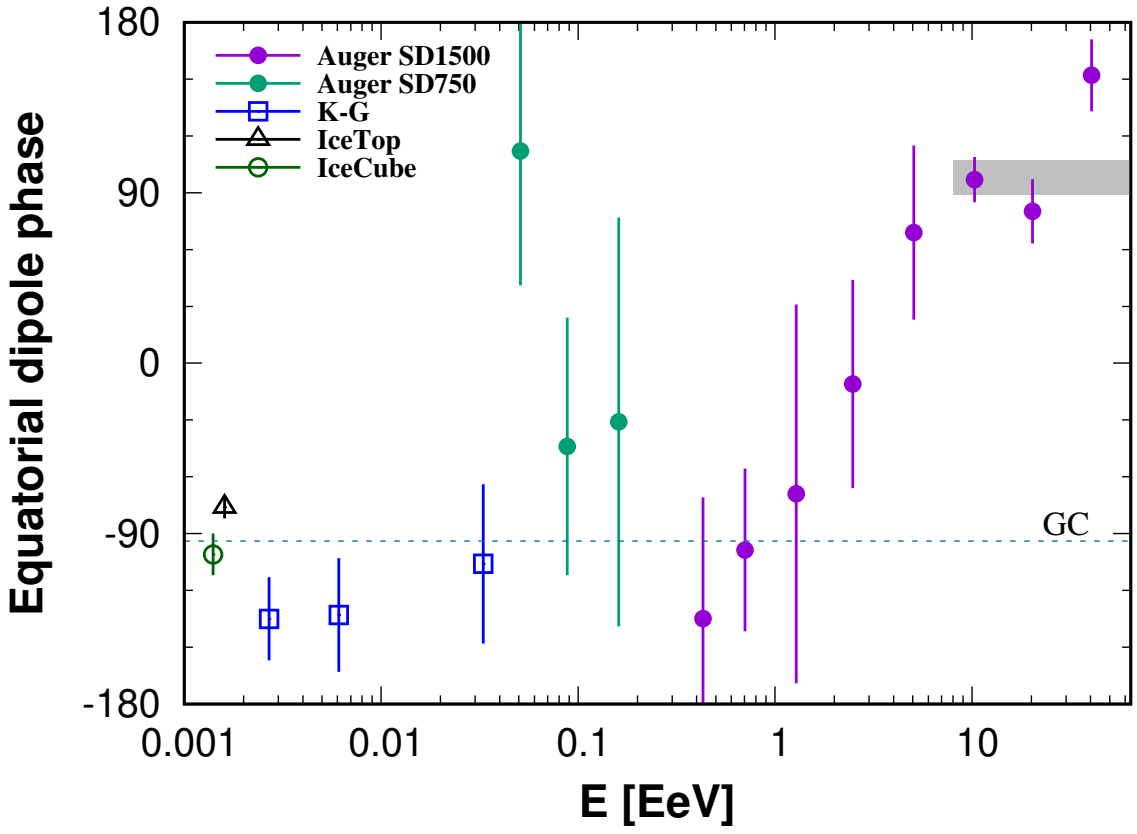

Figure 10 – Phase of the dipole as a function of the energy of particles measured by the Pierre Auger Observatory and other observatories.

Source: AAB *et al.* (1)

3 THE ORIGIN AND PROPAGATION OF ULTRA-HIGH ENERGY COSMIC RAYS

3.1 Top-down models

Top-down models of ultra-high energy cosmic rays are theoretical models that propose that high-energy particles are created through the decay or annihilation of very massive exotic particles, rather than being produced in astrophysical objects. However, these hypotheses have lost relevance, because they do not accurately describe the data on energy spectral index, anisotropy, mass composition and flux of neutrinos and gamma rays measured by the current observatories, such as the Pierre Auger Observatory and the Telescope Array. On the other hand, the so-called bottom-up models of ultra-high energy cosmic rays propose that electromagnetic mechanisms in astrophysical environments are responsible for accelerating these particles to the highest energies.

3.2 The Hillas criterion

The famous Hillas criterion, introduced by (20), is a necessary but not sufficient condition to identify potential candidates as sources of ultra-high energy cosmic rays. It is exclusively based on simple characteristics of astrophysical objects, in particular the typical size R and the typical magnetic field strength B. For particles of charge Ze, where Z is the atomic number of the nucleus and e is the elementary charge, the criterion states that the maximum energy these particles can achieve in a certain accelerator is given by

$$E_{\max} \approx Z \left(\frac{B}{\mu\mathrm{G}}\right) \left(\frac{R}{\mathrm{kpc}}\right) \ \mathrm{EeV}. \tag{3.1}$$

From Equation (3.1), it is evident that the maximum energy is directly proportional to the values of the size and magnetic field of the astrophysical object under analysis. Magnetic fields do not perform work, so charged particles are accelerated by electric fields. The plasma state, which is the predominant form of visible matter in nature, (21) does not permit the maintenance of high voltage drops due to its conductive properties. Consequently, it is the electromotive component of electromagnetic fields, rather than the electrostatic one, that primarily drives particle acceleration in astrophysical environments (22). In addition to their spatial and temporal variations that generate electromotive forces, cosmic magnetic fields also play another crucial role in accelerating cosmic rays. These fields are responsible for trapping particles along magnetic field lines for a duration sufficient for particles to gain energy. In fact, the Hillas criterion was formulated by considering the concept of confining charged particles within an acceleration region.

An important characteristic scale length is the Larmor radius or gyroradius, which describes the radius of the circular or spiral motion of a charged particle in the presence of a homogeneous magnetic field. This quantity is given by

$$R_L = \frac{\gamma m v_\perp}{|q|B} \tag{3.2}$$

in SI units, where γ is the Lorentz factor, m is the mass of the particle, $v_\perp$ is the component of the velocity perpendicular to the direction of the magnetic field, q is the electric charge of the particle, and B is the magnetic field flux density. The Hillas criterion was derived from the energy of an ultra-high energy cosmic ray with a Larmor radius as extensive as the dimensions of the acceleration region. Particles with energy on the order of the maximum energy given by Equation (3.1) will eventually escape from their sources, as magnetic fields can no longer confine them.

For ultra-high energy cosmic rays, we are interested in candidate sources capable of accelerating particles to the highest energies of the cosmic ray spectrum, such as energies above 100 EeV. The Hillas diagram, shown in Figure 11, presents magnetic field values as a function of the characteristic size of several source classes ($R = l \cdot \Gamma$, with l as the comoving size of the source and Γ as the Lorentz factor of the motion). The parameter β is the typical velocity of magnetic field variations as a fraction of the velocity of light, which can dilute the maximum achievable energy presented in Equation (3.1). The diagonal lines delimit the Hillas criterion for a maximum energy of $E_{\max} = 100$ EeV, given the cosmic ray nuclei and the velocity of magnetic field variations. Whereas the red (blue) lines depict proton (iron) nuclei, the solid (dashed) lines represent $\beta = 1.0$ ($\beta = 0.01$).

The parameters of magnetic field and characteristic size of the source are degenerate. On the one hand, we can have large objects with a weak magnetic field, such as galaxies clusters, satisfying the Hillas criterion. On the other hand, we can also have tiny objects with strong magnetic fields as possible candidates, such as neutron stars and magnetars. Active galactic nuclei (*AGN knots*, *AGN hotspots*, and *AGN Hotspots* (23,24)) and starburst galaxies (*Starburst winds* (25)) are among some of the astrophysical objects displayed in the Hillas diagram that satisfy the criterion. These two classes of galaxies are the same ones whose directions presented a correlation with measurements of the distribution of arrival directions from the Pierre Auger Observatory, as discussed in Section 2.5, which makes them candidates with great potential to be sources of ultra-high energy cosmic rays.

Finally, particular attention must be given to aspects not included in the original Hillas criterion. For instance, it does not account for interactions between cosmic rays and photons during acceleration and propagation. It is possible that particles may not reach the maximum energy given by Equation (3.1) due to energy loss processes occurring

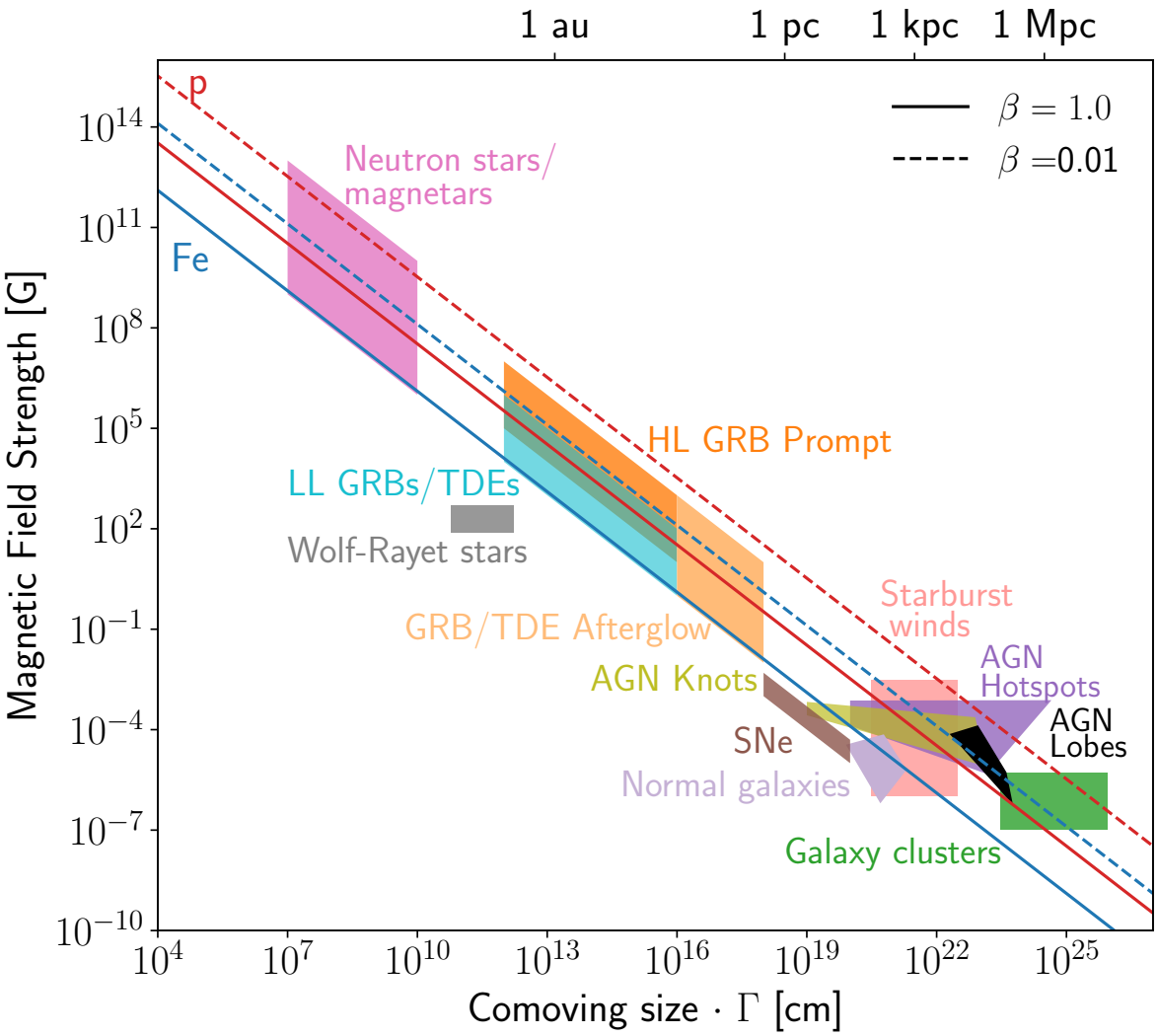

Figure 11 – Hillas diagram.

Source: BATISTA *et al.* (2)

within the sources themselves. For updated results on the Hillas criterion considering radiation losses, refer to (24). Moreover, the mass composition of ultra-high energy cosmic rays becomes heavier with increasing energy, as discussed in Section 2.4. Therefore, it is also important to consider sources that do not have radiation fields intense enough to considerably photodisintegrate nuclei (26).

3.3 Acceleration of non-thermal particles

3.3.1 Second order Fermi acceleration

The original version of Fermi acceleration, known as second-order Fermi acceleration, is an important stochastic acceleration process formulated by Enrico Fermi in 1949. (27) In this mechanism, particles undergo repeated reflections within the so-called

magnetic mirrors in a particular astrophysical medium. Depending on the nature of the collisions with magnetic clouds, particles can either gain or lose energy. However, head-on collisions are commonly preferred as they have a higher likelihood of occurring. (28) Consequently, the rate at which particles gain energy is proportional to

$$\left\langle \frac{\Delta E}{E} \right\rangle = \frac{8}{3} \left(\frac{V}{c} \right)^2, \tag{3.3}$$

where V is the typical velocity of the mirrors and c is the speed of light. This mechanism is named "second order" because particle energy increases in proportion to the square of the velocity of the moving clouds. Due to this proportionality, the second order Fermi acceleration is not a very efficient mechanism for energizing particles. However, it inspired further works to explain what it is measured on Earth.

3.3.2 First order Fermi acceleration

The essence of the original Fermi mechanism written in a slightly different way can leads to the first order Fermi acceleration. For particles crossing from the upstream to the downstream side of the shock, a process known as diffusive shock acceleration (DSA) might occur. DSA is believed to be the primary mechanism through which particles acquire non-thermal energies in astrophysical shock waves. This process is characterized by a fractional energy increase that is proportional to

$$\frac{\Delta E}{E} \propto \frac{V}{c}. \tag{3.4}$$

The fractional energy increase is of first order in V/c, hence appropriately referred to as first-order Fermi acceleration. This acceleration mechanism in the presence of strong shock waves was independently discovered by several researchers in the late 1970s. (29–33) Furthermore, the central characteristic of this process is that the acceleration at the first order results in the formation of a power-law energy spectrum with an energy spectral index of approximately 2.

3.4 Need for local sources

Even if a specific astrophysical source can emit particles at ultra-high energies, these particles may not necessarily be responsible for what we measure on Earth due to propagation effects, such as energy loss processes. The need of local sources, which are located within a distance of approximately 100 Mpc from Earth (34), arises from the combination of the effects of ultra-high energy cosmic ray propagation with measurements from observatories, such as the Pierre Auger Observatory and the Telescope Array. Therefore, we discuss below several pieces of evidence published in the literature regarding the importance of local sources.

Firstly, (34) fitted the energy spectrum of ultra-high energy cosmic rays for distinct nuclei as a function of the distance from the nearest source. It found that beyond a certain distance of the closest source, it is no longer possible to fit the spectrum. This is shown in Figure 12 with the values of the distance to nearest source in which it is possible to fit the spectrum with 3σ of confidence level as a function of the intensity of the magnetic field. It is evident from Figure 12 that it is necessary to have sources closer than 100 Mpc to fit the spectrum, as previously mentioned.

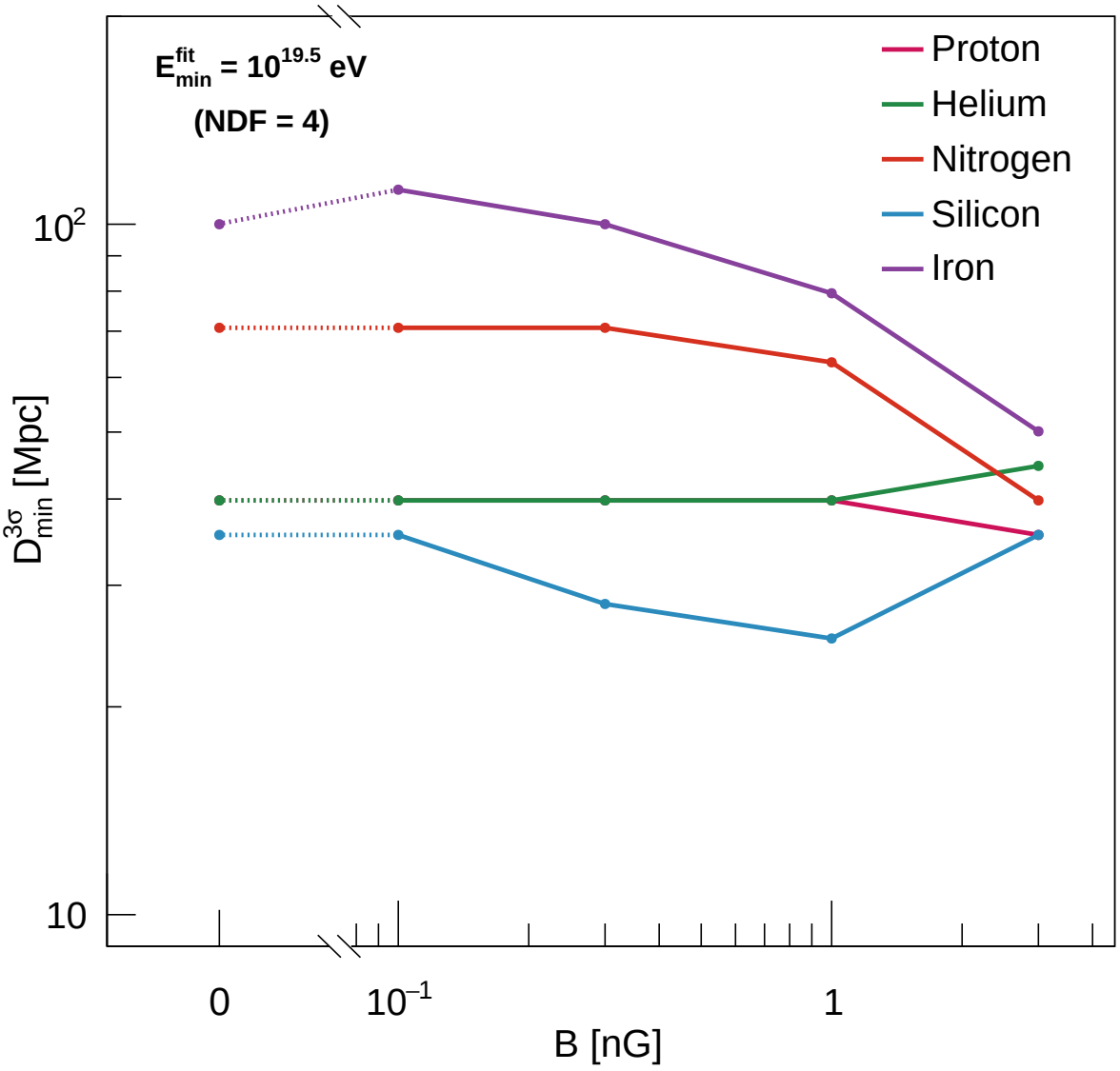

Figure 12 – The evolution of the restrained distance to nearest source, $D^{3\sigma}_{\text{min}}$, with relation to the field strength, B.

Source: LANG *et al.* (34)

A similar study was performed by (26) considering the energy spectrum and the mass composition. In this case, there are two parameters that are taken into account

during the fitting, and it is possible to see in Figures 13 and 14 that as the distance from the nearest source increases, the parameter region that will lead to a spectrum fit decreases. This region practically disappear when the nearest source is above 81 Mpc in Figure 13.

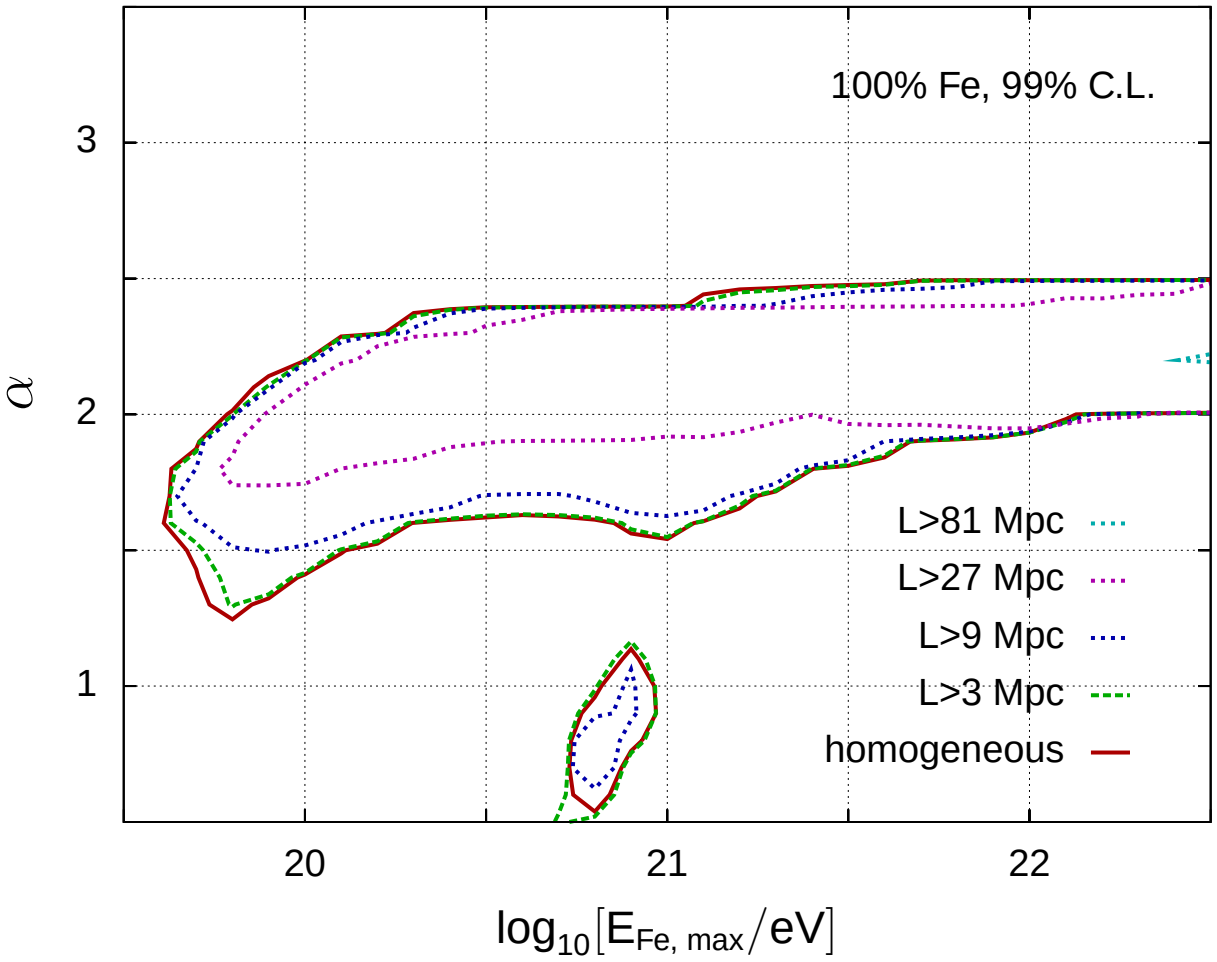

Figure 13 – Plots showing the disappearance of the 99% GOF contours as the distance to the first source is increased up to 81 Mpc.

Source: TAYLOR *et al.* (26)

Studies of large-scale anisotropy in the distribution of arrival directions presented in Figures 15 and 16 the amplitude of the dipole as a function of energy. The curves represent the signal that arises from protons and iron with the distance to the nearest source changing from 3 to 243 Mpc. If a local source does not exist, a description of data is not possible.

To conclude, Figure 17 also corroborates with the scenario of local sources by showing the percentage in which a certain source contribute to the total flux as a function of energy. We can observe that as the energy increases, the closer sources have an increasingly larger contribution to the energy flux.

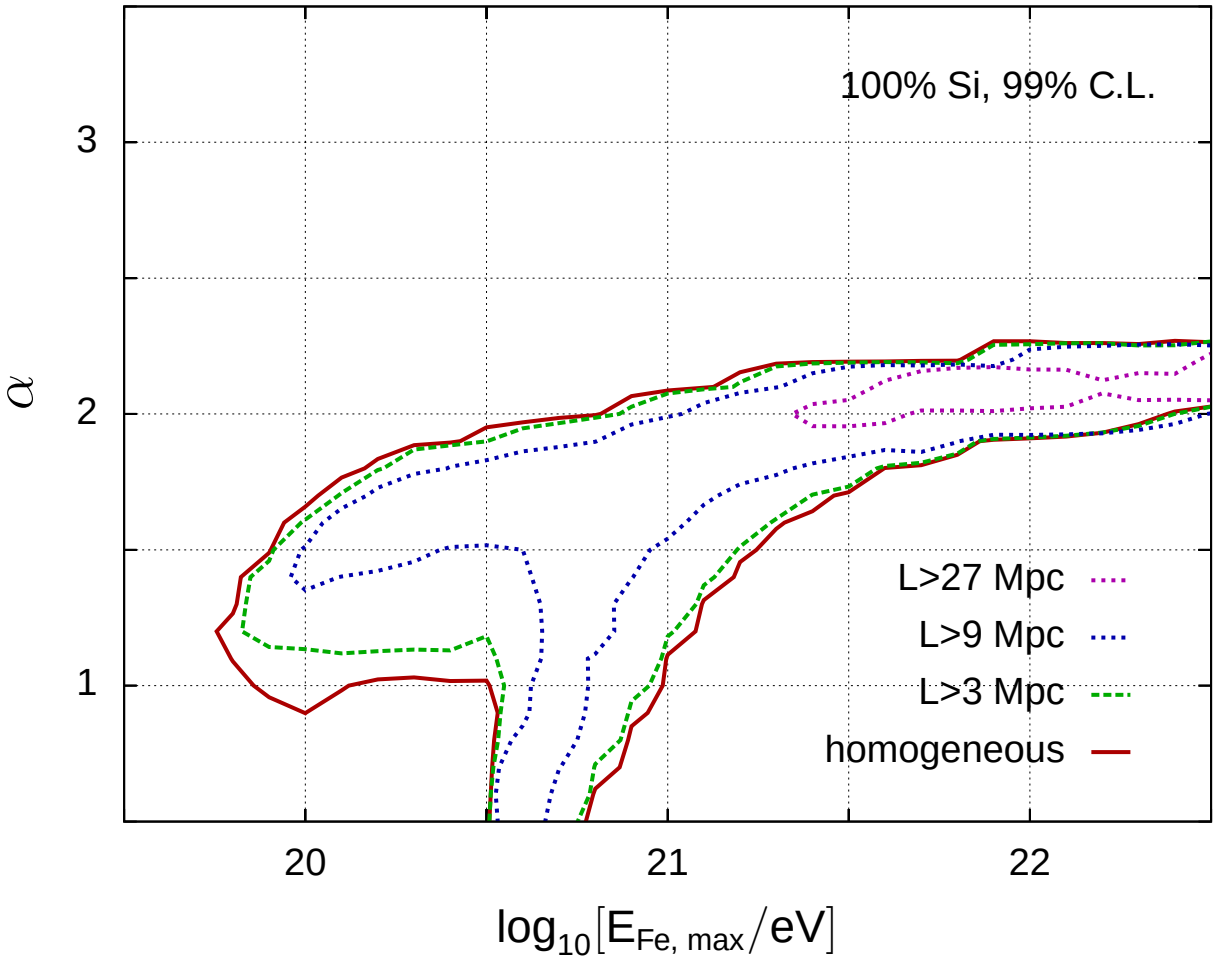

Figure 14 – Plots showing the disappearance of the 99% GOF contours as the distance to the first source is increased up to 81 Mpc.

Source: TAYLOR *et al.* (26)

A similar study was performed by (26) considering the energy spectrum and the mass composition. In this case, there are two parameters that are taken into account during the fitting, and it is possible to see in Figure 13 that as the distance from the nearest source increases, the parameter region that will lead to a spectrum fit decreases. This region practically disappear when the nearest source is above 81 Mpc.

To conclude, Figure 17 also corroborates with the scenario of local sources by showing the percentage in which a certain source contribute to the total flux as a function of energy. We can observe that as the energy increases, the closer sources have an increasingly larger contribution to the energy flux.

All these previous work lead to the need for local sources to explain measurements of ultra-high energy cosmic rays. Besides them, there are several others works, such as (36–40). Therefore, in any study of ultra-high energy cosmic ray sources it is important to describe these sources in simulations, which is what we did in this work.

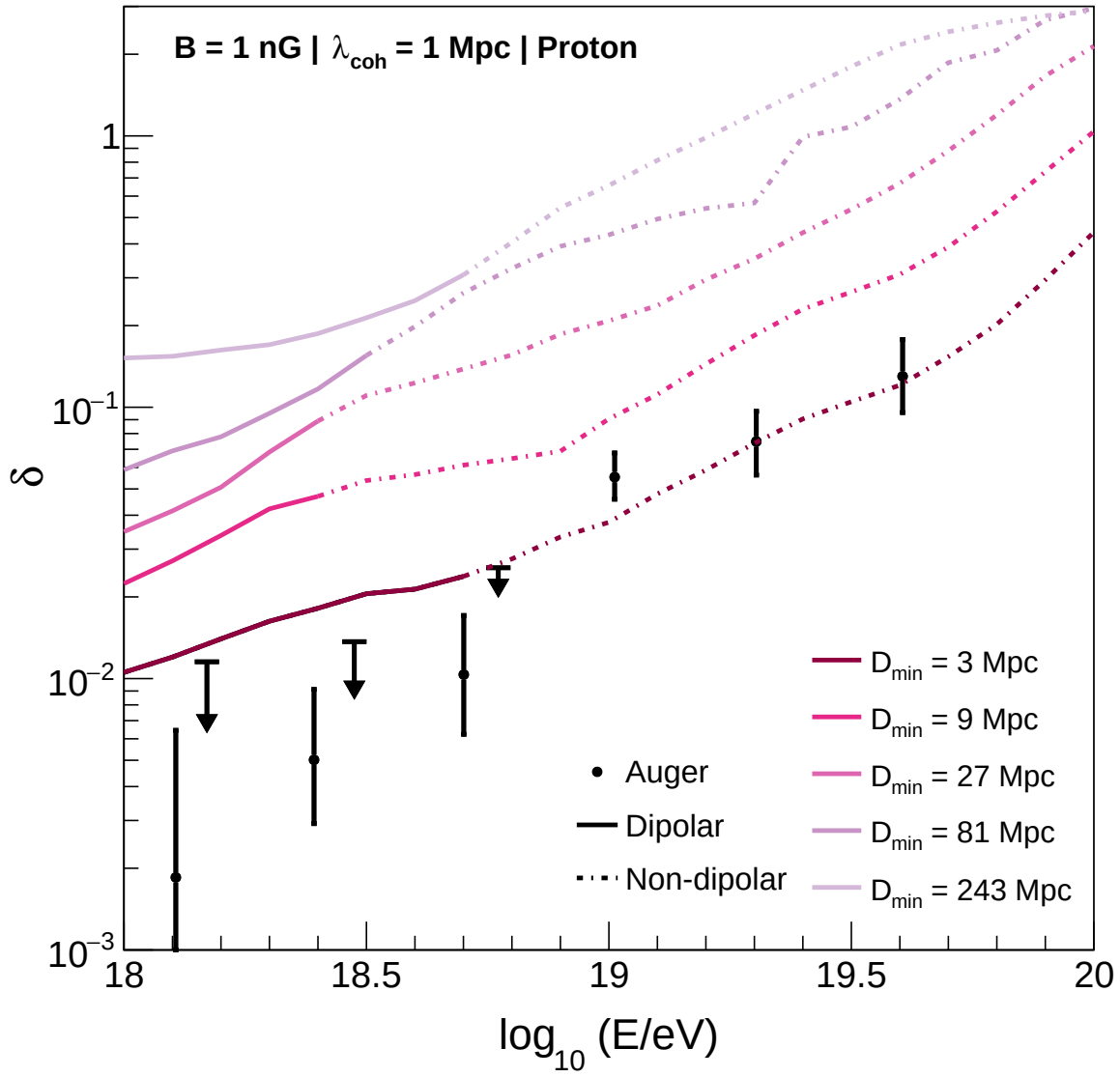

Figure 15 – Evolution of the amplitude of the dipole with energy for proton as primary.

Source: LANG *et al.* (35)

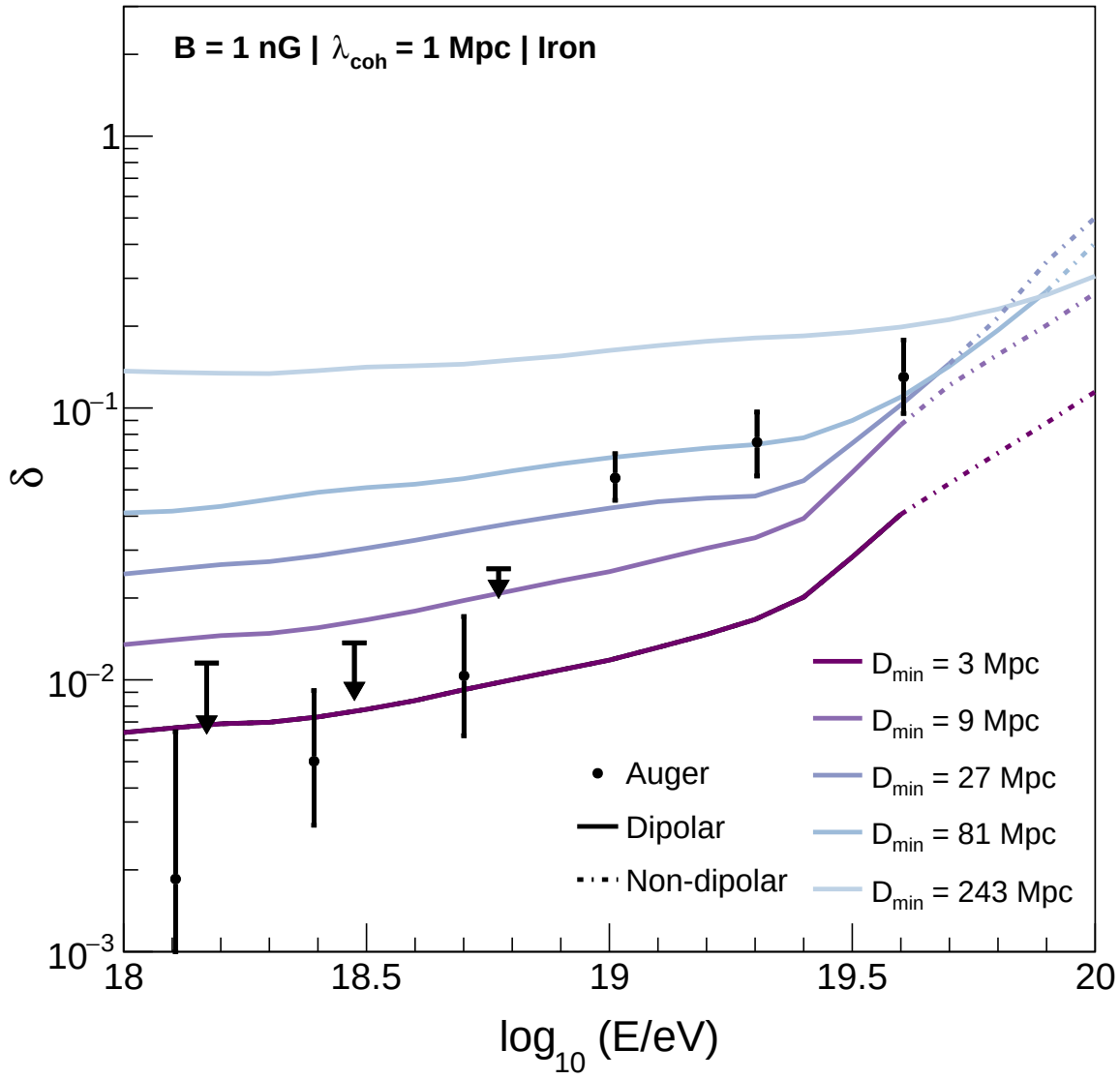

Figure 16 – Evolution of the amplitude of the dipole with energy for iron as primary.

Source: LANG *et al.* (35)

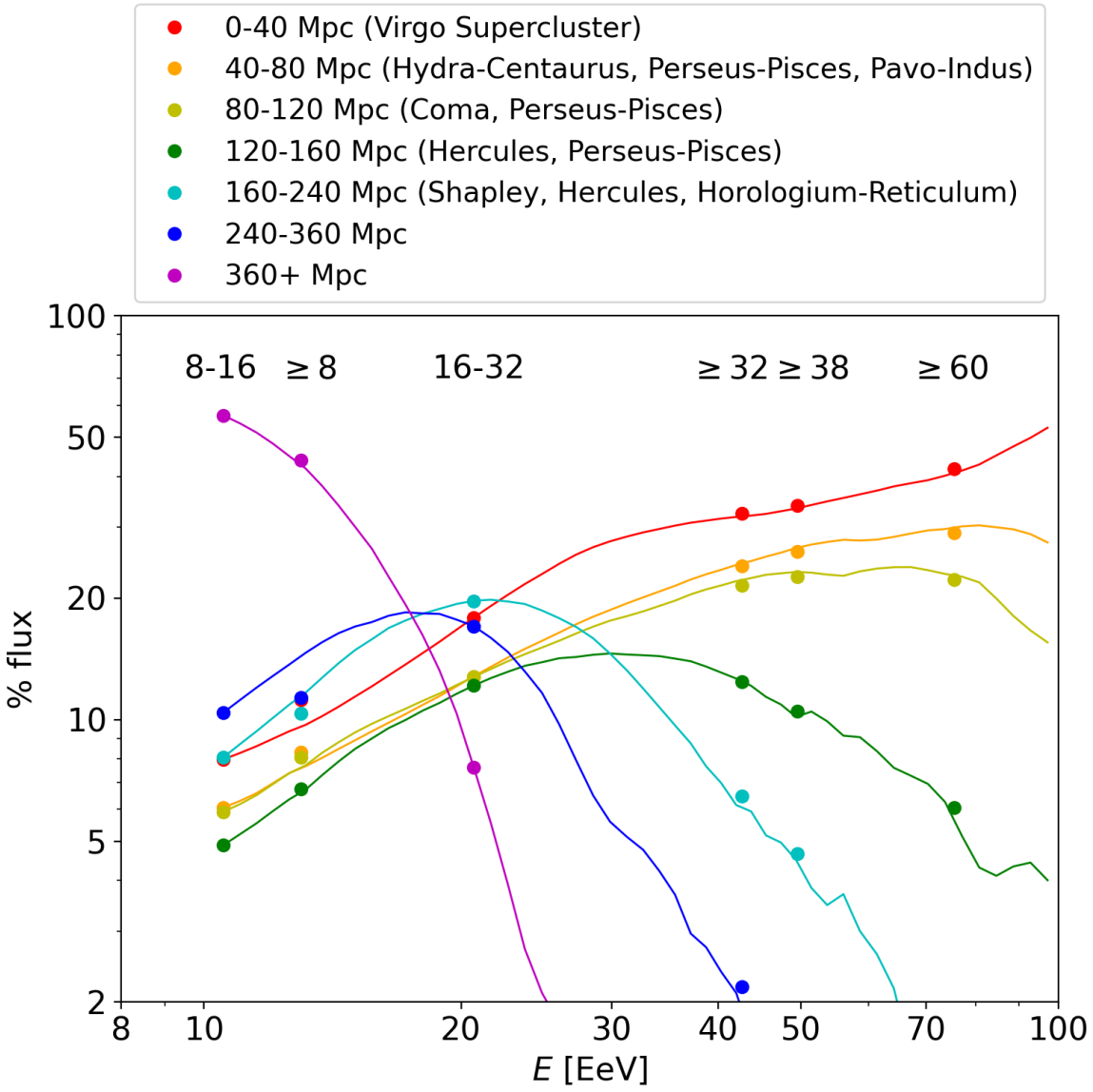

Figure 17 – The percentage contribution to the observed flux of ultra-high energy cosmic rays originating from several distance bins as a function of energy.

Source: DING *et al.* (36)

4 METHODOLOGY

In this work, we studied the amplitude of the dipole of ultra-high energy cosmic rays as a function of the energy with the aim of obtaining information about the origin of these particles. We developed phenomenological models of acceleration sources and extragalactic environments, and compared our results with measurements from the Pierre Auger Observatory. In particular, we considered a combination of local and background sources. We varied the set of local sources three times, chose three luminosity configurations for the sources and adopted eight values for the density of background sources, resulting in a total of 72 distinct models. Details of the specific combinations are presented in section 4.1. While local sources are important for explaining specific experimental results from the Pierre Auger Observatory and the Telescope Array, as discussed in Section 3.4, background sources are also indispensable for studying the amplitude of the dipole, since particles coming from more distant sources mainly contribute to the normalization of this measurement.

Previous works from the Astroparticle Physics Group (APOEMA) investigated the anisotropies measured in the distribution of arrival directions of ultra-high energy cosmic rays. Whereas (41) focused on nearby galaxies within a distance of 23 Mpc to study the direction of the dipole using a Monte Carlo simulation code for propagation of ultra-high energy cosmic rays, (35) obtained the amplitude of the dipole as a function of the energy of particles for an ensemble of randomly distributed sources. The latter work further developed a semi-analytical method that overcomes some computational limitations in simulations of particle propagation from more distant sources. (34) However, (35) did not compare the results obtained with measurements from the Pierre Auger Observatory, since it would require the construction of more realistic models.

Therefore, additional investigation of anisotropies of ultra-high energy cosmic rays and a consistent comparison of the amplitude of the dipole with measurements from the Pierre Auger Observatory are quite natural and even expected. This master's dissertation is a continuation of previous works from APOEMA Group, in particular (34) and (35). We constructed realistic scenarios to further analyze the amplitude of the dipole thanks to the development of the aforementioned methodology in (34) and (35), since it enabled to better include background sources in our phenomenological models. In fact, one of the impacts of this master's dissertation comes from the combination of the two distinct simulation strategies: the Monte Carlo simulation employed in (41) and the semi-analytical method developed in (34) and (35).

4.1 Simulations of particles from local sources

We used the state-of-the-art Monte Carlo code CRPropa 3* (42) in version 3.1.6 to simulate the propagation of ultra-high energy cosmic rays through extragalactic environments coming from local sources. Table 1 provides information about the three active galactic nuclei (AGN) and the 19 starburst galaxies (SBG) within a distance of 27 Mpc considered as candidate sites in these simulations. This set of galaxies is the same one used in (41) and also corresponds to the galaxy ensemble up to 27 Mpc analyzed in (17), with the inclusion of Fornax A. We simulated particles originating from active galactic nuclei and starburst galaxies due to their potential as candidate sources of ultra-high energy cosmic rays, as detailed in Sections 2.5 and 3.2, although there is a certain arbitrariness in the choice of the maximum distance for local sources. The astronomical coordinates of the galaxies were taken from (43) for active galactic nuclei and from (17) for starburst galaxies. The previous works used the standard cosmological model to calculate the distance of the galaxies, and their sky projection in Galactic coordinates is shown in Figure 18.

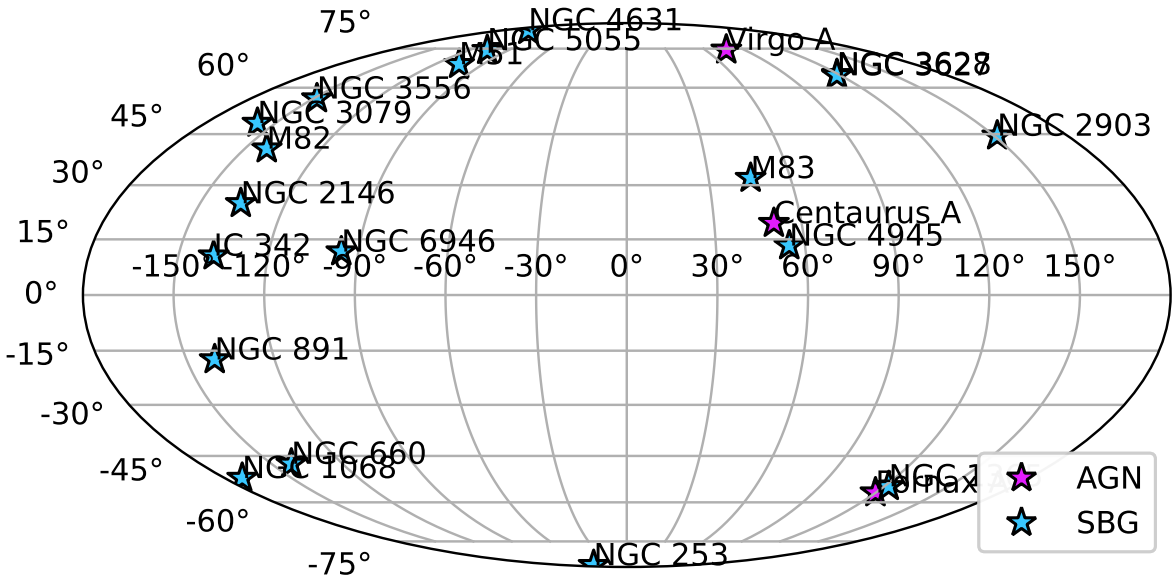

Figure 18 – Sky projection in Galactic coordinates of the position of the three active galactic nuclei (pink star symbols) and the 19 starburst galaxies (blue star symbols) considered as local sources in this work.

Source: By the author.

The emission of particles was isotropic from source positions. Hydrogen (^{1}H), helium (^{4}He), nitrogen (^{14}N), silicon (^{28}Si) and iron (^{56}Fe) were the five representative stable nuclei injected with a power law energy spectrum ranging from 1 to 10^4 EeV and spectral

* https://crpropa.desy.de/

Table 1 – Information about the nearby active galactic nuclei and starburst galaxies within a distance of 27 Mpc considered as candidate sites in the simulations.

Galaxy	Type	Distance [Mpc]	SGB	SGL
Centaurus A	AGN	3.6	-0.092	2.788
Fornax A	AGN	20.9	-0.674	4.556
Virgo A	AGN	18.4	-0.041	1.796
NGC 253	SBG	2.7	-0.088	4.739
M82	SBG	3.6	0.019	0.711
NGC 4945	SBG	4.0	-0.178	2.884
M83	SBG	4.0	0.018	2.581
IC 342	SBG	4.0	0.006	0.185
NGC 6946	SBG	5.9	0.733	0.176
NGC 2903	SBG	6.6	-0.637	1.283
NGC 5055	SBG	7.8	0.249	1.330
NGC 3628	SBG	8.1	-0.317	1.676
NGC 3627	SBG	8.1	-0.322	1.686
NGC 4631	SBG	8.7	0.100	1.470
M51	SBG	10.3	0.302	1.243
NGC 891	SBG	11.0	-0.083	5.986
NGC 3556	SBG	11.4	-0.013	0.995
NGC 660	SBG	15.0	-0.131	5.461
NGC 2146	SBG	16.3	0.073	0.430
NGC 3079	SBG	17.4	-0.149	0.890
NGC 1068	SBG	17.9	-0.451	5.311
NGC 1365	SBG	22.3	-0.715	4.570

Source: By the author.

index of -1. Since the energy of ultra-high energy cosmic rays ranges over many orders of magnitude, it was convenient to use the aforementioned distribution to sample particles in energy rather than an uniform distribution, which would not favor low energy particles. For this reason, we also had to take into account a certain weight relative to the injected spectral index to correct the final flux, besides the usual weight relative to source features.

The domain of the simulations was a cubic box with length of 249.827 Mpc and resolution of 1024 for each dimension. The detector was placed in the center of the domain as a sphere of radius of 100 kpc. Particles with energies below 1 EeV were deactivated.

Furthermore, a spherical boundary around the source with a radius twice the distance between the source and Earth was used. Therefore, simulations ended once all remaining particles reached the detector or passed the spherical boundary limits.

The extragalactic environments of the simulations contained the cosmic microwave background and the extragalactic background light model developed by (44). While the spectrum density of the cosmic microwave background is well known and described by Planck's law, several models, several models have been proposed for the extragalactic background light (44–53). The Gilmore 2012 model (44) was chosen here because it is one of the most recent models available in CRPropa 3 and satisfies the latest constraints found. The energy loss processes of electron-positron pair production, photodisintegration and photoproduction of pions from interactions between these highly energetic particles and the aforementioned cosmic radiation fields were included. It is worth mentioning that photonuclear interactions can produce unstable nuclei, which led to the inclusion of nuclear decay processes. The particles also lose energy due to expansion of the Universe. Therefore, we also considered adiabatic energy losses in the simulations.

Deflections of charged particles in magnetic fields were implemented using the propagation module `PropagationCK` of CRPropa. This module employs the Cash-Karp numerical integration algorithm (54) to solve the equation of motion for charged particles experiencing the Lorentz force. We used a cellular-structure model for extragalactic magnetic fields (55), which is commonly named as stochastic or turbulent magnetic fields in the literature. These fields are randomly oriented inside a cell size equal to a certain coherence length and are generated using turbulence energy spectrum.

The magnetic fields used in the simulations had a root mean square value of 1 nG and a coherence length of approximately 1 Mpc. In fact, the coherence length is given in terms of the power law index (n) and the minimum and maximum wavelength of the turbulence ($l_{\min}$ and $l_{\max}$) (56):

$$\lambda_{\mathrm{coh}} = \frac{1}{2} l_{\max} \frac{n-1}{n} \frac{1-(l_{\min}/l_{\max})^{n}}{1-(l_{\min}/l_{\max})^{n-1}}. \tag{4.1}$$

A Kolmogorov-type distribution (57, 58) was employed for extragalactic magnetic fields of the simulations, which is encoded by a power law index of $n = -5/3$. This choice was made based on the understanding that cosmic magnetic fields might exhibit a Kolmogorov spectrum . We also utilized $l_{\min}$ equal to twice the cell size, which gives approximately 0.49 Mpc. For a broad-band ($l_{\max} \gg l_{\min}$) Kolmogorov spectrum, $\lambda_{\mathrm{coh}} \simeq l_{\max}/5$. Therefore, we chose $l_{\max}$ to be 5 Mpc, so that the coherence length would be approximately 1 Mpc, as previously mentioned.

CRPropa also requires a random seed to generate the stochastic magnetic field. We verified that for each specific seed the distribution of arrival directions of the ultra-high

energy cosmic rays privileges a region around the projection of an astrophysical source in the sky, as can be seen in Figure 19. For this reason, we sampled the magnetic field 20 times with distinct seeds so that all regions around the projection of a source may be equally preferred after particle propagation. Therefore, the total number of injected particles was $5 \times 20 \times 10^7 = 10^9$ for each nearby galaxy as acceleration site. The multiplication by 5 is due to the five primaries injected into the sources. The number of events that reach the detector is shown in Table 2. It is relevant to mention that the order of magnitude of detected events increases for heavier nuclei due to the fragmentation of nuclei resulting from interactions of ultra-high energy cosmic rays and background photons.

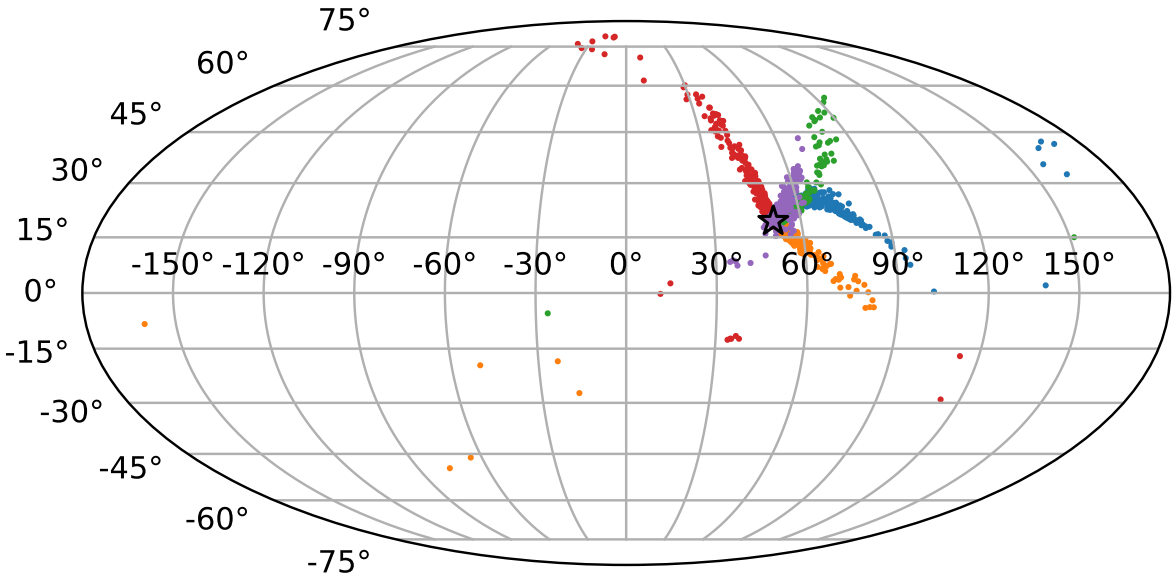

Figure 19 – Galactic coordinates from events originating from different seeds of magnetic fields, with each one represented by a distinct color.

Source: By the author.

Active galactic nuclei and starburst galaxies clearly belong to very distinct classes of galaxies. We made some assumptions about the emission of particles at sources, since there is not enough information about how galaxies emit ultra-high energy cosmic rays. The three models considered in this work were an equal emission of primaries regardless of the astrophysical source ($L_{1:1}$), an emission proportional to the radio luminosity of each galaxy (L_{radio}) and an emission proportional to the gamma ray luminosity of each galaxy (L_γ). We used the same values of luminosity employed in (41), which are displayed in Table 3. In essence, the radio luminosity data at 1.4 GHz was taken from (43) and the gamma ray luminosity between 0.1 and 100 GeV from the *Fermi*-LAT data (59, 60). Since highly energetic particles are responsible for non-thermal emission in astrophysical objects, modeling the emission proportional to the luminosity in these frequency bands is

Table 2 – Number of detected events in the simulations for each primary and local source.

	Hydrogen	Helium	Nitrogen	Silicon	Iron
Centaurus A	38,916	98,330	272,081	465,554	758,906
Fornax A	1,441	4,870	16,847	30,435	46,904
Virgo A	1,661	5,237	17,712	30,528	57,361
NGC 253	69,313	146,478	417,117	702,645	1,137,415
M82	37,665	94,029	276,432	443,488	773,521
NGC 4945	32,356	81,542	231,804	385,834	625,164
M83	30,594	81,195	236,856	395,693	659,737
IC 342	31,417	81,787	243,658	432,556	733,111
NGC 6946	15,086	42,673	128,501	216,736	352,205
NGC 2903	13,435	35,725	105,429	180,279	298,855
NGC 5055	8,578	25,949	77,729	134,495	212,395
NGC 3628	8,488	25,218	81,883	135,339	220,604
NGC 3627	8,359	25,764	80,462	137,127	220,928
NGC 4631	7,691	23,039	72,140	120,643	196,295
M51	5,101	16,245	52,838	86,171	145,633
NGC 891	4,200	12,853	41,747	70,430	109,283
NGC 3556	4,798	15,316	50,006	87,670	146,255
NGC 660	3,140	9,881	32,182	54,082	96,365
NGC 2146	2,137	7,053	24,042	40,717	72,767
NGC 3079	2,020	6,641	21,818	37,601	58,299
NGC 1068	1,816	6,018	21,146	36,271	54,790
NGC 1365	1,240	4,420	14,794	25,685	40,909

Source: By the author.

a reasonable phenomenological hypothesis, besides considering a model of equal emission of particles.

The weights relative to spectral features, simulation binning and luminosity of the sources were applied in the outputs of simulations. For each source s, the number of detected ultra-high energy cosmic rays as a function of the final energy (E), $S(E, s, E_s, Z_s)$, was obtained from simulations and depends on the initial energy of particles (E_s) and their initial electric charge (Z_s). The final flux for each source and each primary with an arbitrary normalization is then given by

Table 3 – Information about the nearby active galactic nuclei and starburst galaxies within a distance of 27 Mpc considered as candidate sites in the simulations.

Galaxy	Type	$L_{\rm radio}$ [10^{38} erg s^{-1}]	L_γ [10^{40} erg s^{-1}]
Centaurus A	AGN	260.0	11.2
Fornax A	AGN	760.0	78.9
Virgo A	AGN	830.0	27.8
NGC 253	SBG	1.0	0.8
M82	SBG	1.3	1.7
NGC 4945	SBG	1.0	1.4
M83	SBG	0.4	1.0
IC 342	SBG	0.5	0.4
NGC 6946	SBG	0.7	0.5
NGC 2903	SBG	0.7	0.9
NGC 5055	SBG	0.6	1.1
NGC 3628	SBG	1.0	1.8
NGC 3627	SBG	0.7	2.0
NGC 4631	SBG	1.1	1.0
M51	SBG	1.2	2.9
NGC 891	SBG	0.9	4.4
NGC 3556	SBG	0.8	2.6
NGC 660	SBG	0.9	5.8
NGC 2146	SBG	4.1	15.4
NGC 3079	SBG	5.0	5.7
NGC 1068	SBG	17.8	17.7
NGC 1365	SBG	3.1	10.7

Source: By the author.

$$\frac{dN}{dE}(E) = \sum_{E_s,s,Z_s} S(E,s,E_s,Z_s) W_{\rm spec}(E_s,Z_s) W_{\rm sim}(E_s) W_{\rm lum}(s), \tag{4.2}$$

where $W_{\rm spec}(E_s,Z_s)$, $W_{\rm sim}(E_s)$ and $W_{\rm lum}(s)$ are the weights accounting for spectral features, simulation binning and luminosity of sources. These weights are given by

$$W_{\rm spec}(E_s,Z_s) = f(Z_s) E_s^{-\Gamma} e^{-E_s/(Z_s R_{\rm max})}, \tag{4.3}$$

$$W_{\rm sim}(E_s) = E_s, \tag{4.4}$$

and

$$W_{\rm lum}(s) = \begin{cases} L_{1:1}(s), \\ L_{\rm radio}(s), \\ L_{\gamma}(s), \end{cases} \tag{4.5}$$

In Equation (4.3), Γ, $R_{\rm max}$ and $f(Z_s)$ are the spectral index, the maximum rigidity and the fraction of each injected nucleus leaving sources. Table 4 displays each value of spectral parameter employed in this work. These specific values were selected based on the best fit results from the combined fit of the Pierre Auger Observatory (61). As the name implies, a combined fit of a simple astrophysical model for ultra-high-energy cosmic ray sources to both the energy spectrum and the mass composition data was carried out in the aforementioned work.

Table 4 – Spectral parameters of the combined fit from the Pierre Auger Collaboration used in this work.

Parameter	Best fit value
Γ	1.22
$\log_{10}(R_{\rm max}/{\rm V})$	18.72
$f({\rm H})$	6.4×10^{-2}
$f({\rm He})$	46.7×10^{-2}
$f({\rm N})$	37.5×10^{-2}
$f({\rm Si})$	9.4×10^{-2}

Source: By the author.

It is true that the ideal way to compare our results with the measurements from the Pierre Auger Observatory is to calculate the amplitude of the dipole considering a partial view of the sky, since the Pierre Auger Observatory is located in the Southern Hemisphere and cannot observe the entire sky. The issue is that it is not possible to calculate the amplitude of the dipole generated by background sources for a partial view with the chosen methodology (Section 4.2). Therefore, we applied the methodology developed in (62) for a full sky coverage to obtain the normalized amplitude of the dipole generated by local sources. No Galactic magnetic field was considered here.

4.2 Simulations of particles from background sources

We implemented the semi-analytical method developed by (34) and (35) to obtain the amplitude of the dipole generated by a random distribution of background sources emitting ultra-high energy cosmic rays. The farther the sources are from Earth, the more magnetic fields deflect the particles coming from them. Since magnetic fields are responsible for isotropizing the distribution of arrival direction of particles, we considered background sources beyond 27 Mpc as being randomly distributed at first.

In general, we can describe the semi-analytical method as a procedure that combines outputs of one-dimensional simulations of particles propagating though background radiation fields with specific weights that provide information about the effects of extragalactic magnetic fields. The one-dimensional simulations are responsible for taking into account energy losses of particles. The semi-analytical method is quite interesting, because it simplifies the numerical simulations required to obtain the flux of particles arriving at Earth. Instead of performing four-dimensional simulations with three spatial dimensions and one time dimension, we only perform one-dimensional simulations with no magnetic fields, which have a lower computational cost.

There are two points to highlight regarding computational expenses. The first one is that particles coming from more distant sources propagate extensively in extragalactic magnetic fields, which can make four-dimensional simulations very time consuming depending on the distance. The second point is that the flux of particles decreases with the square of the distance from the origin so that more particles are needed in four-dimensional simulations for more distant sources to have a good statistic afterwards. For these reasons, it is quite convenient to use the semi-analytical method for background sources. It overcomes time and statistical limitations in completed four-dimensional simulations and has been shown to be very accurate for randomly distributed sources at large distances from Earth.

The semi-analytical method considers turbulent extragalactic magnetic fields, since a simple representation of magnetic fields provides an analytical expression for the scattering length of particles and, consequently, a way to map one-dimensional simulations into four-dimensional results. There are three identifiable regimes for describing the propagation of particles in turbulent magnetic fields, given a specific propagation time (t_s) and scattering length ($\lambda_{\rm scatt}$). These are the ballistic, transition, and diffusive regimes, and each is characterized by a radial distribution of particles relative to the source, $d^2N/drdct$. Let's then define the parameter $\alpha = 3ct/\lambda_{\rm scatt}$. For short propagation times, $\alpha < 0.1$, particle deflections due to magnetic fields are insignificant, and propagation is approximately ballistic. Therefore, a delta distribution describes the ballistic regime,

$$\left(\frac{d^2N}{drdct}\right)_{\text{ballistic}} = \delta(r - ct), \tag{4.6}$$

where r is the distance between particle position and the source. On the other hand, when we dealing with long propagation times, $\alpha > 10$, the behavior of particle propagation aligns more closely with that of a diffusive process. To prevent superluminal propagation, where the particle travels faster than the speed of light ($r > ct$), we use the truncated Gaussian distribution, which is given by

$$\left(\frac{d^2N}{drdct}\right)_{\text{diff}} = \begin{cases} Ar^2 e^{-\frac{r^2}{2\sigma^2}} & \text{for } r \leq ct, \\ 0 & \text{for } r > ct. \end{cases} \tag{4.7}$$

In particular, $\sigma = \sqrt{\lambda_{\text{scatt}} ct/3}$, and A is the normalization constant,

$$\frac{1}{A} = \sigma^2 \left[\sqrt{\frac{\pi}{2}}\sigma \text{erf}\left(\frac{ct}{2\sigma}\right) - cte^{-\frac{(ct)^2}{2\sigma^2}}\right]. \tag{4.8}$$

This distribution effectively characterizes the diffusive regime and is easy to treat both numerically and analytically. However, its limit in the ballistic regime ($\sigma \to \infty$),

$$\lim_{\sigma\to\infty}\left(\frac{dN}{drdct}\right)_{\text{diff}} = \begin{cases} \frac{3r^2}{(ct)^3} & \text{for } r \leq ct, \\ 0 & \text{for } r > ct, \end{cases} \tag{4.9}$$

is not a delta distribution, as desired to characterize particle propagation. Therefore, the truncated Gaussian distribution cannot properly describe the transition between the ballistic and the diffusive regime. For this transition regime ($0.1 < \alpha < 10$), the Jüttner distribution (63, 64), a more complex function, is used,

$$\left(\frac{d^2N}{drdct}\right)_{\text{Jüttner}} = \begin{cases} \frac{r^\alpha e^{-\alpha/\sqrt{1-\left(\frac{r}{ct}\right)^2}}}{(ct)^3 K_1(\alpha)\left[1-\left(\frac{r}{ct}\right)^2\right]^2} & \text{for } r \leq ct, \\ 0 & \text{for } r > ct, \end{cases} \tag{4.10}$$

where $K_1(\alpha)$ is the modified Bessel function of the second kind of integer order 1. The limits of this distribution for small and large α agree with the ballistic and diffusive regime respectively. Nevertheless, the Jüttner distribution is much more complex to handle both numerically and analytically. Figure 20 shows the time evolution of the cosmic ray spatial distribution, while Figure 21 shows its integral over time. Each of the regimes is highlighted by a different color.

The magnetic field weight is then given by

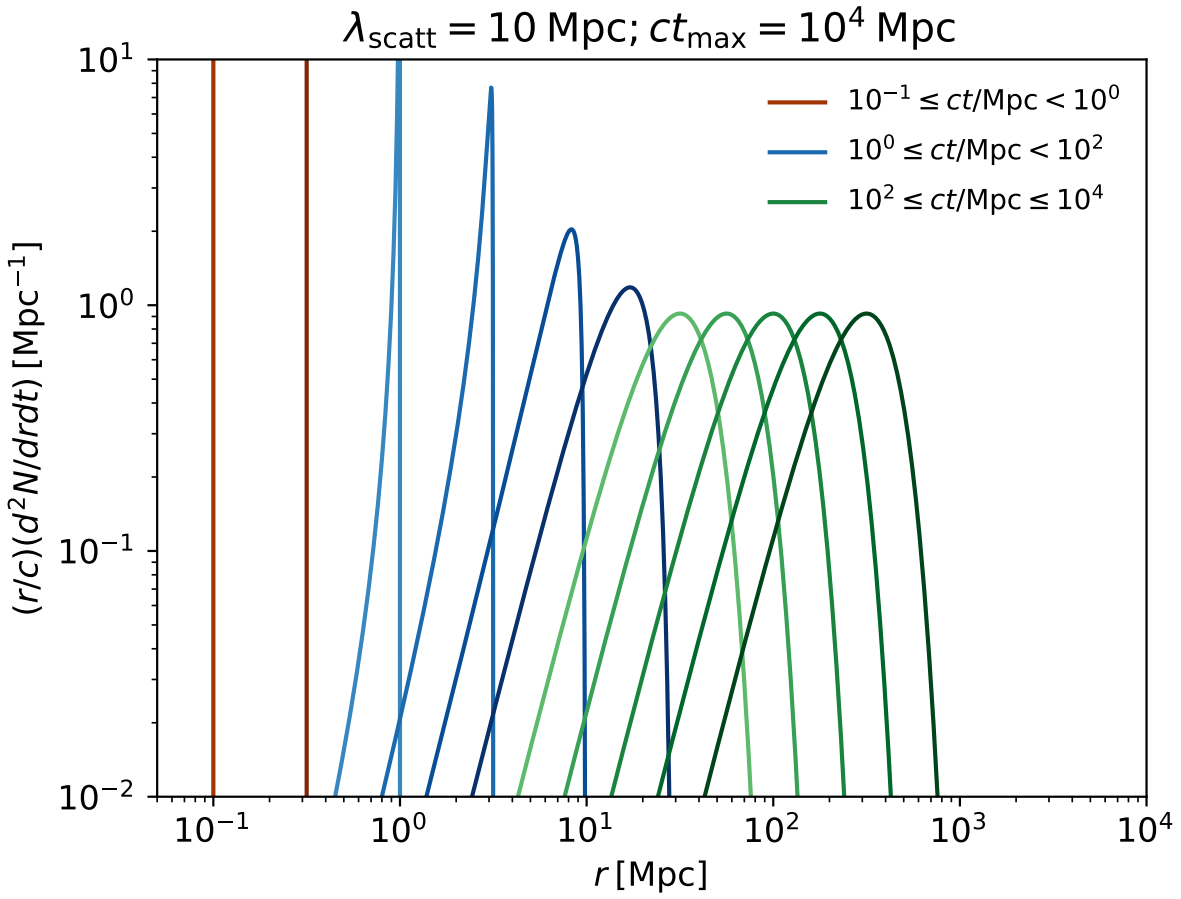

Figure 20 – Radial distributions of particles for distinct propagation times.

Source: By the author.

$$W_{\rm mag} \propto \int_{D_{\rm min}}^{D_{\rm max}} \frac{dN}{drdct}(\lambda_{\rm scatt}, t_s)dr. \tag{4.11}$$

This integration is carried out from a minimum to a maximum distance of a spherical shell of sources. In particular, the magnetic weight provides the fraction of ultra-high energy cosmic rays released at a time t_s ago from sources that are located between $D_{\rm min}$ and $D_{\rm max}$ from Earth. Despite considerably distinct approaches to magnetic fields, the same model of cellular structure was considered in the semi-analytical method with a root mean square value of 1 nG and a coherence length of approximately 1 Mpc, just as in the four-dimensional simulations. These configurations were encoded in the particle scattering length, which takes the form of

$$\lambda_{\rm scatt} = \begin{cases} \left(\frac{R_L}{\lambda_{\rm coh}}\right)^{1/3} \lambda_{\rm coh} & \text{for } R_L < \lambda_{\rm coh}, \\ \left(\frac{R_L}{\lambda_{\rm coh}}\right)^{2} \lambda_{\rm coh} & \text{for } R_L \geq \lambda_{\rm coh}, \end{cases} \tag{4.12}$$

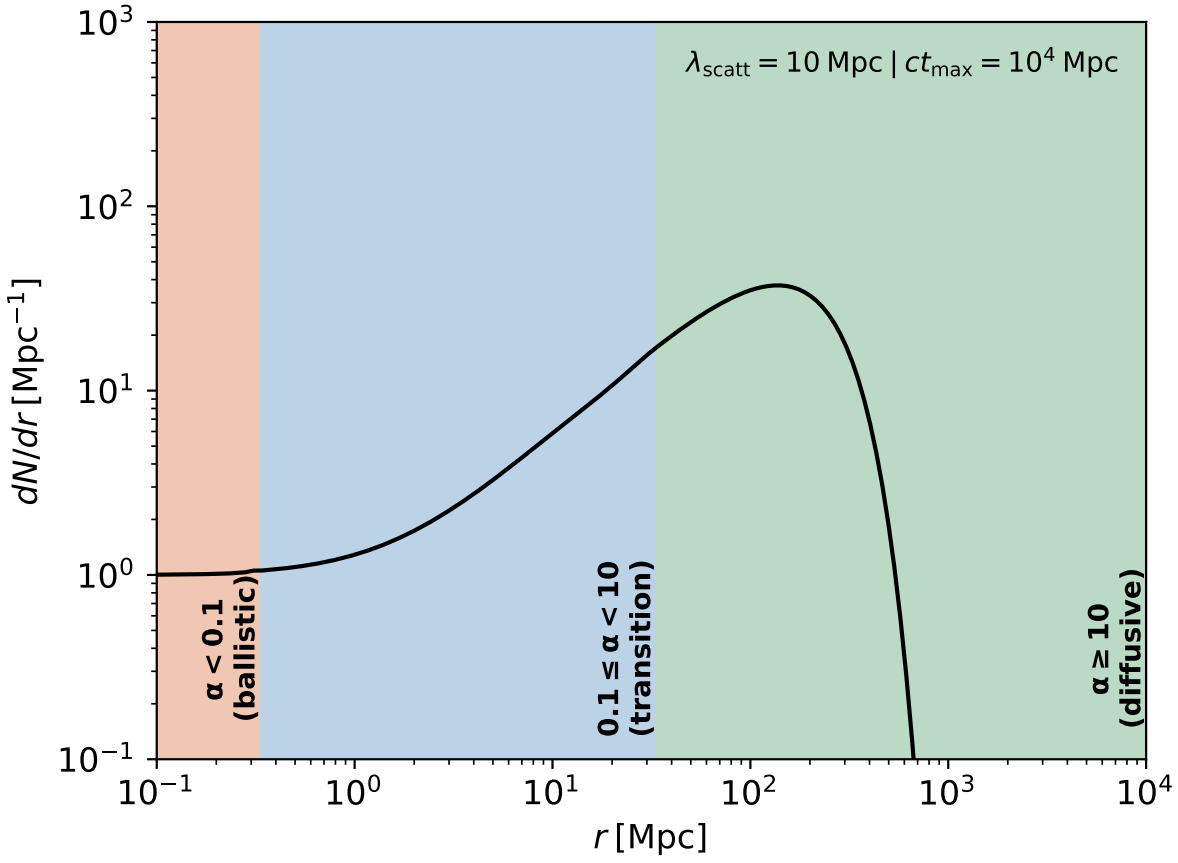

Figure 21 – Integration of the radial distributions.

Source: By the author.

where $\lambda_{\rm coh}$ is the coherence length of the magnetic field and R_L is the Larmor radius of particles,

$$R_L = \frac{p}{|q|B} \approx \frac{1.081}{Z}\left(\frac{E}{\rm EeV}\right)\left(\frac{\rm nG}{B}\right) \text{ Mpc}. \tag{4.13}$$

The magnetic field weight presented in Equation (4.11) was also inserted in Equation (4.2) in order to obtain the flux of particles coming from background sources. The propagation time of particles in Equation (4.11) was sampled from 1 to 3162.2 Mpc (in units of distance ct_s) with 20 bins per decade on a logarithmic scale of base 10. The same binning was used to discretize the energy of particles emitted by sources from 1 to 10^4 EeV. Since we sampled propagation times using a logarithmic scale, we also had to take into account another weight relative to simulation. Therefore, instead of using Equation (4.4) for the weight relative to simulations, we now have

$$W_{\rm sim}(E_s, t_s) \propto E_s t_s. \tag{4.14}$$

The nuclei injected into the sources were the same as those used in the four-dimensional simulations. In each simulation, 10^3 particles were propagated. Simulations were performed with 10^3 particles for each combination of energy, propagation time and primary nucleus. We employed the same energy loss processes described in the Section 4.1. The emission of particles from background sources was modeled according to the specific set of local sources under consideration. For emission proportional to the luminosity in radio and gamma rays from galaxies, the luminosity of background sources was calculated as the average of the individual luminosities within the selected set of local sources. No redshift dependence was considered here for the luminosity of background sources. For equal particle emission, no luminosity was provided for background sources.

The fluxes of particles reaching Earth are proportional to each other for simulations of only local sources, just as for simulations of only background sources. The issue is how to combine the results from both types of simulations. We normalized the fluxes of particles from background sources with respect to the fluxes from local sources using the energy spectrum of Fornax A for protons as primaries as a reference. In particular, we equaled the energy spectra at the energy of 10 EeV. Since Fornax A is located at a distance of 20.90 Mpc from Earth, we also obtained the energy spectrum from a distance shell between 19 and 23 Mpc using the semi-analytical method for normalization. Distance shells with distinct sizes clearly do not provide the same flux. Therefore, the normalization factor that multiplies the flux of background sources had to take into account the number of sources in that certain distance shell. This factor is then given by

$$\eta(\rho) = \frac{n_{ls}(E = 10\,\mathrm{EeV})}{n_{bs}(E = 10\,\mathrm{EeV})} V\rho. \tag{4.15}$$

The volume V values approximately 22,234 Mpc^3 for the distance shell from normalization. The density of background sources ρ is a free parameter. We considered a discrete distribution of sources starting from 27 Mpc described by the size of the each distance shell D_{shell}, in such a way that the number of sources within a shell beginning at distance $iD_{\mathrm{shell}} + 27$ Mpc is i^2. Therefore, the density of each distance shell is given by

$$\rho = \frac{3i^2}{4\pi(3i^2 + 3i + 1)D_{\mathrm{shell}}^3}. \tag{4.16}$$

In the limit where the number of sources goes to infinity, we have that

$$\rho = \frac{1}{4\pi D_{\mathrm{shell}}^3}, \tag{4.17}$$

which only depends on the size of the distance window. For each set of local sources and luminosity of sources, we changed the density of background sources eight times by changing the size of distance shells. Table 5 shows the values used in this work.

Table 5 – Values of the size of spherical layers of sources and the corresponding density of background sources.

D_{shell} [Mpc]	ρ [10^{-4} Mpc^{-3}]
2	99.47
3	29.47
4	12.43
5	6.37
6	3.68
7	2.32
8	1.55
9	1.09

Source: By the author.

To obtain the amplitude of the dipole as a function of energy for background sources, we adapted the mathematical expression presented in (35) for the coefficients of the angular distribution from an ensemble of sources. Instead of performing a summation over the sources, we modified it to perform a summation over the distance shells themselves. Therefore,

$$\Phi_0^{(\text{tot})}(E) = \sum_i n_i(E, iD_{\text{shell}}) \tag{4.18}$$

and

$$\Phi_{l>0}^{(\text{tot})}(E) = \sqrt{\sum_i \left[\frac{\Phi_l(E, iD_{\text{shell}}) n_i(E, iD_{\text{shell}})}{i}\right]^2}, \tag{4.19}$$

where n_i is the particle flux for the distance window of sources i and l is the order of the pole. To conclude, the normalized amplitude of the dipole for background sources is given by

$$\delta(E) = \frac{\Phi_1^{(\text{tot})}(E)}{\Phi_0^{(\text{tot})}(E)}. \tag{4.20}$$

4.3 Combining results from local and background sources

As shown in Sections 4.1 and 4.2, we know how to calculate the amplitudes of dipoles for local sources and for background sources. To derive the formula for the total amplitude of the dipole generated by both categories of sources, we considered two dis-

tributions of arrival directions represented as a combination of a monopole term and a dipole term. These functions depend on two distinct angles, θ and φ, and are described as

$$f_1(\theta_1, \varphi_1) = A_1(1 + \delta_1 \cos\theta_1) \tag{4.21}$$

and

$$f_2(\theta_2, \varphi_2) = A_2(1 + \delta_2 \cos\theta_2), \tag{4.22}$$

where A is the flux of particles and δ is the normalized amplitude of the dipole. The subscript 1 is used for local sources, while the subscript 2 for background sources. When we write the angle θ_2 in Equation in terms of the angle θ_1,

$$\theta_2 = \theta_1 + \alpha, \tag{4.23}$$

we have that

$$f_2(\theta_1, \varphi_2) = A_2[1 + \delta_2 \cos(\theta_1 + \alpha)] = A_2[1 + \delta_2(\cos\theta_1 \cos\alpha - \sin\theta_1 \sin\alpha)]. \tag{4.24}$$

Since both distributions of arrival directions are now expressed in terms of the angle θ_1, a direct summation of Equations (4.21) and (4.24) can be done to yield the combined distribution of arrival directions for both local sources and background sources. This summation results in

$$f(\theta_1, \varphi_1) = (A_1 + A_2) + \cos\theta_1[A_1\delta_1 + A_2\delta_2 \cos\alpha] + \sin\theta_1[-A_2 \sin\alpha]. \tag{4.25}$$

We do not have information about the arrival directions of particles by using the semi-analytical method, which would be encoded by the angle α. Nevertheless, background sources can either amplify or dilute the amplitude of the dipole from local sources, which has a strong signal. The two extreme cases are when the directions of the dipole of both categories of sources point exactly in the same direction ($\alpha = 0$) and when point in opposite directions ($\alpha = \pi$). The total amplitude encompassed by these two extremes is given by

$$\delta = \frac{A_1\delta_1 \pm A_2\delta_2}{A_1 + A_2}. \tag{4.26}$$

It is worth mentioning that we did not need to include additional terms in the distribution in Equations (4.21) and (4.22), since higher pole terms would not contribute to the amplitude of the dipole.

4.4 Statistical analysis

For each model of local sources and luminosity, we compared our results of the amplitude of the dipole as a function of energy with measurements of the Pierre Auger Observatory (Figure 9). This comparison involved altering the density of background sources. In particular, we used the value of the amplitude of the dipole in which the second term in Equation (4.26) is zero. For gaussian or almost gaussian uncertainties, it is possible to use the chi-square statistical test given by

$$\chi^2 = \sum_{i=1}^{n} \frac{[y_i - f(x_i)]^2}{\sigma_i^2}, \tag{4.27}$$

where y_i represents the measured data from the Pierre Auger Observatory, $f(x_i)$ is the proposed fit function and σ_i^2 denotes the variance for each data point. The upper limit measurements in Figure 9 were not used in the statistical test, because these points are consistent with the null hypothesis that there is not a dipole there. Based on these analyses, we constrained the range of density of background sources for each model within a 3σ confidence level.

5 THE AMPLITUDE OF THE DIPOLE

We constructed 72 distinct phenomenological models of sources of ultra-high energy cosmic rays, in which their distinct parameters are shown in Figure 22. There are three sets of nearby galaxies (AGN, AGN + SBG, and SBG) and three variations of luminosity ($L_{1:1}$, L_{radio}, and L_{γ}). For each phenomenological model, we varied the density of background sources eight times according to the values presented in Table 5. Each distinct combination of the three parameters provides a different model. Figures 23 to 28 present the results obtained for the amplitude of the dipole as a function of the energy using Equation (4.26) across the entire parameter space. As we do not have the direction of the dipole from the background sources, there is a range of possible values for the amplitude of the dipole, encoded in the plus-minus sign in the second term of the numerator of Equation (4.26). Therefore, the shaded areas in Figures 23 to 28 illustrate all possible values for the amplitude of the dipole, ranging from the lowest to the highest value. Moreover, the colored lines in Figures 23 to 28 illustrate when the second term of the amplitude of the dipole in Equation (4.26) is zero. In particular, we used the pink color for AGN, the purple color for AGN + SBG, and the blue color for SBG. Lastly, the black data points with uncertainties represent the measurements obtained by the Pierre Auger Observatory (1).

The amplitude of the dipole increases with energy regardless of the model, since more energetic particles are less deflected by magnetic fields, which is an agent responsible for isotropizing the distribution of arrival directions of particles in the simulations. For instance, if we decompose an isotropic distribution into spherical harmonics, the only non-zero term in the multipole expansion is the monopole term. This means that the anisotropy of a distribution is encoded in higher order poles. Therefore, the higher the anisotropy, the higher the terms from other poles will be.

5.1 The amplitude of the dipole for distinct sets of local sources and luminosities

In general, the amplitude of the dipole for the combination of active galactic nuclei and starburst galaxies is higher than for each category separately, considering their emission proportionately to the radio or gamma-ray luminosity. This might appear counterintuitive in principle, since a smaller number of sources would result in a greater degree of anisotropy in the distribution of arrival directions. However, the point is that we are not considering the amplitude of the dipole produced only by local sources, but the amplitude of the dipole produced by local sources and background sources together. Equation (4.26) shows that there is a further contribution of background sources in the denominator with the particle flux from background sources, A_2, which assumes higher values for the

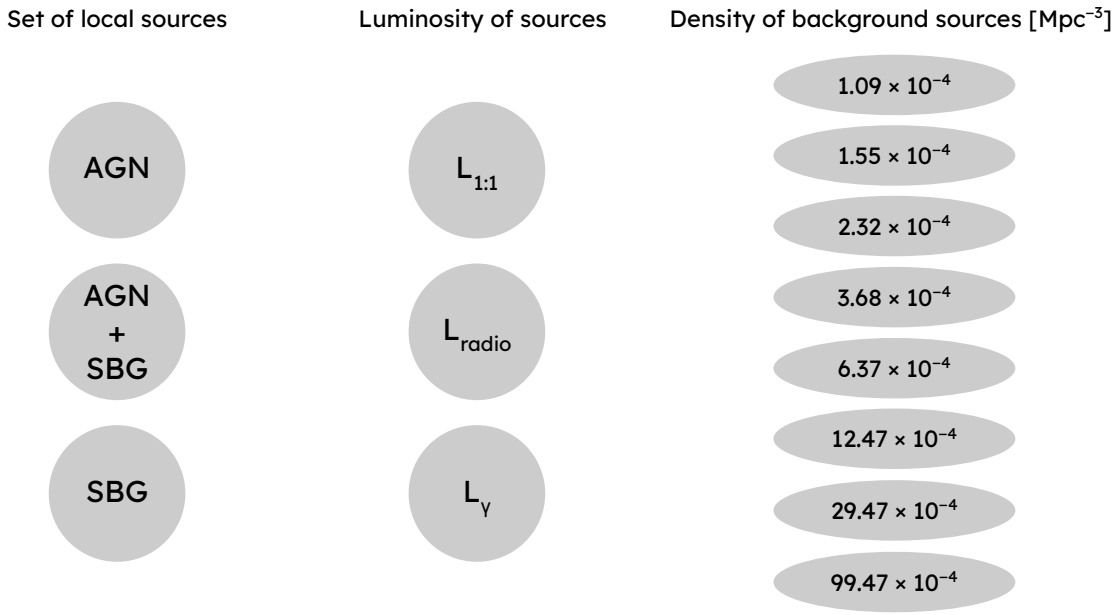

Figure 22 – Parameter space of the 72 phenomenological models of sources considered in this work.

Source: Source: By the author.

emission proportional to the radio and gamma-ray luminosity of galaxies.

The range of possible values for the amplitude of the dipole is commonly higher for active galactic nuclei or in some cases for the combination of both classes of nearby galaxies. This feature probably occurs due to the higher value of A_2 for active galactic nuclei that emit proportional to radio or gamma-ray luminosity of each galaxy. The shaded area also becomes more visible as the density of background sources increases, since A_2 is proportional to the density of background sources in the normalization term given by Equation (4.15). While the amplitude of the dipole δ_2 is normalized and does not depend on the set of local sources, A_2 changes as we change the parameter space.

The behaviour of the curves for each set of local sources is more or less the same so that distinct densities can better fit the data of the Pierre Auger Observatory by increasing or decreasing the value of the amplitude of the dipole. For this reason, only analyzing the amplitude of the dipole was not enough to distinguish which class of galaxies can be sources of ultra-high energy cosmic rays. To distinguish which type of galaxy accelerates particles to the highest energies, it would probably require investigating other measurements, such as the direction of the dipole.

Finally, we can clearly see in Table 3 that the radio and gamma-ray luminosity

from active galactic nuclei are much higher than those from starburst galaxies. Therefore, there is a higher particle emission coming from active galactic nuclei compared to starburst galaxies for the set of AGN + SBG in the case of emission proportional to the radio and gamma-ray luminosity of each galaxy. On the other hand, the amplitude of the dipole for a one-to-one luminosity and the same set of local sources (AGN + SBG) is dominated by starburst galaxies, since the number of starburst galaxies is much greater than that of active galactic nuclei within 27 Mpc. The behaviour of the amplitude of the dipole for AGN + SBG and for SBG in Figures 23 and 24 is then almost the same, which means that both curves are practically overlapped.

5.2 The amplitude of the dipole and the density of background sources

The density of background sources is given by Equation (4.17). If we choose a certain phenomenological model and analyze the evolution of the amplitude of the dipole with the density of background sources, we find that the higher the value of density of background sources, the lower the amplitude of the dipole. Naturally, magnetic field effects complicate the interpretation of the results, but in essence the distribution of background sources is directly related to the anisotropy in the distribution of arrival directions. For instance, the anisotropy would be very large in the limit of a unique source of ultra-high energy cosmic rays. Even though our results are completely contemplated in Figures 23 to 28, Figures 32 to 40 in Appendix A depict the amplitude of the dipole in a distinct arrangement, where each graph shows distinct density values for a single catalog of nearby sources.

Table 6 provides the values that minimize the chi-square statistical test in Equation (4.27), $\chi^2_{\rm min}$, and Figures 29 to 31 display how the $\chi^2 - \chi^2_{\rm min}$ value behaves with the density of background sources. In particular, we compiled in Table 7 the density values of background sources that minimize the chi-square statistical test performed. It was possible to constrain the range of density of background sources within a confidence level of 3σ for each constructed model, which is also shown in Table 7. Therefore, the range of density of background sources obtained in this work considering all the distinct models was 2.20×10^{-4} to $57.44 \times 10^{-4}\,{\rm Mpc}^{-3}$. This density range not only is within the values obtained in previous analyzes by the Pierre Auger Collaboration but also constrained even more these previous results. In particular, (65) obtained a lower limit at a 95% confidence level for the density of sources of ultra-high energy cosmic rays of $(0.06 - 5) \times 10^{-4}\,{\rm Mpc}^{-3}$ for a uniform distribution of sources and of $(0.2 - 7) \times 10^{-4}\,{\rm Mpc}^{-3}$ for sources following the distribution of local matter (66). Our results constrained the density of background sources by one order of magnitude, considering the hypotheses raised for astrophysical sources of ultra-high energy cosmic rays and extragalactic environments.

Table 6 – Minimum chi-squared value for each phenomenological model of set of local sources and luminosity.

Model	$\chi^2_{\rm min}$
$L_{1:1}$ | AGN	24.12
$L_{1:1}$ | AGN + SBG	15.55
$L_{1:1}$ | SBG	16.26
$L_{\rm radio}$ | AGN	25.37
$L_{\rm radio}$ | AGN + SBG	23.12
$L_{\rm radio}$ | SBG	15.22
L_{γ} | AGN	23.79
L_{γ} | AGN + SBG	21.45
L_{γ} | SBG	18.22

Source: Source: By the author.

Table 7 – Value of the density of background sources that better describe measurements of the Pierre Auger Observatory, $\rho_{\rm best}$, and the lower and upper limits of the density of background sources within a 3σ of confidence level, $\rho^{3\sigma}_{\rm min}$ and $\rho^{3\sigma}_{\rm max}$, for each phenomenological model of set of local sources and luminosity.

Model	$\rho_{\rm best}$ $[10^{-4}\,{\rm Mpc}^{-3}]$	$\rho^{3\sigma}_{\rm min}$ $[10^{-4}\,{\rm Mpc}^{-3}]$	$\rho^{3\sigma}_{\rm max}$ $[10^{-4}\,{\rm Mpc}^{-3}]$
$L_{1:1}$ | AGN	12.43	9.41	20.18
$L_{1:1}$ | AGN + SBG	6.37	5.36	14.85
$L_{1:1}$ | SBG	6.37	5.79	19.19
$L_{\rm radio}$ | AGN	3.68	3.36	9.29
$L_{\rm radio}$ | AGN + SBG	29.47	27.99	57.44
$L_{\rm radio}$ | SBG	6.37	3.85	10.26
L_{γ} | AGN	3.68	2.20	5.69
L_{γ} | AGN + SBG	12.43	9.72	20.66
L_{γ} | SBG	6.37	3.68	10.26

Source: Source: By the author.

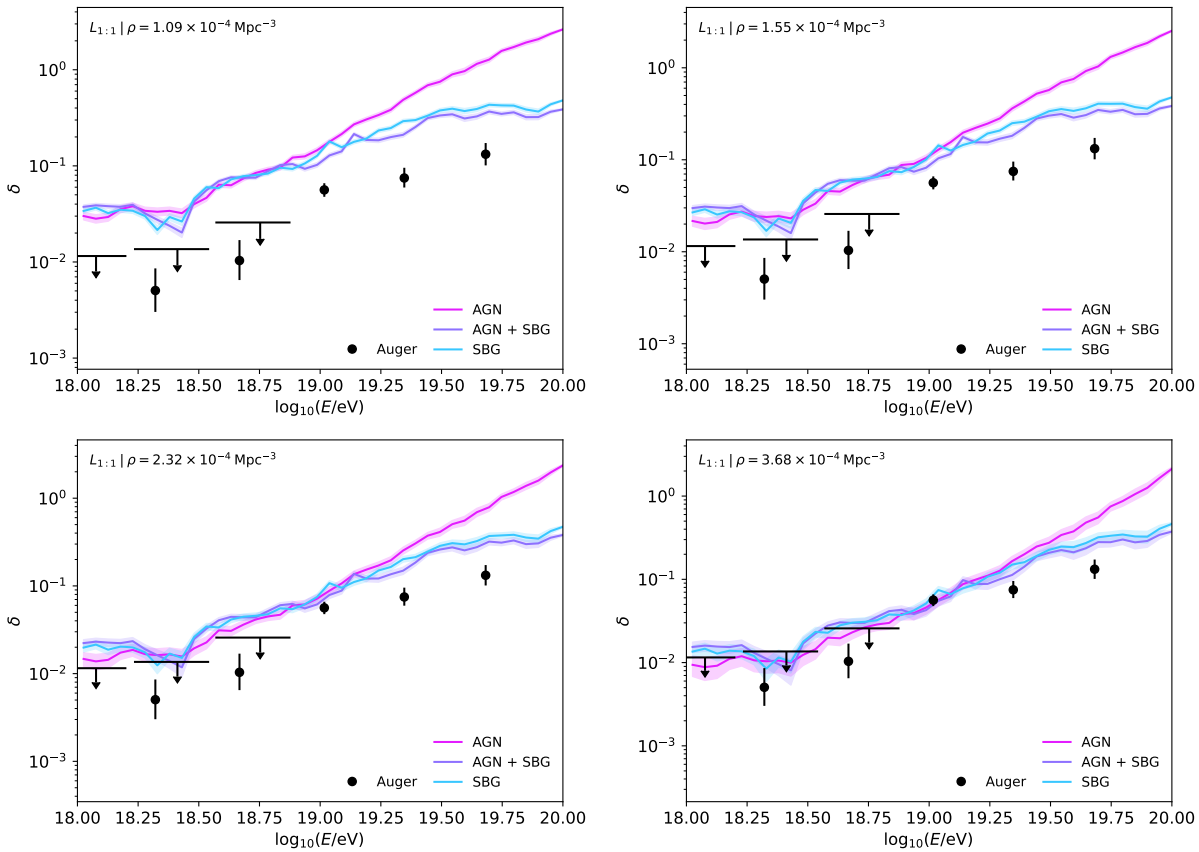

Figure 23 – Amplitude of the dipole as a function of the energy for an equal emission of primaries regardless of the astrophysical source. The distinct classes of nearby galaxies and densities of background sources are shown in the plots. The black points with uncertainties are measurements from the Pierre Auger Observatory. (1)

Source: By the author.

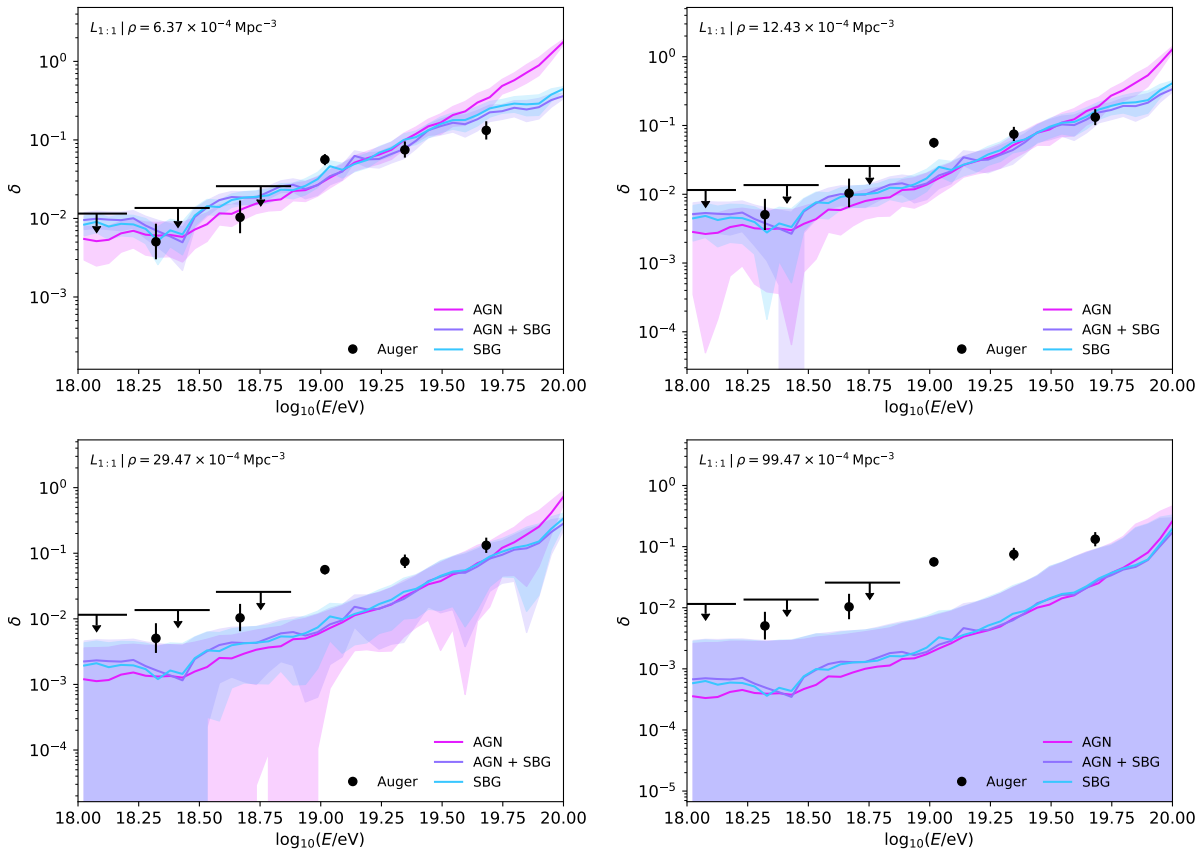

Figure 24 – Amplitude of the dipole as a function of the energy for an equal emission of primaries regardless of the astrophysical source. The distinct classes of nearby galaxies and densities of background sources are shown in the plots. The black points with uncertainties are measurements from the Pierre Auger Observatory. (1)

Source: By the author.

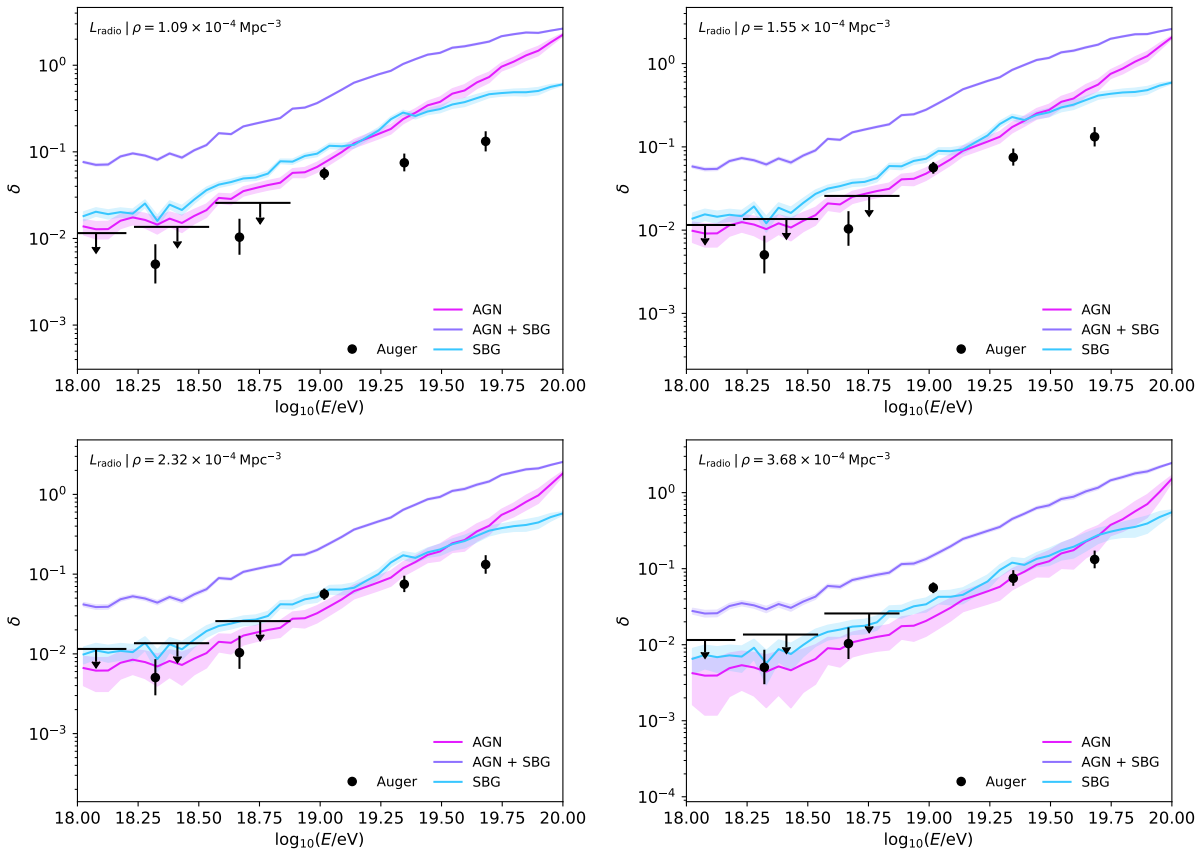

Figure 25 – Amplitude of the dipole as a function of the energy for an emission proportional to the radio luminosity of each galaxy. The distinct classes of nearby galaxies and densities of background sources are shown in the plots. The black points with uncertainties are measurements from the Pierre Auger Observatory. (1)

Source: By the author.

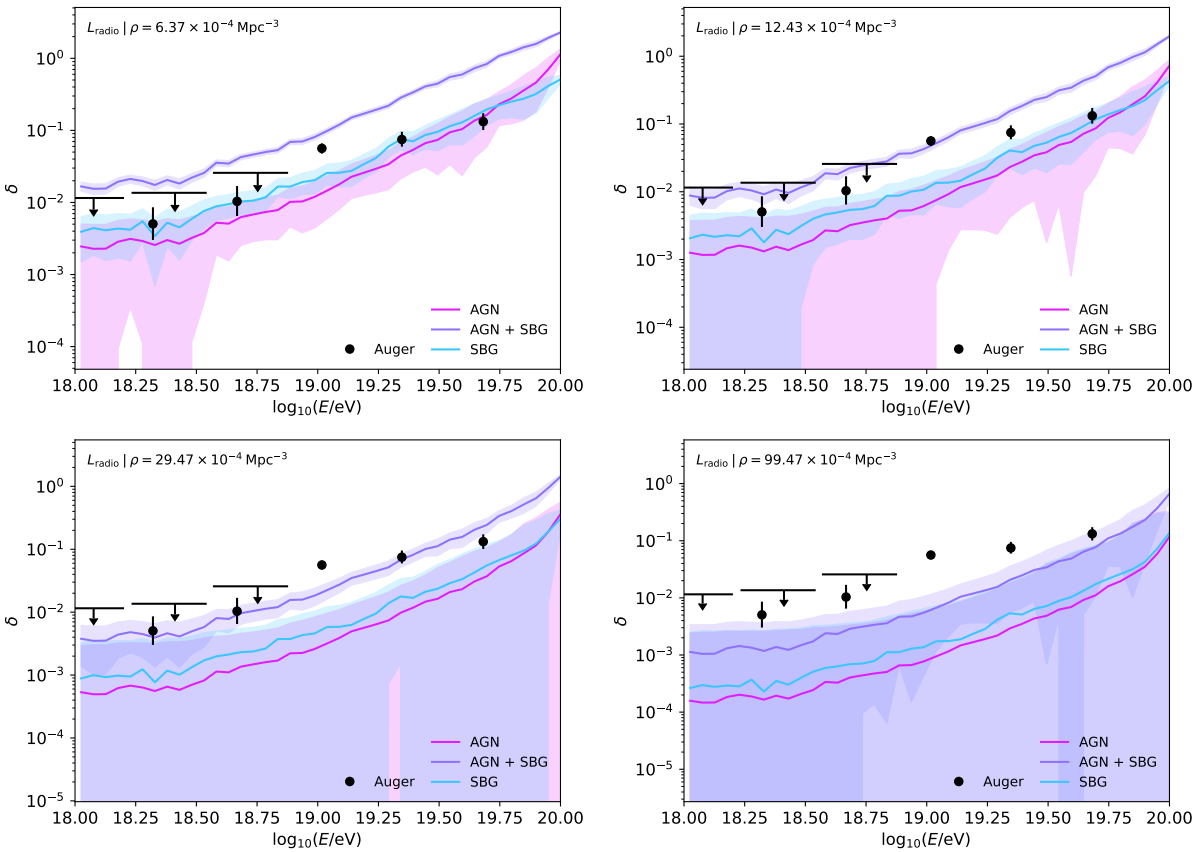

Figure 26 – Amplitude of the dipole as a function of the energy for an emission proportional to the radio luminosity of each galaxy. The distinct classes of nearby galaxies and densities of background sources are shown in the plots. The black points with uncertainties are measurements from the Pierre Auger Observatory. (1)

Source: By the author.

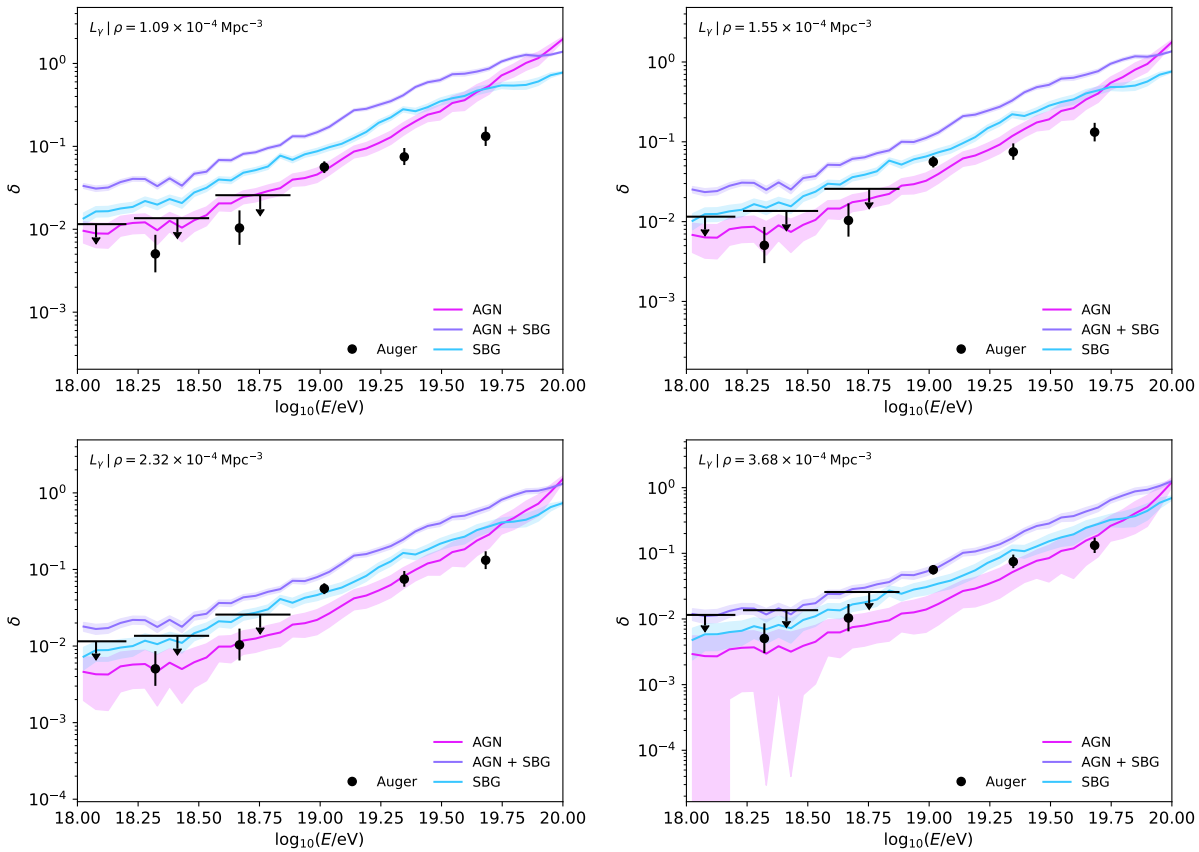

Figure 27 – Amplitude of the dipole as a function of the energy for an emission proportional to the gamma ray luminosity of each galaxy. The distinct classes of nearby galaxies and densities of background sources are shown in the plots. The black points with uncertainties are measurements from the Pierre Auger Observatory. (1)

Source: By the author.

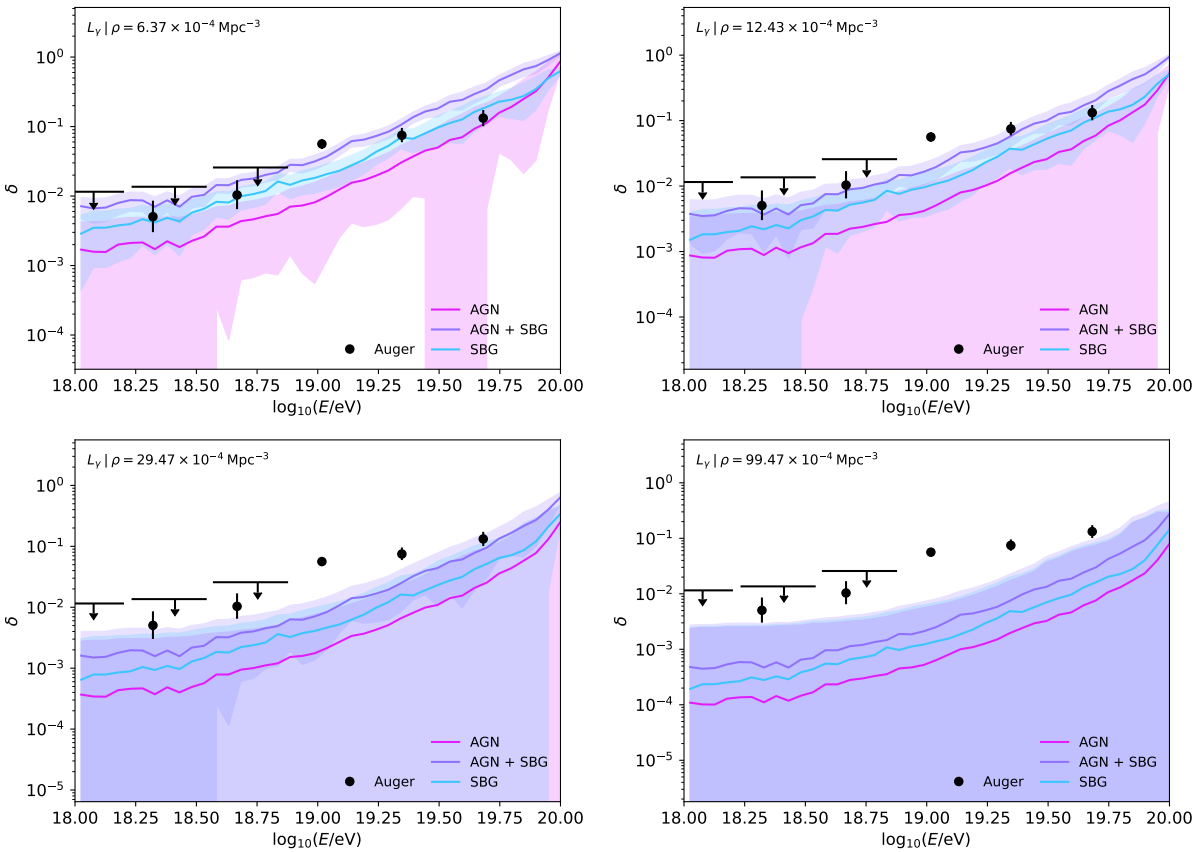

Figure 28 – Amplitude of the dipole as a function of the energy for an emission proportional to the gamma ray luminosity of each galaxy. The distinct classes of nearby galaxies and densities of background sources are shown in the plots. The black points with uncertainties are measurements from the Pierre Auger Observatory. (1)

Source: By the author.

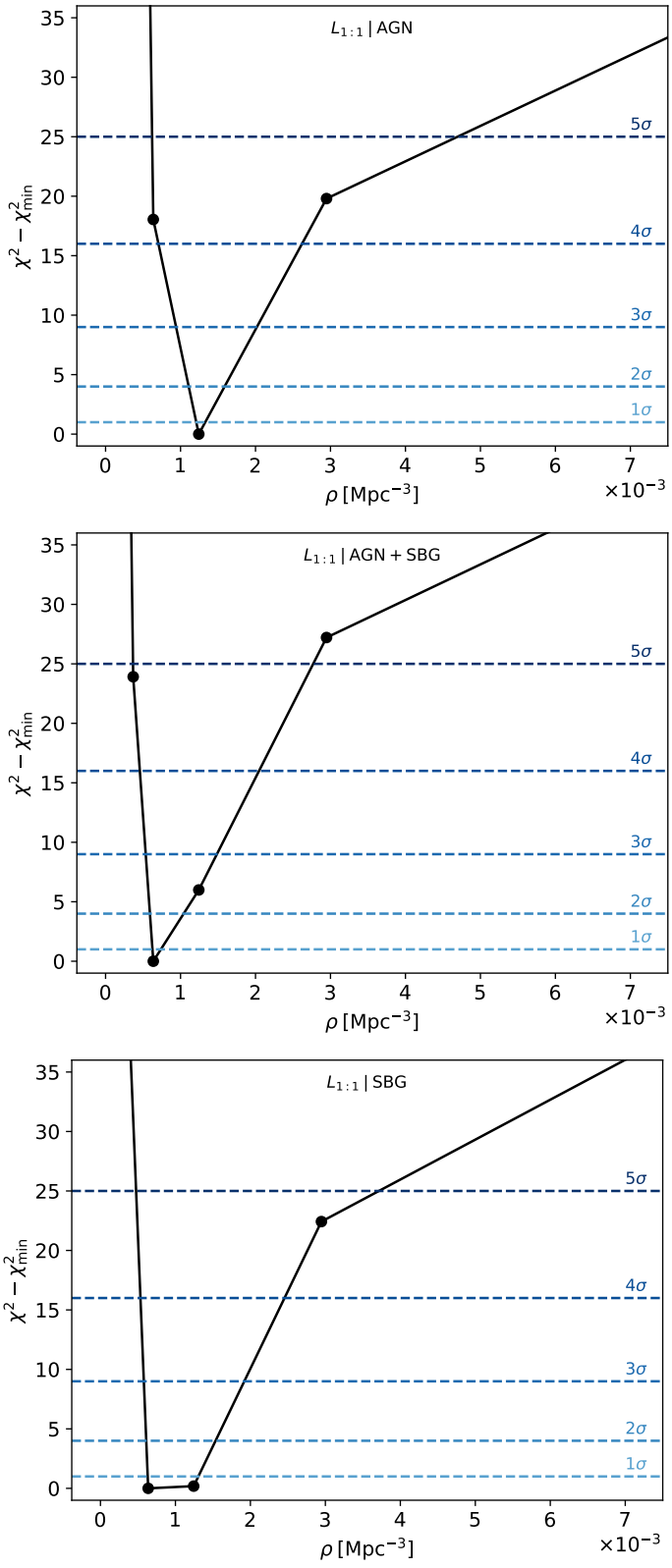

Figure 29 – Difference between chi-squared and minimum chi-squared values as a function of the density of background sources for an equal emission of primaries regardless of the astrophysical source and the three distinct sets of local sources. In the upper part of the plots, each combination of set of local sources and luminosity of sources is indicated. The black lines only connect the black points obtained by the statistical analysis.

Source: By the author.

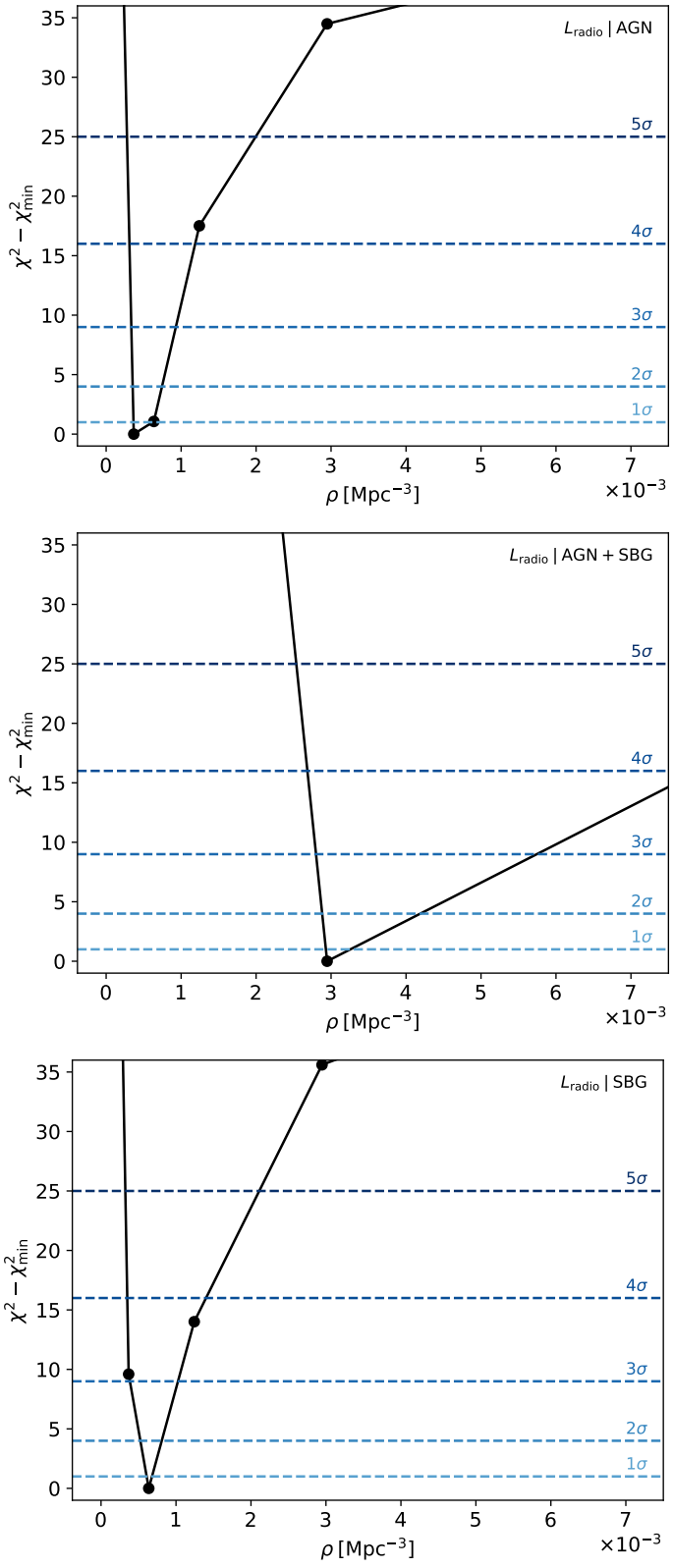

Figure 30 – Difference between chi-squared and minimum chi-squared values as a function of the density of background sources for an emission proportional to the radio luminosity and the three distinct sets of local sources. In the upper part of the plots, each combination of set of local sources and luminosity of sources is indicated. The black lines only connect the black points obtained by the statistical analysis.

Source: By the author.

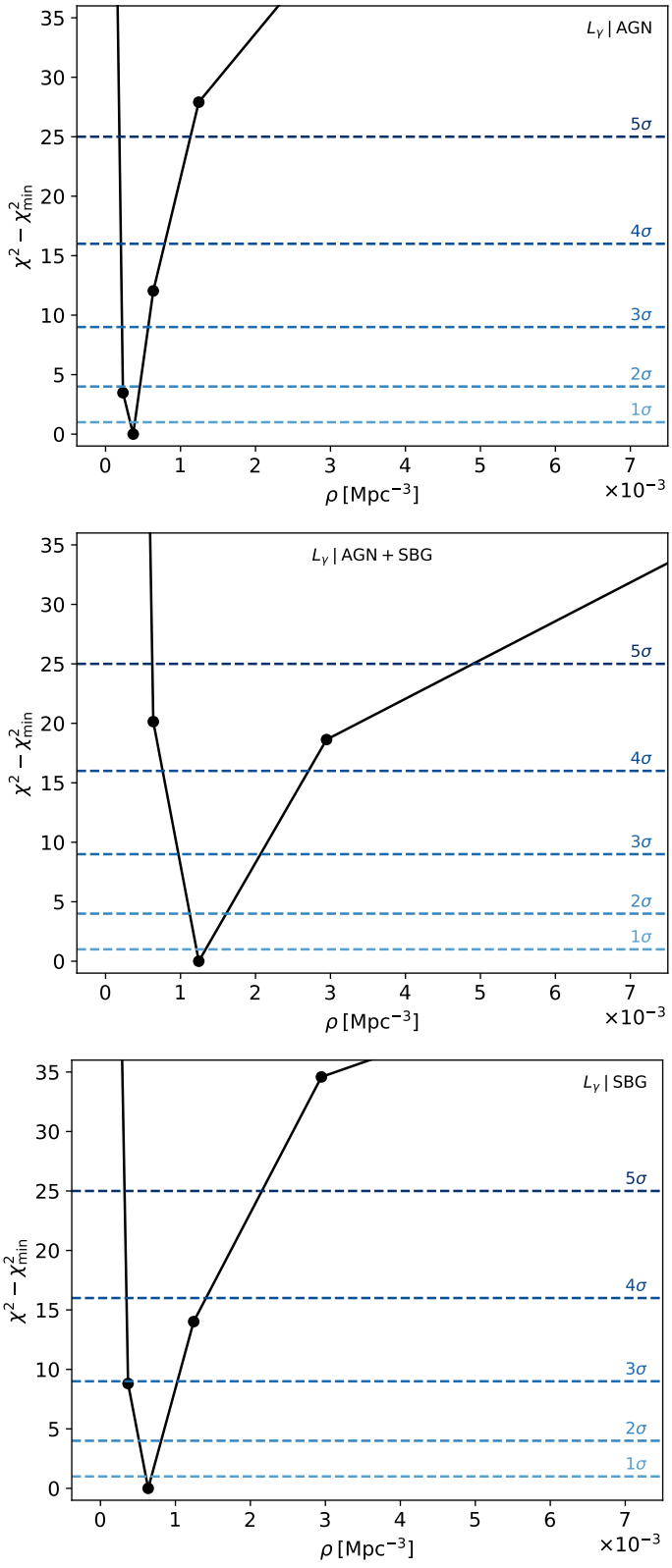

Figure 31 – Difference between chi-squared and minimum chi-squared values as a function of the density of background sources for an emission proportional to the gamma ray luminosity and the three distinct sets of local sources. In the upper part of the plots, each combination of set of local sources and luminosity of sources is indicated. The black lines only connect the black points obtained by the statistical analysis.

Source: By the author.

6 CONCLUSIONS AND PERSPECTIVES

In this work, we analyzed one of the main measurements of anisotropy of ultra-high energy cosmic rays, which was the amplitude of the dipole measured by the Pierre Auger Observatory. We constructed 72 scenarios of local sources and background sources. The models consisted in three sets of local sources, three variations of particle emission and eight density values of background sources. A unique aspect of this work was combining two distinct simulation strategies to deal with different sources depending on their distance. Besides understating the behavior of the amplitude of the dipole for the entire parameter space, we compared our results with previous measurements from the Pierre Auger Observatory through a statistical test. Therefore, we constrained the range of density of background sources, which was one of the main aims of this work.

The importance of local sources of ultra-high energy cosmic rays arises from combining propagation effects with measurements from observatories. Energy loss processes and magnetic field deflections can help constrain the distance to the nearest sources of these particles. Therefore, it is crucial to consider these sources as individual sources in simulations. Among the possible acceleration source candidates, we selected active galactic nuclei and starburst galaxies, as they satisfy the Hillas criterion presented in Section 3.2. However, there remains controversy regarding whether starburst galaxies can accelerate particles due to their galactic power. Nevertheless, starburst galaxies gain credibility as candidate sources based on works from the Pierre Auger Observatory, which correlate ultra-high energy cosmic rays with the measured distribution of arrival directions of particles. However, in active galactic nuclei, particles can be accelerated in relativistic jets at the shock front between the jet and the intergalactic medium.

We simulated particles propagating in the universe originating from local sources (up to 27 Mpc) using the conventional Monte Carlo propagation code CRPropa. For background sources, we employed the semi-analytical method. The extragalactic environments included the cosmic microwave background and extragalactic background light, along with cellular structure magnetic fields with a root mean square of 1 nG. Particles could interact with photons from the background fields through photodisintegration, photopion production, and electron-positron pair production. We injected five representative nuclei into the sources, and the spectral features were determined from the combined fitting work conducted by the Pierre Auger Collaboration. Due to the distinct treatments in each simulation strategy, the methods for calculating the amplitude of the dipole also differed between local sources and background sources.

The amplitude of the dipole obtained from our simulations is presented in Section 5. It is worth mentioning that in this work we fixed extragalactic environments and only

modified the characteristics of the sources, which were the set of local sources, the luminosity, and the density of background sources. There are several features related to the behavior of the amplitude of the dipole as we changed the parameter space. We emphasize that the amplitude of the dipole increases with energy regardless of the phenomenological model. The primary objective of this work was to determine a density range for background sources. An interesting aspect of the study is realizing that would be possible to get the information about the density through the normalized amplitude of the dipole, since altering the density of background sources can either increase or decrease this measurement. Consequently, we were able to constrain the density of background sources, within a range of one order of magnitude, from 2.20×10^{-4} to $57.44 \times 10^{-4}\,\mathrm{Mpc}^{-3}$ at a 3σ confidence level. This was achieved through a chi-square statistical test comparing our simulation results with the measurements from the Pierre Auger Observatory. Furthermore, our results aligned with previous findings from Pierre Auger Collaboration that established a lower limit for the density of ultra-high energy cosmic ray sources. Although we tried to encompass as much as possible distinct characteristic of the sources, it is important to emphasize that in phenomenological works the results depend on the constructed models.

Some ideas for future research arise directly from this work. For instance, we could compare the range of density of background sources that we obtained from simulations with the values of the density of distinct classes of galaxies in order to discover which one accelerates particles to ultra-high energies. Since the amplitude of the dipole itself does not provide direct information about the classes of galaxies, we could investigate another measurement of ultra-high energy cosmic rays, particularly the direction of the dipole as a function of energy, by using both local and background sources. This approach could help us understand whether these sources can explain what we observe on Earth. In any case, the question of the origin of ultra-high energy cosmic rays remains an open question, and we continue to advance toward unveiling their sources and providing insights into the physics of these fascinating cosmic particles.

REFERENCES

1 AAB, A. *et al.* Cosmic-ray anisotropies in right ascension measured by the Pierre Auger Observatory. **The Astrophysical Journal**, v. 891, n. 2, p. 142, 2020. DOI: 10.3847/1538-4357/ab7236.

2 BATISTA, R. A. *et al.* Open questions in cosmic-ray research at ultrahigh energies. **Frontiers in Astronomy and Space Sciences**, v. 6, p. 23, 2019. DOI: 10.3389/fspas.2019.00023.

3 EVOLI, C. **The Cosmic-ray energy spectrum**. 2020. Available at: https://doi.org/10.5281/zenodo.4396125. Accessible at: 27 Sept. 2023.

4 AUGER, P. *et al.* Extensive cosmic-ray showers. **Reviews of Modern Physics**, APS, v. 11, n. 3-4, p. 288- 291, 1939.

5 GREISEN, K. End to the cosmic-ray spectrum? **Physical Review Letters**, APS, v. 16, n. 17, p. 748-750, 1966. DOI: 10.1103/PhysRevLett.16.748.

6 ZATSEPIN, G. T.; KUZ'MIN, V. A. Upper limit of the spectrum of cosmic rays. **Soviet Journal of Experimental and Theoretical Physics Letters**, v. 4, p. 78-80, 1966.

7 PENZIAS, A. A.; WILSON, R. W. A measurement of excess antenna temperature at 4080 mhz. In: LANG, K. R.; GINGERICH, O. (ed.). **A source book in astronomy and astrophysics, 1900–1975**. Harvard: Harvard University Press, 1979. p. 873–876.

8 AAB, A. *et al.* Observation of a large-scale anisotropy in the arrival directions of cosmic rays above 8×10^{18} eV. **Science**, American Association for the Advancement of Science, v. 357, n. 6357, p. 1266–1270, 2017.

9 AAB, A. *et al.* The Pierre Auger Observatory and its upgrade. **Science Reviews: from the end of the world**, v. 1, n. 4, p. 8–33, 2020.

10 SAGAWA, H.; COLLABORATION, T. A. Highlights from the telescope array experiment. **Brazilian Journal of Physics**, Springer, v. 44, p. 589–599, 2014.

11 AAB, A. *et al.* Features of the energy spectrum of cosmic rays above 2.5×10^{18} eV using the Pierre Auger Observatory. **Physical Review Letters**, v. 125, n. 12, p. 121106, 2020. DOI: 10.1103/PhysRevLett.125.121106.

12 TSUNESADA, Y. *et al.* Joint analysis of the energy spectrum of ultra-high-energy cosmic rays measured at the Pierre Auger Observatory and the Telescope Array. **Proceedings of Science**, v. 395, p. 1–14, 2022. DOI: 10.5445/IR/1000156082.

13 PIEROG, T. *et al.* Epos lhc: Test of collective hadronization with data measured at the cern large hadron collider. **Physical Review C**, APS, v. 92, n. 3, p. 034906, 2015.

14 OSTAPCHENKO, S. Monte carlo treatment of hadronic interactions in enhanced pomeron scheme: Qgsjet-ii model. **Physical Review D**, APS, v. 83, n. 1, p. 014018, 2011.

15 FEDYNITCH, A. *et al.* Hadronic interaction model sibyll 2.3 c and inclusive lepton fluxes. **Physical Review D**, APS, v. 100, n. 10, p. 103018, 2019.

16 HALIM, A. A. *et al.* Depth of maximum of air-shower profiles: testing the compatibility of the measurements at the Pierre Auger Observatory and the Telescope Array. **Proceedings of Science**, p. 249, 2023. DOI: 10.22323/1.444.0249.

17 AAB, A. *et al.* An indication of anisotropy in arrival directions of ultra-high-energy cosmic rays through comparison to the flux pattern of extragalactic gamma-ray sources. **The Astrophysical Journal Letters**, v. 853, n. 2, p. L29, 2018. DOI: 10.3847/2041-8213/aaa66d.

18 ABBASI, R. U. *et al.* Indications of intermediate-scale anisotropy of cosmic rays with energy greater than 57 EeV in the northern sky measured with the surface detector of the Telescope Array experiment. **The Astrophysical Journal Letters**, v. 790, n. 2, p. L21, 2014. DOI: 10.1088/2041-8205/790/2/L21.

19 ALMEIDA, R. *et al.* Large-scale and multipolar anisotropies of cosmic rays detected at the Pierre Auger Observatory with energies above 4 EeV. 2022. **Proceedings of Science**, v. 395, 2021. DOI: 10.22323/1.395.0335.

20 HILLAS, A. M. The origin of ultra-high-energy cosmic rays. **Annual Review of Astronomy and Astrophysics**, v. 22, n. 1, p. 425–444, 1984. DOI:10.1146/annurev.aa.22.090184.002233.

21 CHEN, F. F. **Introduction to plasma physics**. Berlin: Springer Science & Business Media, 2012.

22 PELLETIER, G. Fermi acceleration of astroparticles. *In*: LEMOINE, M.; SIGL, G. (ed.) **Physics and astrophysics of ultra-high-energy cosmic rays**. Berlin: Springer, 2001. p. 58–89.

23 KATAOKA, J.; STAWARZ, Ł. X-ray emission properties of large-scale jets, hot spots, and lobes in active galactic nuclei. **The Astrophysical Journal**, IOP Publishing, v. 622, n. 2, p. 797, 2005.

24 PTITSYNA, K. V.; TROITSKY, S. V. Physical conditions in potential accelerators of ultra-high-energy cosmic rays: updated hillas plot and radiation-loss constraints. **Physics-Uspekhi**, IOP Publishing, v. 53, n. 7, p. 691, 2010.

25 THOMPSON, T. A. *et al.* Magnetic fields in starburst galaxies and the origin of the fir-radio correlation. **The Astrophysical Journal**, IOP Publishing, v. 645, n. 1, p. 186, 2006.

26 TAYLOR, A. M.; AHLERS, M.; AHARONIAN, F. A. Need for a local source of ultrahigh-energy cosmic-ray nuclei. **Physical Review D**, v. 84, n. 10, p. 105007, 2011. DOI: 10.1103/PhysRevD.84.105007.

27 FERMI, E. On the origin of the cosmic radiation. **Physical Review**, v. 75, n. 8, p. 1169-1174, 1949. DOI:10.1103/PhysRev.75.1169.

28 LONGAIR, M. S. **High energy astrophysics**. Cambridge: Cambridge University Press, 2010.

29 AXFORD, W.; LEER, E.; SKADRON, G. *In*: . [*S.l.: s.n.*]. The acceleration of cosmic rays by shock waves. *In*: INTERNATIONAL COSMIC RAY CONFERENCE, 15., 1977, Plovdiv. **Proceedings** [. . .] Plovdiv: ICRC, 1977.

30 KRYMSKY, G. F. Regular mechanism of charged particle acceleration on the shock wave. **Doklady Akademii Nauk SSSR**, v. 234, n. 6, p. 1306–1308, 1977.

31 BELL, A. The acceleration of cosmic rays in shock fronts – I. **Monthly Notices of the Royal Astronomical Society**, v. 182, n. 2, p. 147–156, 1978.

32 BELL, A. The acceleration of cosmic rays in shock fronts – II. **Monthly Notices of the Royal Astronomical Society**, v. 182, n. 3, p. 443–455, 1978.

33 BLANDFORD, R. D.; OSTRIKER, J. P. Particle acceleration by astrophysical shocks. **Astrophysical Journal**, v. 221, p. L29–L32, 1978.

34 LANG, R. G. *et al.* Revisiting the distance to the nearest ultrahigh energy cosmic ray source: effects of extragalactic magnetic fields. **Physical Review D**, v. 102, n. 6, p. 063012, 2020. DOI:10.1103/PhysRevD.102.063012.

35 LANG, R. G.; TAYLOR, A. M.; SOUZA, V. de. Ultrahigh-energy cosmic rays dipole and beyond. **Physical Review D**, v. 103, n. 6, p. 063005, 2021. DOI:10.1103/PhysRevD.103.063005.

36 DING, C.; GLOBUS, N.; FARRAR, G. R. The imprint of large-scale structureon the ultrahigh-energy cosmic-ray sky. **The Astrophysical Journal Letters**, v. 913, n. 1, p. L13, 2021. DOI 10.3847/2041-8213/abf11e.

37 WIBIG, T.; WOLFENDALE, A. W. 27 WIBIG, T.; WOLFENDALE, A. W. **Heavy cosmic ray nuclei from extragalactic sources above 'the ankle'**. 2007. Available at: https://arxiv.org/pdf/0712.3403.pdf. Accessible at: 2 Oct. 2023.

38 PIRAN, T. **A new limit on the distances of nuclei uhecrs sources**. 2010. Available at: https://arxiv.org/pdf/1005.3311.pdf. Accessible at: 2 Oct. 2023.

39 BIERMANN, P. L.; SOUZA, V. D. Centaurus a: the extragalactic source of cosmic rays with energies above the knee. **The Astrophysical Journal**, v. 746, n. 1, p. 72, 2012.

40 MOLLERACH, S.; ROULET, E. Ultrahigh energy cosmic rays from a nearby extragalactic source in the diffusive regime. **Physical Review D**, v. 99, n. 10, p. 103010, 2019.

41 OLIVEIRA, C. de; SOUZA, V. de. Nearby active galactic nuclei and starburst galaxies as sources of the measured UHECRs anisotropy signal. **Journal of Cosmology and Astroparticle Physics** v. 2023, n. 7, p. 58, 2023. DOI 10.1088/1475-7516/2023/07/058.

42 BATISTA, R. A. *et al.* CRPropa 3.2 – an advanced framework for high-energy particle propagation in extragalactic and galactic spaces. **Journal of Cosmology and Astroparticle Physics**, v. 2022, n. 9, p. 35, 2022. DOI: 10.1088/1475-7516/2022/09/035.

43 VELZEN, S. van *et al.* Radio galaxies of the local universe-all-sky catalog, luminosity functions, and clustering. **Astronomy & Astrophysics**, v. 544, p. A18, 2012. DOI 10.1051/0004-6361/201219389.

44 GILMORE, R. C. *et al.* Semi-analytic modelling of the extragalactic background light and consequences for extragalactic gamma-ray spectra. **Monthly Notices of the Royal Astronomical Society**, v. 422, n. 4, p. 3189–3207, 2012. DOI:10.1111/j.1365-2966.2012.20841.x.

45 KNEISKE, T. M. *et al.* Implications of cosmological gamma-ray absorption-II. modification of gamma-ray spectra. **Astronomy & Astrophysics**, v. 413, n. 3, p. 807–815, 2004.

46 STECKER, F. W.; MALKAN, M. A.; SCULLY, S. Intergalactic photon spectra from the far-ir to the uv lyman limit for $0 < z < 6$ and the optical depth of the universe to high-energy gamma rays. **The Astrophysical Journal**, v. 648, n. 2, p. 774-783, 2006. DOI: 10.48550/arXiv.astro-ph/051044.

47 FRANCESCHINI, A.; RODIGHIERO, G.; VACCARI, M. Extragalactic optical-infrared background radiation, its time evolution and the cosmic photon-photon opacity. **Astronomy & Astrophysics**, v. 487, n. 3, p. 837–852, 2008.

48 FINKE, J. D.; RAZZAQUE, S.; DERMER, C. D. Modeling the extragalactic background light from stars and dust. **The Astrophysical Journal**, v. 712, n. 1, p. 238-249, 2010. DOI: 10.1088/0004-637X/712/1/238.

49 DOMINGUEZ, A. *et al.* Extragalactic background light inferred from AEGIS galaxy-SED-type fractions. **Monthly Notices of the Royal Astronomical Society**, v. 410, n. 4, p. 2556–2578, 2011. 2011. DOI:10.1111/j.1365-2966.2010.17631.x.

50 HELGASON, K.; KASHLINSKY, A. Reconstructing the γ-ray photon optical depth of the universe to z 4 from multiwavelength galaxy survey data. **The Astrophysical Journal Letters**, IOP Publishing, v. 758, n. 1, p. L13, 2012.

51 STECKER, F. W.; SCULLY, S. T.; MALKAN, M. A. An empirical determination of the intergalactic background light from uv to fir wavelengths using fir deep galaxy surveys and the gamma-ray opacity of the universe. **The Astrophysical Journal**, IOP Publishing, v. 827, n. 1, p. 6, 2016.

52 SALDANA-LOPEZ, A. *et al.* An observational determination of the evolving extragalactic background light from the multiwavelength hst/candels survey in the fermi and cta era. **Monthly Notices of the Royal Astronomical Society**, Oxford University Press, v. 507, n. 4, p. 5144–5160, 2021.

53 FINKE, J. D. *et al.* Modeling the extragalactic background light and the cosmic star formation history. **The Astrophysical Journal**, IOP Publishing, v. 941, n. 1, p. 33, 2022.

54 CASH, J. R.; KARP, A. H. A variable order runge-kutta method for initial value problems with rapidly varying right-hand sides. **ACM Transactions on Mathematical Software (TOMS)**, ACM, v. 16, n. 3, p. 201–222, 1990.

55 TANCO, G. M. Cosmic magnetic fields from the perspective of ultra-high-energy cosmic rays propagation. In: LEMOINE, M.; SIGL, G. (ed). **Physics and astrophysics of ultra-high-energy cosmic rays**. Berlin: Springer, 2001. p. 155–180.

56 HARARI, D. *et al.* Lensing of ultra-high energy cosmic rays in turbulent magnetic fields. Lensing of ultra-high energy cosmic rays in turbulent magnetic fields. **Journal of High Energy Physics**, v. 2002, n. 3, p. 45, 2002. DOI: 10.1088/1126-6708/2002/03/045.

57 KOLMOGOROV, A. N. The local structure of turbulence in incompressible viscous fluid for very large reynolds. **Doklady Akademiia Nauk SSSR**, v.30, p.301-305, 1941.

58 KOLMOGOROV, A. N. The local structure of turbulence in incompressible viscous fluid for very large reynolds numbers. **Proceedings of the Royal Society of London. Series A: mathematical and physical sciences**, The Royal Society London, v. 434, n. 1890, p. 9–13, 1991.

59 ACKERMANN, M. *et al.* GeV observations of star-forming galaxies with the Fermi Large Area Telescope. **The Astrophysical Journal**, v. 755, n. 2, p. 164, 2012. DOI: 10.1088/0004-637X/755/2/164.

60 SAHAKYAN, N.; BAGHMANYAN, V.; ZARGARYAN, D. Fermi-LAT observation of nonblazar AGNs. **Astronomy & Astrophysics**, v. 614, p. A6, 2018. DOI:10.1051/0004-6361/201732304.

61 AAB, A. *et al.* Combined fit of spectrum and composition data as measured by the Pierre Auger Observatory. **Journal of Cosmology and Astroparticle Physics**, v. 2017, n. 4, p. 38, 2017. DOI 10.1088/1475-7516/2017/04/038.

62 AUBLIN, J.; PARIZOT, E. Generalised 3D-reconstruction method of a dipole anisotropy in cosmic-ray distributions. **Astronomy & Astrophysics**, v. 441, n. 1, p. 407–415, 2005. DOI: 10.1051/0004-6361:20052833.

63 JÜTTNER, F. Das maxwellsche gesetz der geschwindigkeitsverteilung in der relativtheorie. **Annalen der Physik**, Wiley Online Library, v. 339, n. 5, p. 856–882, 1911.

64 ALOISIO, R.; BEREZINSKY, V.; GAZIZOV, A. The problem of superluminal diffusion of relativistic particles and its phenomenological solution. **The Astrophysical Journal**, IOP Publishing, v. 693, n. 2, p. 1275, 2009.

65 ABREU, P. *et al.* Bounds on the density of sources of ultra-high energy cosmic rays from the Pierre Auger Observatory. **Journal of Cosmology and Astroparticle Physics**, v. 2013, n. 5, p. 9, 2013. DOI:10.1088/1475-7516/2013/05/009.

66 HUCHRA, J. P. *et al.* The 2mass redshift survey—description and data release. **The Astrophysical Journal Supplement Series**, IOP Publishing, v. 199, n. 2, p. 26, 2012.

APPENDIX

APPENDIX A – RESULTS OF THE AMPLITUDE OF THE DIPOLE

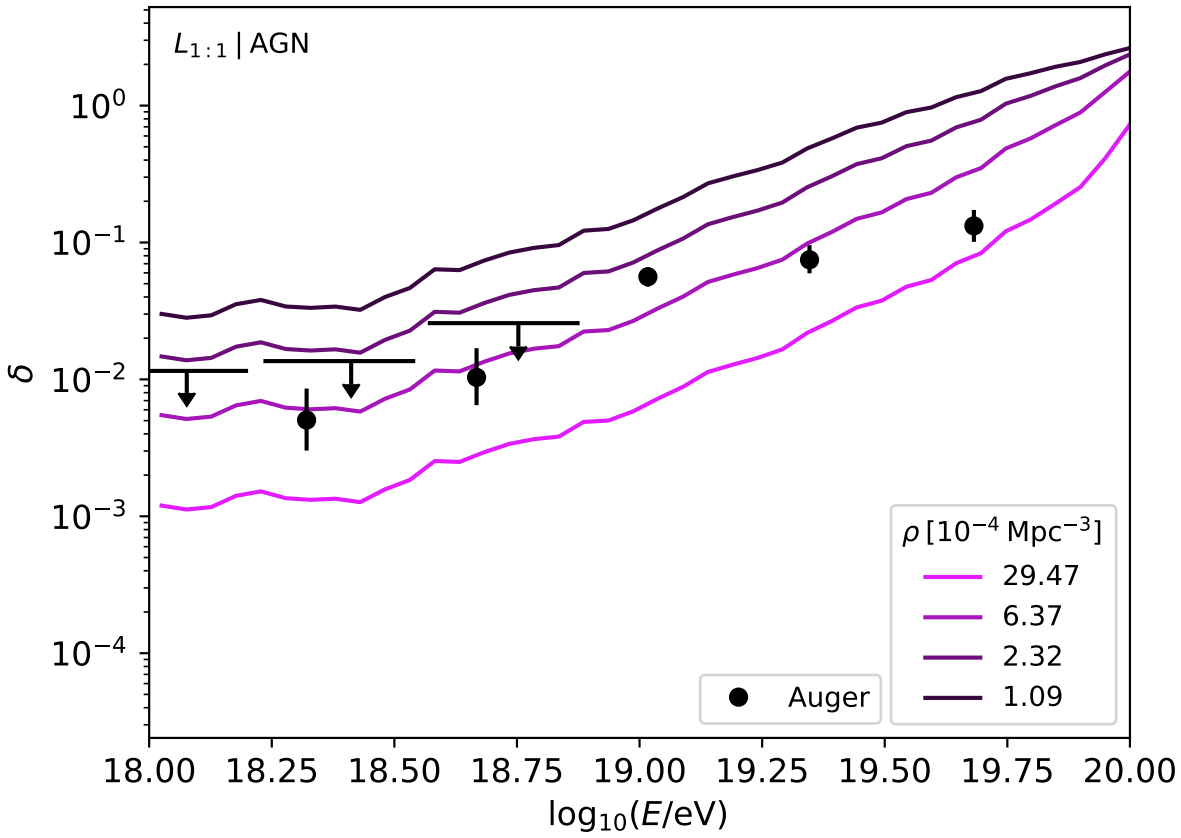

Figure 32 – Amplitude of the dipole as a function of energy for the second term of the Equation (4.26) equal to zero. The case is illustrated for an equal particle emission regardless of the astrophysical source, with active galactic nuclei as local sources. The colored curved represent four values of the density of background sources, and the black points with uncertainties correspond to measurements from the Pierre Auger Observatory. (1)

Source: By the author.

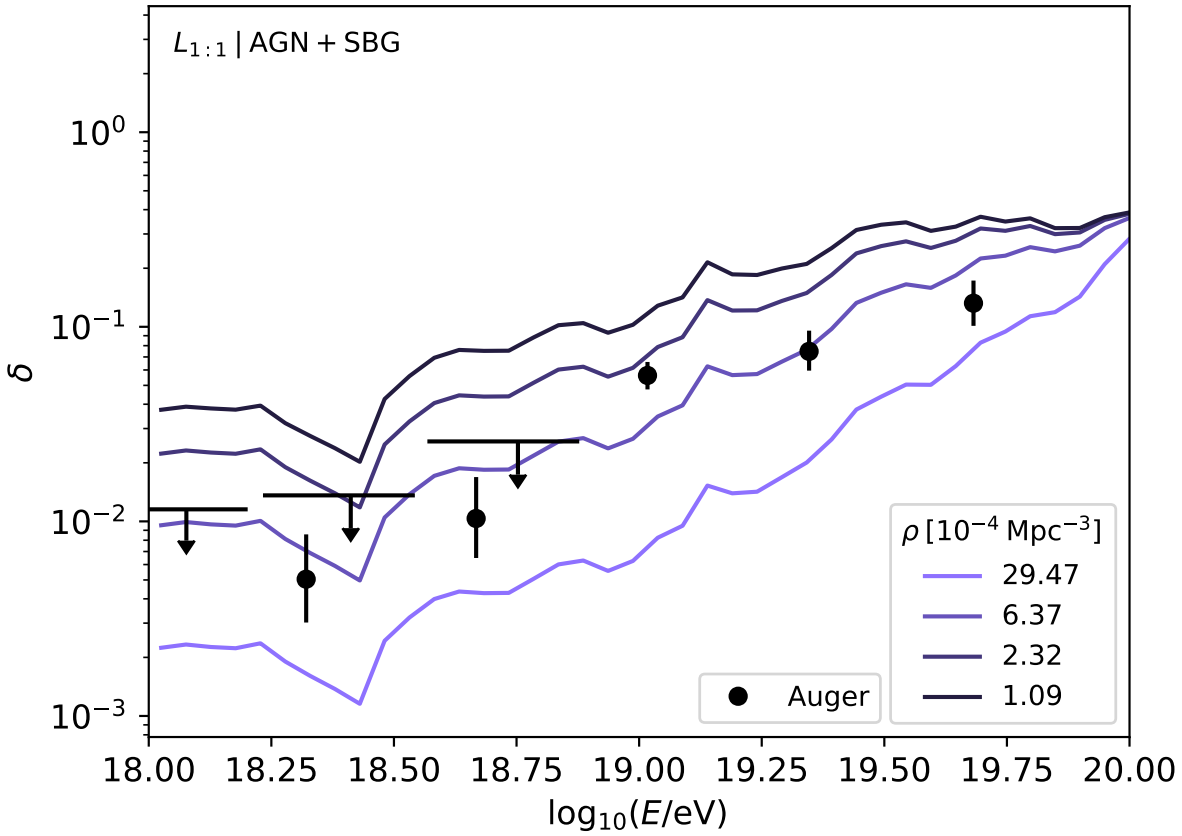

Figure 33 – Amplitude of the dipole as a function of energy for the second term of the Equation (4.26) equal to zero. The case is illustrated for an equal particle emission regardless of the astrophysical source, with active galactic nuclei and starburst galaxies as local sources. The colored curved represent four values of the density of background sources, and the black points with uncertainties correspond to measurements from the Pierre Auger Observatory. (1)

Source: By the author.

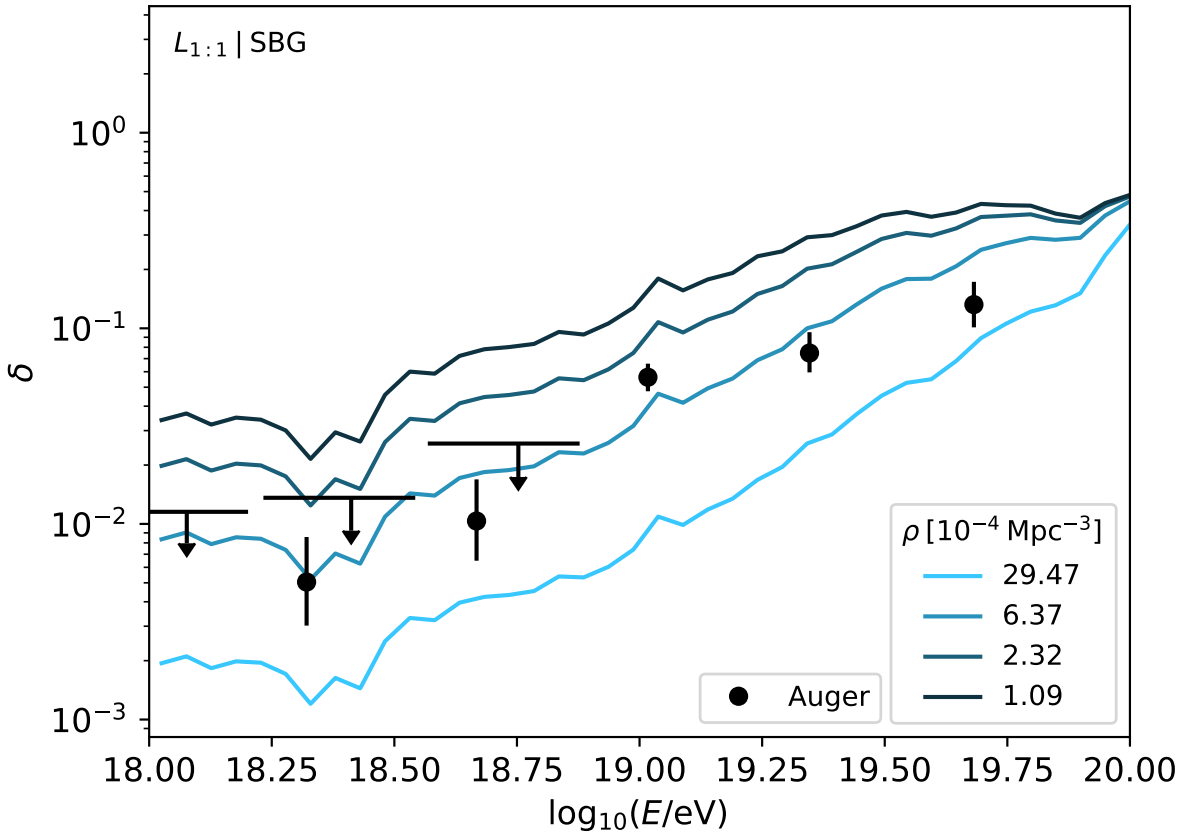

Figure 34 – Amplitude of the dipole as a function of energy for the second term of the Equation (4.26) equal to zero. The case is illustrated for an equal particle emission regardless of the astrophysical source, with starburst galaxies as local sources. The colored curved represent four values of the density of background sources, and the black points with uncertainties correspond to measurements from the Pierre Auger Observatory. (1)

Source: By the author.

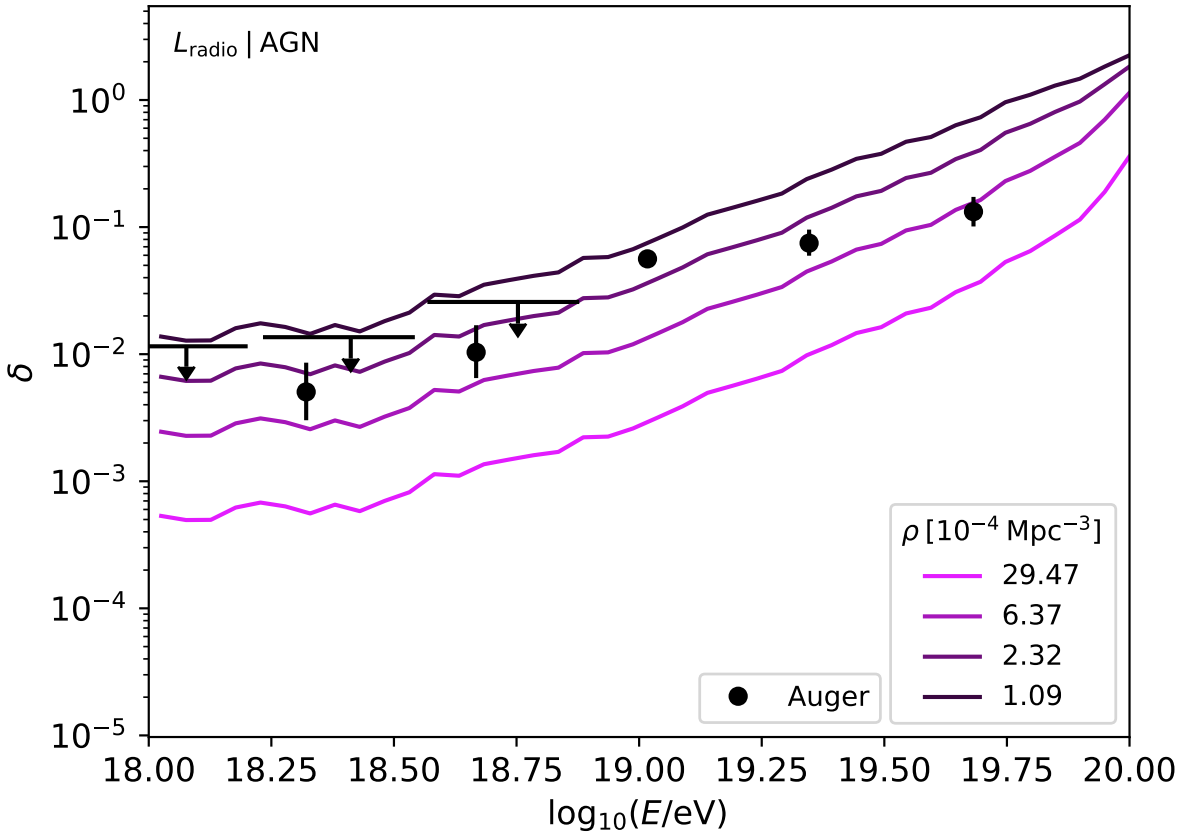

Figure 35 – Amplitude of the dipole as a function of energy for the second term of the Equation (4.26) equal to zero. The case is illustrated for a particle emission proportional to the radio luminosity, with active galactic nuclei as local sources. The colored curved represent four values of the density of background sources, and the black points with uncertainties correspond to measurements from the Pierre Auger Observatory. (1)

Source: By the author.

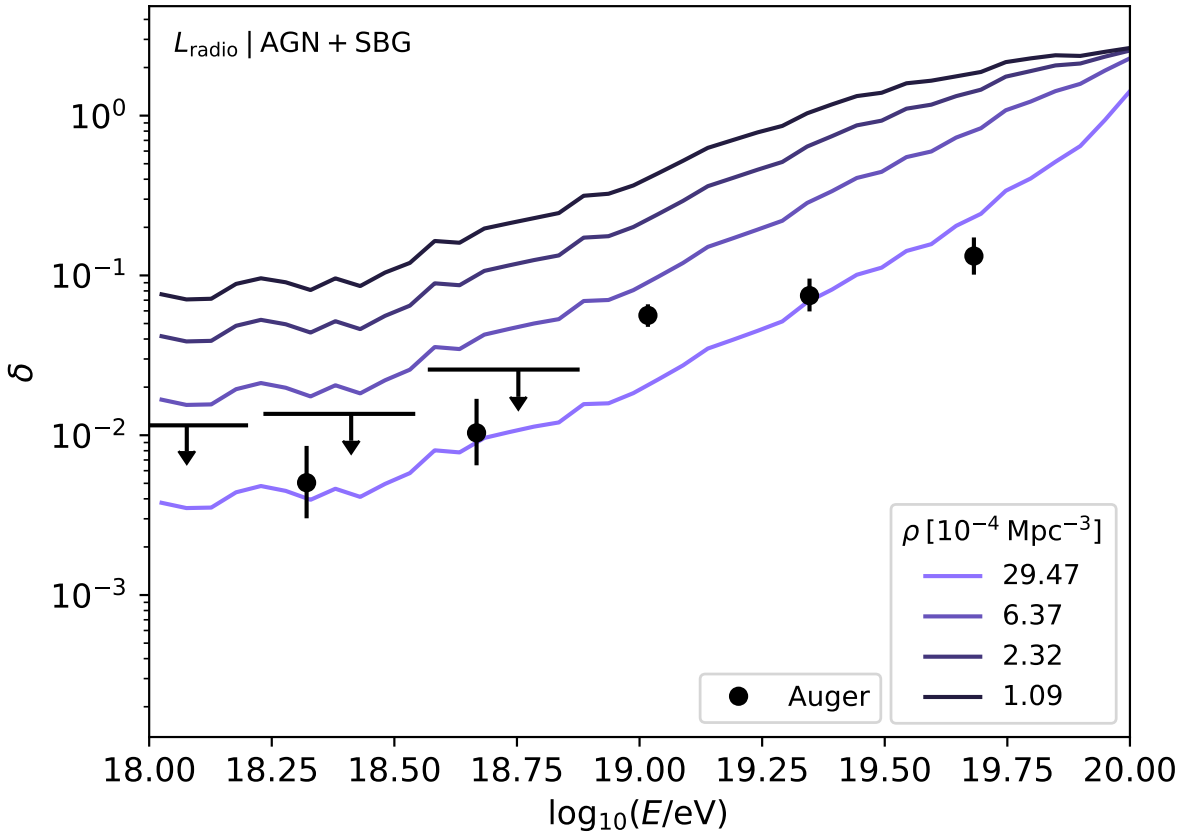

Figure 36 – Amplitude of the dipole as a function of energy for the second term of the Equation (4.26) equal to zero. The case is illustrated for a particle emission proportional to the radio luminosity, with active galactic nuclei and starburst galaxies as local sources. The colored curved represent distinct values of the density of background sources, and the black points with uncertainties correspond to measurements from the Pierre Auger Observatory. (1)

Source: By the author.

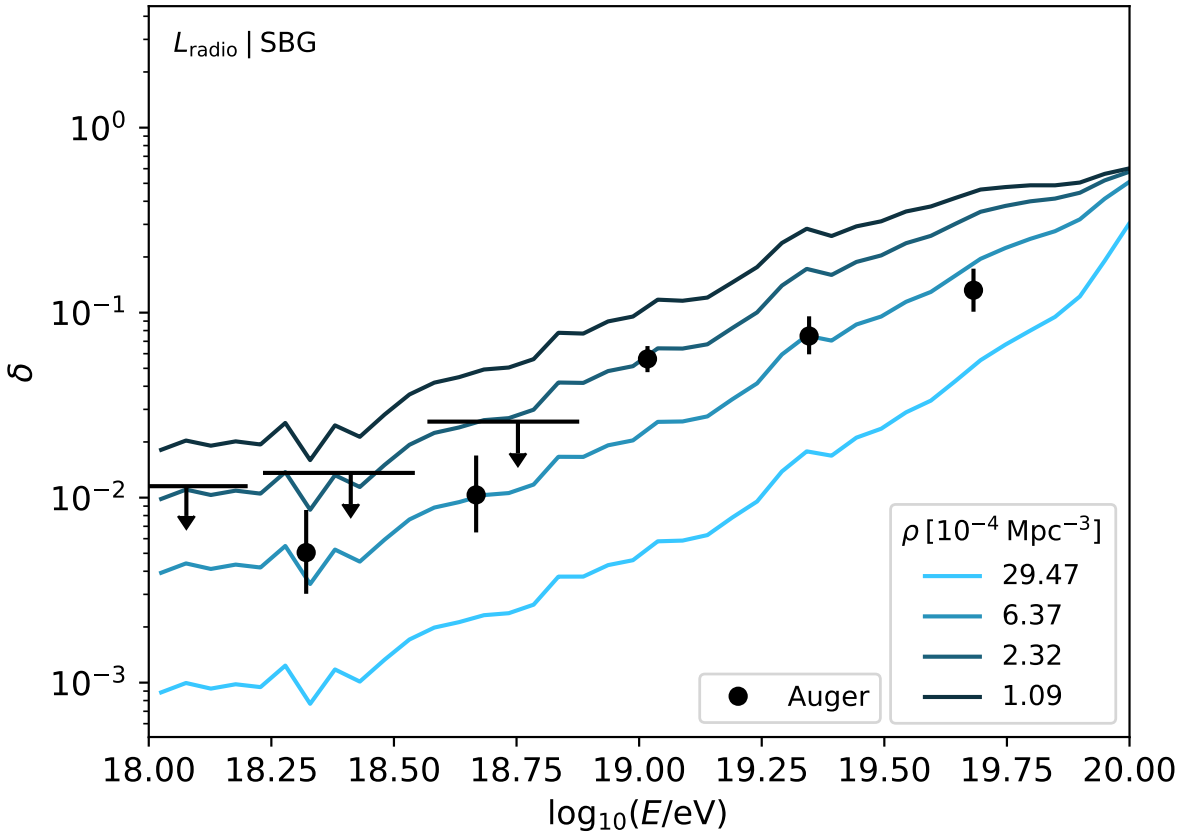

Figure 37 – Amplitude of the dipole as a function of energy for the second term of the Equation (4.26) equal to zero. The case is illustrated for a particle emission proportional to the radio luminosity, with starburst galaxies as local sources. The colored curved represent four values of the density of background sources, and the black points with uncertainties correspond to measurements from the Pierre Auger Observatory. (1)

Source: By the author.

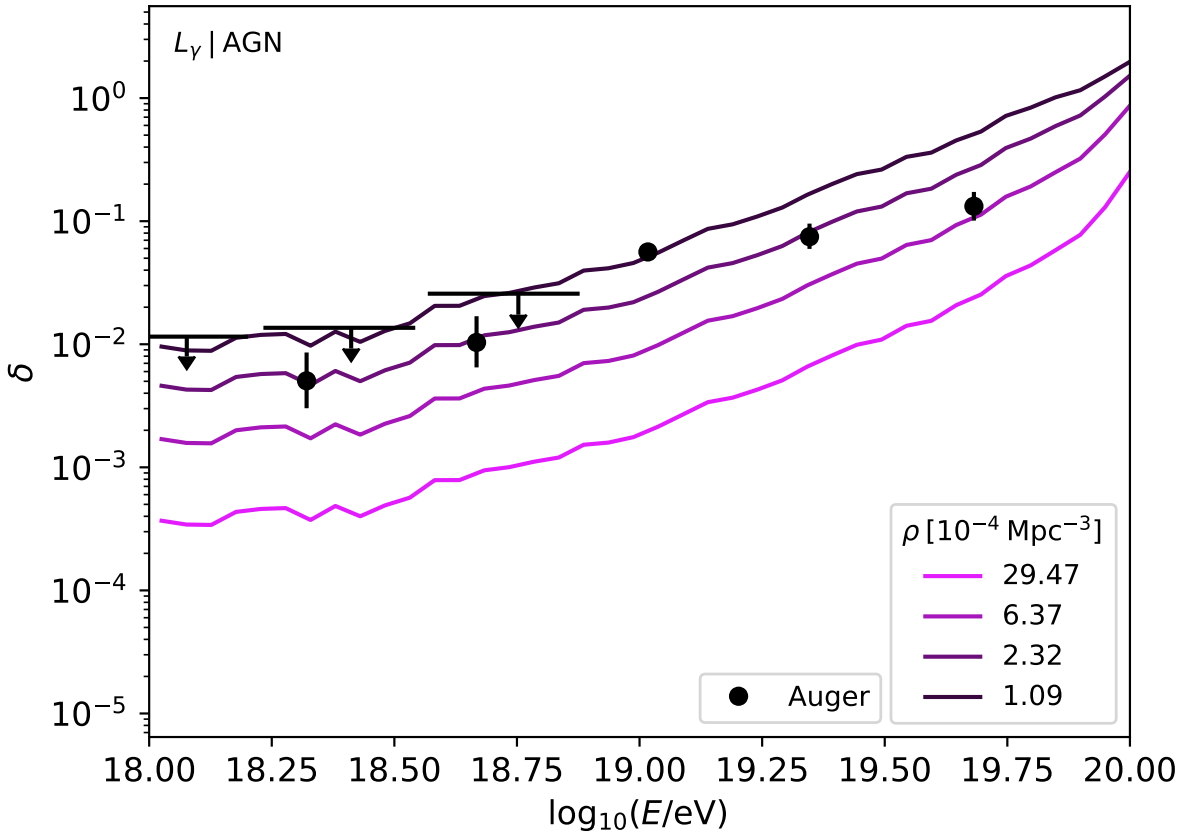

Figure 38 – Amplitude of the dipole as a function of energy for the second term of the Equation (4.26) equal to zero. The case is illustrated for a particle emission proportional to the gamma ray luminosity, with active galactic nuclei as local sources. The colored curved represent four values of the density of background sources, and the black points with uncertainties correspond to measurements from the Pierre Auger Observatory. (1)

Source: By the author.

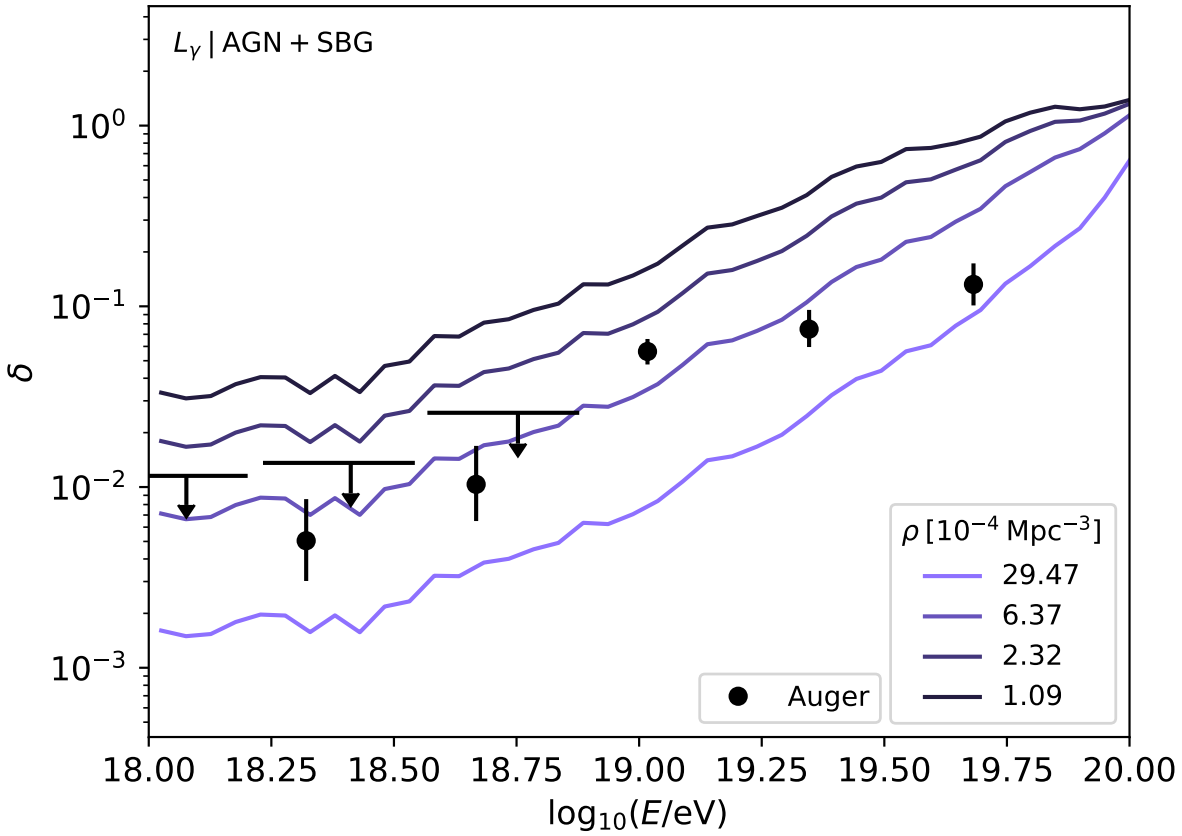

Figure 39 – Amplitude of the dipole as a function of energy for the second term of the Equation (4.26) equal to zero. The case is illustrated for a particle emission proportional to the gamma ray luminosity, with active galactic nuclei and starburst galaxies as local sources. The colored curved represent four values of the density of background sources, and the black points with uncertainties correspond to measurements from the Pierre Auger Observatory. (1)

Source: By the author.

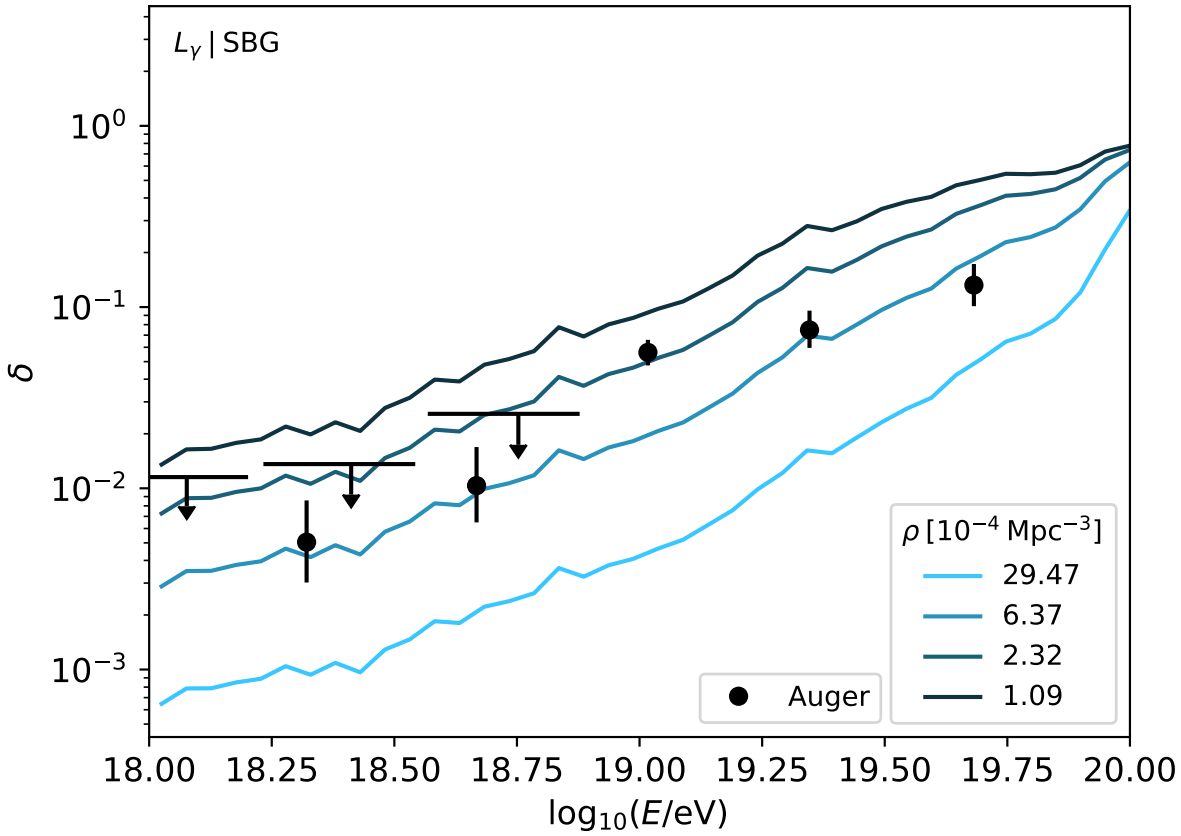

Figure 40 – Amplitude of the dipole as a function of energy for the second term of the Equation (4.26) equal to zero. The case is illustrated for a particle emission proportional to the gamma ray luminosity, with starburst galaxies as local sources. The colored curved represent four values of the density of background sources, and the black points with uncertainties correspond to measurements from the Pierre Auger Observatory. (1)

Source: By the author.